Nonlinear Spatial Dynamics of Double Phase Conjugation in Photorefractive Crystals and Holographic Dynamics of Photopolymerization

Thesis by

Doruk Engin

In Partial Fulfillment of the Requirements

for the Degree of

Doctor of Philosophy

California Institute of Technology

Pasadena, California

1998

(Submitted June 20, 1997)

To my family and friends

Acknowledgments

First, I would like to thank my thesis advisor Prof Amnon Yariv, for giving me the opportunity to work in his group. His support and guidance has made this thesis possible. In the group I had the pleasure to work with Prof. Mordechai Segev who has walked me through the first few manuscripts I was involved in and has introduced me to some of the most exciting problems in photorefractive nonlinear optics. I would like to give special thanks to Prof. M. C. Cross for guiding me through the exciting field of pattern formation outside of equilibrium. Working with his broad knowledge of physics was very inspirational and informative.

I would like to acknowledge the generous financial support from Hughes Graduate Fellowship. The support has made this thesis possible. I would like to especially thank Dr George Valley for support and guidance during the fellowship program.

Special thanks are also extended to the researchers I had the pleasure to collaborate with, including Drs George Valley, Sergei Orlov, Victor Leyva, Prof Bruno Crosignani, Prof. Aharon Agranat, Xiao-lin Tong, Anthony Kewitsch. Helpful discussions with Drs Marvin Klein, David Pepper, Kirill Sheglov, George Rakuljic, Rudolf Hoffmeister are also gratefully acknowledged.

I wish to thank all the remarkable individuals with whom I had the pleasure to interact and work with, including Dr Gilad Almogy, Kevin Cooper, Dr Danny Eliyahu, Dr Jing Feng, Ali Ghaffari, John Ianelli, Dr John Kitching, Roger Koumans, Reginald Lee, Dr William Marshall, Dr Matthew McAdams, Jana Mercado, Dr John O'Brien, Dr Volnei Pedroni, Dan Provenzano, Dr Joseph Rosen, Tal Segev, Dr Randy Salvatori, Dr Lee Borrows, Dr George Barbastathis, Ahmet Kirac, Dr Zehra Cataltepe, Murat Mese, Roman Gutierrez, Akira Saito, Dr Boaz Salik, Dr Ali Shakouri, Dr Yuanjian Xu, Min Zhang, Wanda Renderos.

First and foremost I would like to thank my brother Kerim Can Engin, sister in law Monique Ehsan, my parents Sevgi and Morton Actor, for their support, care and encouragements. I would lastly like to thank Elif Sibel Yelten for being so amazingly beatiful.

Abstract

This thesis explores spatial nonlinear optical effects in photorefractive crystals and photopolymers. In these materials upon exposure with spatially varying light, large refractive index changes occur. In the first part of the thesis Double Phase Conjugation in photorefractive crystals is studied both theoretically and experimentally. Various processes effecting the conjugation fidelity, such as fanning are quantified through a coupled multiple mode model which is an extension of the coupled mode theory. Predictions of the model such as assymetric phase conjugation is confirmed experimentally. Critical slowing down near the threshold is also predicted and experimentally confirmed. Lastly the amplitude equation formalism is carried out for the wave mixing phenomenon. This approach unifies the optical phenomenon with a large class of other physical phenomena referred to as pattern formation outside of equilibrium. Through this formalism the instability is identified as a convective instability and the possibility of a transition to absolute instability is studied.

In the second part of the thesis, photopolymerization dynamics is studied with holography. A theoretical model is developed for the holographic configuration starting from a standard chain polymerization model. A holographic characterization method is developed. The method is especially powerful in measuring diffusion constants. Various multifunctional polymers is characterized using the novel technique.

Table of Contents

Chapter one

Introduction and Thesis Outline

1.1 Wave mixing in photorefractive crystals

A photorefractive crystal (p.r.) may be regarded as a nonlinear device allowing parametric amplification of coherent signal waves containing spatial information [1]. Amplification of one coherent beam in the expanse of an other (two wave mixing[2-4]) is a result of non-local response of the photorefractive crystals. Refractive index change within the electro optic crystal is facilitated by charge transport between the bright and the dark regions [5]. Resulting index changes are typically out of phase with the intensity pattern which makes coherent amplification possible. The gain provided by p.r. nonlinearities can be as large as 10-100 cm^{-1} [6] Phase conjugate wave front generation is also obtainable in photorefractive crystals by degenerate or nearly degenerate four wave mixing [7 , 8 ch. 6]. Phase conjugation permits the restoration of phase distorted wave fronts which is difficult by other means. Phase conjugation can be used in imaging systems, for coupling sources with small and very different numerical apertures (single to multi-mode fiber coupling [9], laser diode coupling [10]), for correcting for phase distortions due to propagation through multimode fibers or scattering media.

Coupled mode theories (CMT) have been very successful in quantifying some basic characteristics of the nonlinear wave mixing interactions [4] such as the energy transfer between the beams as a function of the coupling constant in two wave mixing. In CMT models the interacting beams are treated as plane waves which couple through one or two self written dynamic gratings (sections 3.2, 4.2). These plane waves interact in a 2-D area infinite in one of the dimensions and finite in the other. This approach albeit unrealistic in many respects, (i.e. finite interaction region, pump beams with spatial information) is a convenient starting point from a theoretical point of view and the resulting nonlinear equations can often be solved analytically. On the other hand CMT can not address a number of practical issues, such as the quality of phase conjugation, the quality of the amplified image in two wave mixing.

In experiments a number of different mechanisms is found which reduce the performance. In double phase conjugate mirror (DPCM) [11] (section 4.1) which is studied extensively here experimentally (chapter 5) and theoretically (chapters 4,6), at least three separate mechanisms can be identified. Conical ring formation coexists with phase conjugation when the pump beams have simple spatial information [12]. Fanning (section 3.4) also coexist with phase conjugation especially when the input pump intensities are asymmetric [13] (section 5.4, section 4.8). A third and controversial mechanism is the large scale distortions in phase conjugate outputs that result from the convective nature of the instability. This mechanism was first suggested theoretically [14] and then observed experimentally (this is controversial) [15]. It may account for the better quality of phase conjugation observed in the lower right corner of images in figure 5.5. For other schemes, for example, image amplification via two wave mixing; the competition between fanning and two wave mixing is an important mechanism that result in both distortions of the amplified image and lower effective gain.

Various approaches have been employed for modeling the wave mixing interaction more realistically. In a number of studies the starting equations (Helmholtz equations and photorefractive material equations) that are in the form of nonlinear partial differential equations are solved numerically [16, 17, 18]. Figure[1.1] shows numerical results reported in reference[16].

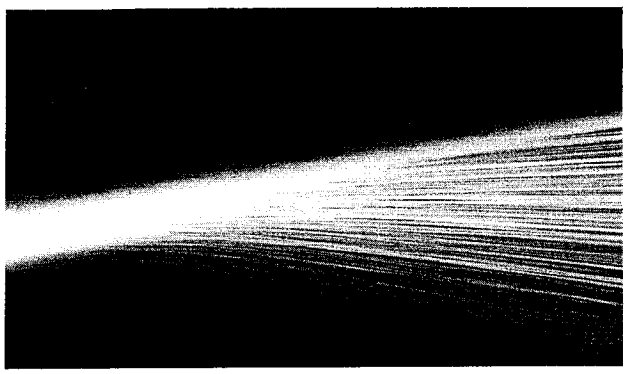

Figure 1.1 the fanning simulations from ref[16]. Large angular output behavior that is generally associated with fanning, as well as tiny filamentation of the original beam are apparent.

These simulations duplicate the observed behavior in experiments very well. However by themselves, (just like in experiments) it is very difficult to isolate the different mechanisms and to study the dependencies of the mechanisms on the system parameters. Here we describe two approaches that can be seen as generalizations of the coupled mode theories. They are computationally less demanding and they enable easier identification of specific physical processes.

The first approach involves formulating the starting equations in the Fourier space [18, 19]. Only two major approximations are carried out, scattering of waves from phase mismatched gratings is neglected in the first one. This approximation is a reasonable assumption when the volume holograms are thick. In the other approximation the

linearization of the materials equations is carried out by assuming a large uniform intensity as compared to the amplitudes of the intensity variations (section 2.3). In the experiments described in chapter 5, care is taken to generate the latter condition. When the entire Fourier spectrum is sampled by only few plane waves the formulation resembles CMT with multiple mode. For this reason we refer to this formulation as coupled multiple mode theory (CMMT).

(a)

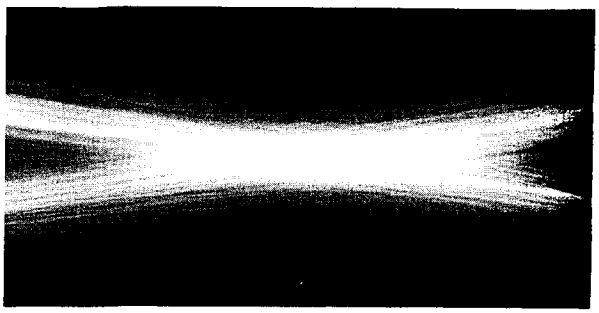

(b)

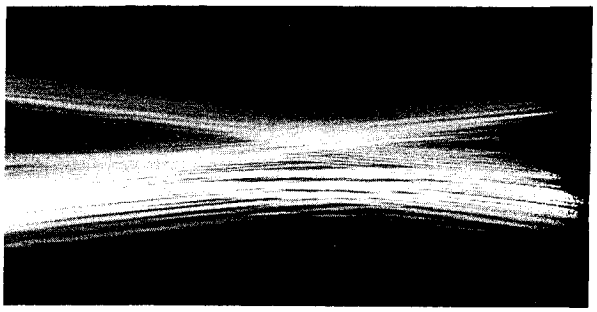

(c)

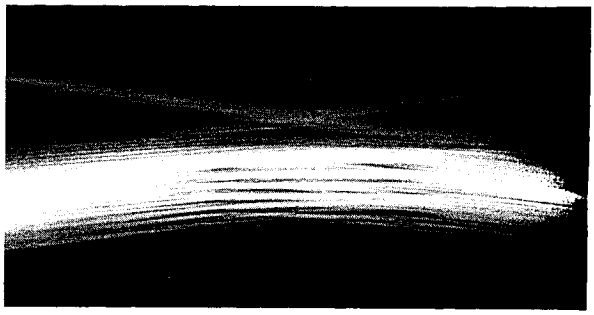

Figure 1.2 DPCM dynamics from ref[16]. a, b and c are steady state results for respectively increasing the p.r. nonlinearity.

Using CMMT we simulate fanning (chapter 3) and the double phase conjugate mirror (chapter 4) and study two dimensional effects such as the angular distribution of fanned output and the quality of phase conjugation.

Our first approach is ideal for modeling distortion mechanisms such as competition between fanning and the phase conjugation. However modeling mechanisms that result in large scale distortions, such as convective behavior, require a dense sampling of the spatial frequency spectrum. In addition the assumption of ignoring the phase-mismatched scattering processes in this case is questionable, since as it will be discussed in chapter 6, the convective behavior arises from the phase-mismatched interactions. An alternative approach, the amplitude equation formalism [20] can be employed for studying large scale distortions on the beams in double phase conjugation. This is an approach employed in many different physical systems that exhibit pattern formation when they are under constant non equilibrium conditions [20]. The amplitude equation, just like in the coupled mode theory, is derived for an ideal system where one of the two spatial dimensions is infinite. Near the instability threshold for DPCM, a small family of spatial modes around the phase conjugate mode become unstable. The amplitude equation captures the spatio-temporal behavior of this small family of unstable modes. In addition to the computational advantages of this simpler equation, this approach also allows for the straight forward inclusion of finite transverse boundaries and/or Gaussian shape of the pump beams, (section 6.3).

In this study, coupled multiple mode theory and the amplitude equation formalism are used for modeling the double phase conjugate mirror. In our opinion creative combination of the two techniques may enable the modeling of a number of important practical cases for DPCM, such as pump beams carrying complicated spatial information, conical ring formation, pump beams with different optical frequencies. These techniques

can be applied to other nonlinear wave mixing phenomena as well, such as four wave mixing with local nonlinearity.

1.2 Photopolymerization dynamics and Holography

Photopolymerization dynamics has been studied for the last few decades and many of the fundamental mechanisms are well understood [22]. However the study of diffusion effects in photopolymerization is relatively new, and has especially gained importance in photo-lithography and printing applications [23]. Photopolymers are also one of the most promising materials for holography applications, such as optical data storage [27]. Recently, self focusing and self trapping of optical beams have also been reported in these materials [24]. The process may have applications in large aspect ratio micro-machining, and in sub-micron lithography. Detailed understanding of photopolymerization dynamics is of prime importance in tailoring the materials for these applications.

In this study holography is used as a characterization tool for the photopolymerization dynamics. This characterization technique not only can measure typical kinetic constants such as chain propagation rate and chain termination rates, but it also has the potential to measure diffusion effects, such as monomer diffusion. There are other techniques through which these kinetic constants can be measured [25, 23], although an all optical characterization technique may be advantageous for holography and self trapping applications.

In chapter 7 a standard model for photopolymerization is introduced. This phenomenological model describes the kinetics of the most dominant reactions; it is used as the basis for developing a characterization scheme. Such a scheme is necessary because

photopolymerization involves number of time constants, describing the dynamics of photoinitiators, monomers, radicals and oxygen. We show that by carefully choosing various experimental conditions, it is possible to isolate the different time constants. In chapter 8 the characterization technique is described in detail.

We demonstrate the characterization technique using multifunctional acrylate monomers. These chemicals are among the most widely used uv curable systems today because of their high reactivity, moderated cost, and low volatility. The photopolymerization of multifunctional monomers has been studied extensively, [28, 25, 27]. The main application of these chemicals is in the coating industry, but they are also finding applications in microelectronics and photoimaging. The self-trapping of optical beams have been first observed in these chemicals as well.

In a number of the multifunctional monomers, we find that the monomer diffusion is very weak, although a permanent, fixed grating can be written in these chemicals. This observation is contrary to the accepted notion that the monomer diffusion is essential for fixing gratings in photopolymers [27]. A likely explanation for the observation is that the polymerization is incomplete, due to drastic density changes (cross linking) that accompany polymerization. Our results suggest that the only sure way to find the exact nature of the grating fixing is through careful characterization of the photopolymerization dynamics. The fixing mechanism is expected to be important from the point of view of grating stability and life time.

References for chapter one

[1] P. Gunter and J.-P. Huignard, Chapter 2, *in Photorefractive Materials and Thier Applications*, Vol. 2 edited by P. Gunter and J.P. Huignard (Springer-Verlag, Berlin, 1989).

[2] D. L. Staebler, J.J. Amodei: J. Appl. Phys. **43**, 1043 (1972).

[3] N. Kukhtarev, V. Markov, S. Oloulov, M. Soskin, V. Vinetski: Ferroelectrics, **22**, 946 and 961 (1979).

[4] M. Cronin-Golomb, B. Fisher, A. Yariv: IEEE J. QE-20, **12** (1984).

[5] N. V. Kukhtarev, Pis'ma Zh. Tekh. Fiz. **2**, 1114 (1976).

[6] R. Hellwarth. J. Feinberg: Opt. Lett. **5**, 519 (1980) and **6**, 257 (1981).

[7] B. Ya. Zel'dovich, N. F. Pilipetsky, V. V. Shkunov, *Principles of Phase Conjugation*, (Springer-Verlag, Berlin, 1985).

[8] P. Yeh, *Introduction to Photorefractive Nonlinear Optics* (Wiley-Interscience Publications, 1993).

[9] A. Chiou, P. Yeh, C. Yang, and C. Gu, Opt. Lett. **20**, 1125 (1995).

[10] S. Sternklar, S. Weiss, M. Segev, and B. Fischer, Opt. Lett. 11, 528 (1986).

[11] S. Weiss, S. Sternklar, B. Fischer, Opt. Lett. **12**, 114 (1987).

[12] A. P. Mazur, A. D. Novikov, S. G. Olulov, M.S. Soskin M. V. Vasnetov, J. Opt. Soc. Am. B, **10**, 1408 (1993).

[13] S. S. Orlov, M. Segev, A. Yariv, And G. C. Valley, Opt. Lett. **19**, 578 (1994).

[14] A. A. Zozulya, Opt. Lett. **16**, 545 (1991).

[15] N. V. Bogodaev, V. V. Eliseev, L. I. Ivleva, A. S. Korshunov, S. S. Orlov, N. M. Polozkov, A. A. Zozulya, J. Opt. Soc. Am. B **9**, 1493 (1992).

[16] A. A. Zozulya, M. Saffman, D. Z. Anderson, Phys. Rev. Lett. **73**, 6, 818 (1994).

[17] M. R. Belic, J. Leonardy, D. Timotijevic, F. Kaiser, J. Opt. Soc. Am. B. **12**, 9 (1995).

[18] M. Segev, D. Engin, A. Yariv, G. C. Valley, Opt. Lett. **18**, 1828 (1993).

[19] G. C. Valley, J. Opt. Soc. Am. B **9**, 1440 (1992).

[20] M. C. Cross, P. C. Hohenber, Rev. Mod. Phys. **65**, 851 (1993).

[21] D. Engin, M. C. Cross, A. Yariv, M. Segev, Submitted to J. Opt. Soc. Am. B.

[22] Odion, Georg G., in *Principles of Polymerization* (Wiley-Interscience Publications, 1981)

[23] V. V. Krongauz, Section 2.5, in *Processes in Photoreactive Polymers*, edited by V. V. Krongauz, A. D. Trifunac (Capman and Hall, 1995).

[24] A. S. Kewitsch, A. Yariv, Opt. Lett., **1**, 1, 24 (1996).

[25] C. Decker, K. Moussa, Maromolecules **22**, 4455 (1989).

[26] G. R. Tryson, A. r. Shultz, J. Polym. Sci., 17, 2059 (1979).

[27] R. A. Lessard, R. Changkakoti, G. Manivannan, Section 3.1, in *Processes in Photoreactive Polymers*, edited by V. V. Krongauz, A. D. Trifunac (Capman and Hall, 1995).

[28] C. Decker, Section 3.1, in *Processes in Photoreactive Polymers*, edited by V. V. Krongauz, A. D. Trifunac (Capman and Hall, 1995).

Chapter two

Photorefractive Effect

2.1 Introduction

The photorefractive (p.r) effect has been observed in a variety of electro-optic materials [1] and may be considered a general property of these materials. The effect results in high optical nonlinearities at milliwatt power levels. Depending on the band gap of the material and the energies of the donor and acceptor levels of the impurity ions involved, the photorefractive effect may be induced by ultraviolet, visible or infrared radiation and resulting index changes can be erased by uniform, incoherent illumination.

Light-induced changes of refractive indices are caused by the separation of charges upon illuminating by a spatially varying intensity pattern. Electrons or holes excited from the impurity centers (donors) by light drift, diffuse and retrap until they travel out of the bright regions. Charge transport results in charge separation between the ionized donors and the excited charge carriers. Spatially varying electric field (space charge field) distribution induces a refractive index change via the electro-optic effect. In this chapter we first present a summary of a standard model [3, 1(ch. 3)] that captures the relevant characteristics of the p.r. effect. In section(2.3) we describe a linearized version of the model which assumes an intensity pattern with a small spatially varying component

compared to a large uniform component. In section(2.4), another approximate version of the model is described where the carrier number density is assumed to be in quasi-steady state. Both of these versions lead to a single dynamic equation for the space charge field (as opposed to the four starting equations) for the response of the material which makes it easier to model more complicated wave mixing phenomena.

2.2 Band transport theory

The most basic [3, 1(ch. 3)] model for the p.r. effect in electro optic crystals takes into account only a single family of donor centers with a number density N that have energy levels somewhere in the middle of the band gap.

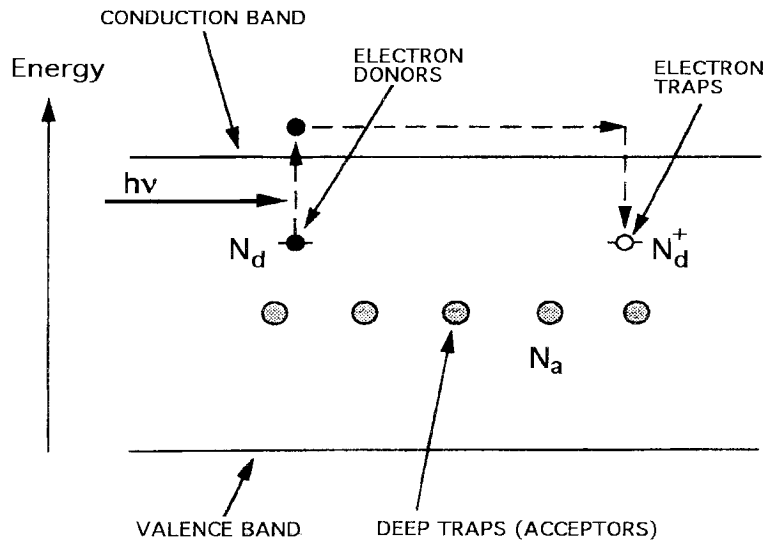

Figure 2.1. Photorefractive band transport model with one photorefractive donor species N_d. Charge compensation condition implies $N_d^+ \cong N_a$ (in the dark). The total donor number density is constant: $N_D = N + N^+$.

In the dark a number of these donor states are assumed to be ionized (become acceptors, with number density N^+) due to another family of lower energy level photo-insensitive

acceptors (with number density, N_A). For example for $BaTiO_3$ [1(ch. 7), 4] (with Fe impurities) donor and ionized donor centers are Fe^{2+} , Fe^{3+} respectively. The charge difference between the two ionized and non-ionized donor states are modeled by treating the donor states as neutral and ionized states as positively charged. Optically inactive acceptor (deep traps) states, which are represented in the model by a single family of states, are taken to be negatively charged and they allow for the overall charge compensation within the crystal. Fig(2.1) shows the band structure assumed within the model.

In the presence of illumination the incident photons ionize the donors generating electrons in the conduction band with a number density n. Positively charged ionized donors act as acceptors capturing back the electrons. The rate equation for the ionized donor density describes the two processes:

$$\frac{\partial N^+}{\partial t} = (s\ I + \beta)(N - N^+) - \gamma\ n\ N^+ \qquad 2.1$$

where β , s , γ are respectively the dark generation rate, cross section of photo-ionization and recombination coefficient. Electrons unlike the donors, can diffuse and drift. The resulting flux of current effects the local charge densities. The process is described by the continuity equation:

$$\frac{\nabla . \mathbf{j}}{e} = \frac{\partial n}{\partial t} - \frac{\partial N^+}{\partial t}, \qquad 2.2$$

The current density j has both drift and diffusion components (neglecting photovoltaic effect [1(ch.2), 5]):

$$\mathbf{j} = e\,\mu\, n\,\mathbf{E} + \mu\, k_B\, T\ \nabla n, \qquad 2.3$$

where μ is the electron/hole mobility. As shown in figure(2.2), in the presence spatially non-uniform intensity pattern, more electrons are generated in the bright regions. Electrons diffuse away from these high electron density regions generating spatial charge distribution.

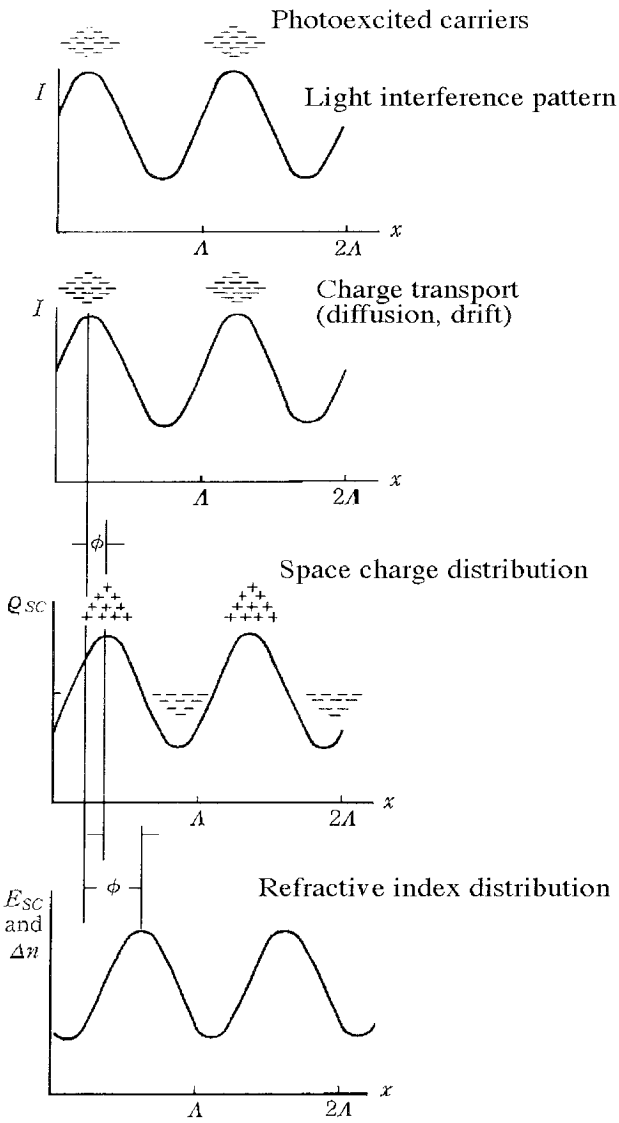

Figure 2.2 illustration of the photorefractive effect for a sinusoidal intensity pattern.

Since the charge transport dynamics are very slow the space charge field generated by the non-uniform charge distribution can be described by the Poisson's equation:

$$\nabla.\mathbf{E} = -(\frac{e}{\varepsilon\ \varepsilon_0})(n + N_A - N^+). \qquad 2.4$$

The internal space charge field given by equation 2.4 creates a spatially inhomogeneous index of refraction via the electro-optic effect. In anisotropic media the dielectric permeability is a three-dimensional tensor and effectively the electro-optic effect results in a perturbation (linear with the space charge field) of the dielectric permeability tensor. The electro-optic effect is defined traditionally, in terms of the local (spatially) change in impermeability tensor and strongly depends on the direction of the space charge field; the crystal symmetry. The general formula for the change in the impermeability tensor is:

$$\Delta\ \eta_{ij} = \Delta\left\{\frac{1}{n^2}\right\}_{ij} = r_{ijk}E_k\ . \quad , \qquad 2.5$$

where r_{ijk} is the linear electro-optic tensor [6(ch. 2)].

2.3 Band transport theory with low intensity modulation (linearized theory)

The above material equations can be linearized if the driving intensity pattern has a large d.c. spatial component. (i.e. magnitude of the spatial variation of the intensity is small compared to the spatial average of the intensity). When the linearization is carried out in two dimensions, the following equation for the space charge field can be derived:

$$\frac{\partial^2 E_{mn}}{\partial t^2} + \left(\frac{1}{\tau_{Re}} + \frac{1}{\tau_{Dmn}} + \frac{1}{\tau_{Ie}} + \frac{1}{\tau_{die}}\right)\frac{\partial E_{mn}}{\partial t}$$
$$+ \left\{\left(\frac{1}{\tau_{Dmn}} + \frac{1}{\tau_{Ie}}\right)\frac{1}{\tau_{die}} + \frac{1}{\tau_{Ie}\tau_{Dmn}}\right\} E_{mn} = \frac{-i\, e\, s(N_D - N_A) I_{mn}}{\tau_{Dmn}\, k_{mn}\, \varepsilon}, \qquad 2.6$$

where $\mathbf{E}_{mn}$, is the space charge field amplitude, that has a grating wave vector, $\mathbf{k}_{mn} = (m\text{-}n)\varepsilon\, \hat{\mathbf{x}} + (m^2 - n^2)\, \varepsilon^2/2\, \hat{\mathbf{z}}$. The total space charge field and the intensity pattern can be expressed in the following Fourier expansions:

$$\mathbf{E}(x,z,t) = \sum_{m,n}{}' \mathbf{E}_{mn}(z,t)\ exp\ [-ik(m\text{-}n)x\varepsilon\ -ik\varepsilon^2(m^2\text{-}n^2)z/2] \qquad 2.7$$

$$I(x,z,t) = I_0 + \sum_{m,n}{}' I_{mn}(z,t)\ exp\ [-ik(m\text{-}n)x\varepsilon\ -ik\varepsilon^2(m^2\text{-}n^2)z/2].$$

The linearization assumption is expressed as: $I_0 >> I_{mn}(z,t)$.

In equation 2.6 the various time constants are defined as: $1/\tau_{\text{die}} = e\mu n_0/(\varepsilon_0\varepsilon)$, $1/\tau_{\text{Re}} = \gamma N_0^+$, $1/\tau_{\text{Dmn}} = k_{mn}^2 k_b T\mu\ /e$, $1/\tau_{\text{Ie}} = s\ (I_0 + I_{\text{dark}}) + \gamma n_0$. The terms with zero subscritps are the spatial averages of respective number densities and they are defined later in this section. Here the time constants τ_{die}, τ_{Re}, τ_{Dmn}, τ_{Ie} are dielectric relaxation time, electron recombination time, diffusion time, sum of production and ion recombination time, respectively. For typical photorefractive crystals, τ_{die} and τ_{Ie} are on the order of milliseconds, while τ_{Re} and τ_{De} are on the order of nanoseconds. We also expect E_{mn} to be a slowly varying function of time (on the order of seconds). From these physical considerations, we neglect the second derivative term relative to $1/\tau_{Re}\ \partial E_{\text{mn}}/\partial t$ and $1/\tau_{\text{die}}$; we also neglect $1/\tau_{Ie}$ relative to $1/\tau_{\text{Dmn}}$ and $1/\tau_{Re}$. With these assumptions equation 2.7 can simplified into a first-order differential equation:

$$\tau_{mn}\frac{\partial E_{mn}}{\partial t} + (1 + I_0/I_{dark})E_{mn} = -i\, I_{mn}/I_{dark}\frac{E_{Dmn}}{(1+E_{Dmn}/E_{qmn})}, \qquad 2.8$$

where $E_{Dmn}=k_{mn}k_B T/e$, $E_{qmn}=eN_A(N_D-N_A)/(\varepsilon k_{mn}N_D)$ are the diffusion field and the limiting space charge field [1], respectively. The time constant, τ_{mn} is the photorefractive (grating) decay time at the equivalent dark irradiance and is given by $\tau_{mn}=\tau_{dark}(1+\tau_{Re}/\tau_{Dmn})/(1 + k_{mn}^2/k_d^2)$, where $k_d = \sqrt{e^2N_A/(\varepsilon k_b T)}$ is the Debye wave number. The equation 2.8 has been used in numerical modeling of number of wave mixing geometries with complicated pump beams [7, 9, 10], some of these studies will be reviewed in the chapters 3 and 4.

Derivation of equation 2.6 presented below is shortly outlined for the first time in ref[7]. We can eliminate $\boldsymbol{j}$ by substituting equation 2.3 into equation 2.2 which gives us three equations for the three unknowns N^+, n, $\mathbf{E}$.. We consider spatial Fourier expansions for the ionized dopant, electron number densities and the space charge field, N^+, n, $\mathbf{E}$:

$$n(x,z,t) = n_0(z,t) + \sum_{m,n}{}' n_{mn}(z,t)\ exp\ [-ik(m-n)x\varepsilon\ -ik\varepsilon^2(m^2-n^2)z/2]$$

$$N^+(x,z,t) = N_0^+(z,t) + \sum_{m,n}{}' N_{mn}^+(z,t)\ exp\ [-ik(m-n)x\varepsilon\ -ik\varepsilon^2(m^2-n^2)z/2] \qquad 2.9$$

$$\mathbf{E}(x,z,t) = \sum_{m,n}{}' \mathbf{E}_{mn}(z,t)\ exp\ [-ik(m-n)x\varepsilon\ -ik\varepsilon^2(m^2-n^2)z/2]\ ,$$

where N_0^+, n_0 are the spatial averages of the acceptor number density, electron number density respectively, and N_{mn}^+,, n_{mn},, $\mathbf{E}_{mn}$ are the Fourier coefficients of the expansions. Note that $\mathbf{E}_{mn}$, space charge field component, point in the direction of the grating wave

vector, $\mathbf{k}_{mn} = (m\text{-}n)\varepsilon\,\hat{\mathbf{x}} + (m^2 - n^2)\,\varepsilon^2/2\,\hat{\mathbf{z}}$ and in general it has both x and z components. In the absence of external electric field and photovoltaic fields, the spatial average of the space charge field is zero, hence $\mathbf{E}_0 = 0$.

We substitute equations 2.9 into 2.1-4, the transport equations and equate separately terms with the same exponential factors. We assume that the electron number density is much less than the acceptor number density ($N_A >> n$). For the typical, cw operating conditions (less than 1 W/cm^2) this assumption is well founded ($N_A \approx 10^{16}$ cm^{-3}, $n_0 \approx 10^{10}$ cm^{-3}). The resulting zeroeth order solutions are $n_0 = s\,(I_0+I_{\text{dark}})(N_D-N_0^+)/(\gamma N_0^+)$, and $N_0^+ = N_A$ where $I_{\text{dark}}=\beta/s$.

In general, we get a complicated set of nonlinear differential equations, for the Fourier coefficients. We linearize the equations by omitting terms of the second or higher order in Fourier coefficients. The set of equations then becomes (with the above zeroth-order solutions):

$$\frac{\partial N^+_{mn}}{\partial t} = s\,(N_D - N_A) I_{\text{dark}}\, I_{mn} - s\, I_{\text{dark}}(1+I_0) N^+_{mn} - \gamma (n_0\, N^+_{mn} + N^+_0\, n_{mn})$$

$$\frac{\partial n_{mn}}{\partial t} = \frac{-i\,k_{mn}\,\mu}{e}\left(e\,n_0\,E_{mn} + i\,k_{mn}\,k_B T\; n_{mn}\right) + \frac{\partial N^+_{mn}}{\partial t} \qquad 2.10$$

$$i\,k_{mn}\,E_{mn} = \left(\frac{e}{\varepsilon\,\varepsilon_0}\right)(n_{mn} - N^+_{mn}),$$

where we neglect terms with $\frac{\partial E_{mn}}{\partial z}$, $\frac{\partial n_{mn}}{\partial z}$ and E_{mn}, k_{mn} are the amplitudes of the corresponding vectors. Manipulating equations 2.10, we eliminate N^+_{mn} and n_{mn}. The result is the sought after second-order differential equation for E_{mn}, equation 2.6.

2.4 Band transport theory with fast electronic recombination

In this section we derive an alternative form for the materials equations 2.1-4 without the linearization assumption. In general it can be shown that for fast electronic recombination (where $dn/dt = 0$, n is the electron number density), the basic material equations can be reduced to a single equation for the space charge field. Here, we only consider the case where a small fraction of the donors are ionized ($N_D >> N_A$) and neglect dark conduction. We also consider the open circuit case where the total current density is zero. With the above assumptions which are thought to be appropriate for a large class of problems, one can derive:

$$i\, e - i\, \alpha^2\, \partial_x^2 e + \alpha\, \partial_x i = -\,(1+\alpha \partial_x e)^2 \partial_t e - e\, i\, \alpha\, \partial_x e - \alpha \partial_x i\, \partial_x e. \qquad 2.11$$

Here, x, t are normalized by the inverse of the transverse component q_0 of a characteristic wave number, and the dielectric relaxation time τ_a, respectively. The space charge field, $e = E_{sc} q / (k_B T k_D)$ is normalized by the amplitude of the maximum field possible, which occurs when the grating wave number is equal to the Debye wave number, k_D. The intensity profile i (not to be confused with $\sqrt{-1}$), is normalized by a characteristic intensity, I_0. Equation 2.11 can be reduced to equation 2.8 when a large spatial d.c. component for the intensity and a fast electronic recombination are assumed. This equation has been used in number of numerical and analytical studies of various wave mixing geometries [9] and will be used in chapter 7 of this work.

Next, we present a sketch of the derivation of 2.11 from the basic material equations 2.1-4. The starting material equations can be expressed as:

$$\partial_t e + n\, e + \partial_x n = 0$$

$$\partial_x e = N^+ - 1 \qquad 2.12\ \text{a-c}$$

$$n\ N^+ = i\,.$$

Here, the acceptor number density N^+ and n are normalized by N_A, the number density of negative ions that compensate for the charge N^+ in the dark, and the zeroth-order solution for the electron number density (n_0 in the previous section), respectively. The first equation, eq(2.12 a) is derived from the continuity equation and Poisson's equation for the open circuit case. The equation states that the total current density (the sum of the displacement, drift and diffusion current densities from left to right) is zero. Eq(2.12 b) is Poisson's equation for fast electronic recombination ($|n_0\, n| << |N_A\ (N^+\text{-}1)|$). The last equation, eq(2.12 c) is derived from the rate equation for the acceptor number density for $N_D >> N_A$.

The acceptor number density can be eliminated from these equations by a simple substitution. Transformed eq(2.12 b), can be solved for the electron number density which in turn can be substituted into eq(2.12 a). Carrying out the spatial derivative for the electron number density and multiplying the equation by $(1 + \partial_x e)^2$ results in the desired equation 2.11.

Equation 2.11 can be thought of as a continuity equation. The time derivative term in this equation arises from the displacement current density. The first term on the left and the second term on the right arise from the drift current density and the remaining terms arise from the diffusion current density.

2.5 Summary:

In section 2.2 we introduced the standard band transport theory that accounts for the basic characteristics of the photorefractive effect. The theory quantifies the photogeneration of charge carriers by excitation from deep donors, the transport of these carriers by diffusion and drift which leads to charge separation, and the build up of space charge field. Section 2.3, and 2.4 introduces simplified versions of the starting material equations 2.1-4. The first one assumes a small spatial fluctuation of the intensity pattern around a mean value. The second one requires that the electron number density be in quasi-steady state. The range of validity of these approximations are discussed. These simplifications of the material equations will be used to model complicated wave mixing geometries in latter chapters. Both of the versions of the material equations have short comings. Clearly the first version cannot be used to model the finite transverse boundary effects and the second one cannot be used for modeling short pulsed illumination.

References for Chapter Two

[1] P. Gunter and J.-P. Hulgnard, Chapter 2, in *Photorefractive Materials and Their Applications,* **Vol. 1**, edited by P. Gunther and J.P. Huignard (Springer-Verlag, Berlin, 1989).

[2] A. Ashkin, G. D. Boyd, J. M. Dziedzic, R. G. Smith, A. A. Ballmann, H. J. Levinstein, and K. Nassau, Appl. Phys. Lett. **9**, 72 (1996).

[3] N. V. Kukhtarev, Pis'ma Zh. Tekh. Fiz. **2**, 1114 (1976) [Sov. Tech. Phys. Lett. **2**, 438 (1976)].

[4] M. B. Klein, R. N. Schwartz, J. Opt. Soc. Am. B, **3**, 293 (1986).

[5] V. F. Belinicher, B. I. Sturman, Sov. Phys. Usp. **23**, 199 (1980).

[6] P. Yeh, *Introduction to Photorefractive Nonlinear Optics* (Wiley-Interscience Publications, 1993).

[7] G. C. Valley, J. Opt. Soc. Am. B **9**, 8 (1992).

[8] A. A. Zozulya, M. Saffman, and D. Z. Anderson, J. Opt. Soc. Am. B 12, 255 (1995).

[9] M. Segev, D. Engin, A. Yariv, G. C. Valley, Opt. Lett. 18, 1828 (1993).

[10] M. Segev, D. Engin, A. Yariv, G. C. Valley, Opt. Lett. 18, 956 (1993).

Chapter three

Fanning simulations

3.1 Introduction

We define unidirectional wave propagation in p.r. crystals as the class of phenomena that can be modeled by one scalar paraxial wave equation and the photorefractive material equations, 2.1-2.4 (diffusion dominated, no photovoltaic field or externally applied field) that were introduced in chapter 2. This class of phenomena involves nearly co-propagating waves interacting through self-written transmission gratings. Two-wave mixing, beam fanning and conical diffractions [1(ch. 2), 2(ch. 4), 3-9] are some of the phenomena that belong to this class. In section 3.2 the coupled mode theory for the two-wave mixing geometry is introduced. The model considers two copropagating plane waves interacting through a single grating. In section 3.3 we will introduce the coupled multiple mode analysis which involves nearly copropagating multiple plane waves which are coupled through multiple transmission gratings. This is a general method that can be used to model any of the unidirectional wave propagation phenomena in 2-D. The fanning phenomenon is briefly reviewed and spatio-temporal simulations, carried out with the generalized coupled mode formulation is described in section 3.4.

3.2 Codirectional degenerate two-wave mixing, coupled mode theory:

The geometry considered is shown in figure 3.1 [2(ch.4)]. Two plane waves are incident on the p.r. crystal. The two beams are coherent and they write a transmission grating, which couples the two beams. For a diffusion dominated p.r. nonlinearity, the phase shift between the writing interference pattern and the index change is $\pi/2$ and this relative phase difference allows the power transfer between the two beams.

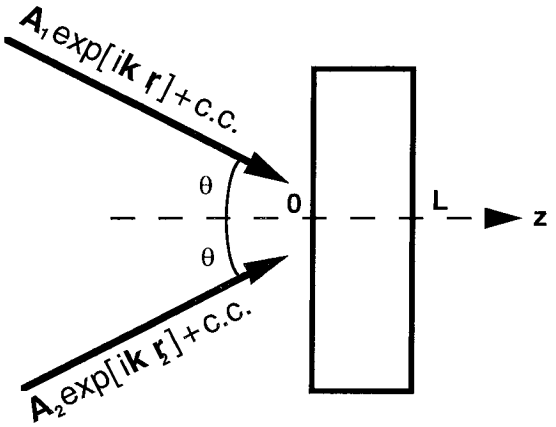

Figure 3.1. A schematic diagram of two-wave mixing in photorefractive materials. If c-axis is perpendicular to z-axis (pointing up), then the energy transfer takes place from the first to the second beam.

The equations governing the slowly varying amplitudes (in z direction) of the two interacting plane waves are:

$$\frac{\partial a_2}{\partial z} = \frac{k\,\gamma_{12}}{n_b\,I_0}|a_1|^2\,a_2$$

$$\frac{\partial a_1}{\partial z} = -\frac{k\,\gamma_{12}}{n_b\,I_0}|a_2|^2\,a_1 \qquad 3.1$$

where I_0 is the total intensity incident on the p.r. crystal and γ_{12} is the coupling constant (real for diffusion dominated material response) between the two beams. The coupling constant has in general a strong dependence on the angle between the beams, angle the beams make to the c-axis and the material parameters such as Debye wave number [13]. The equation describes the process in which the beams propagating through the interaction region diffract from the phase matched grating in the direction of the other beam. Then two waves add in phase (or out of phase) increasing the total energy propagating in the direction of the first wave.

Equation 3.1 can be solved analytically with arbitrary boundary conditions at the input plane. For a very large intensity ratio, $m = \frac{I_1}{I_2}$ the phase of the waves change very little, although the intensity of the waves varies as:

$$I_1 = I_1(0)\frac{1 + m^{-1}}{1 + m^{-1}\exp[\gamma z]}$$

$$I_2 = I_2(0)\frac{1 + m}{1 + m\exp[-\gamma z]} \qquad 3.2$$

where $\gamma = \frac{k\,\gamma_{12}}{n_b\,I_0}$. Clearly, for a larger interaction length more of the energy from the wave one is transferred to wave two and the rate at which the transfer takes place is proportional to γ, the effective coupling constant.

3.3 Coupled multiple mode theory with linear material response

The wave propagation problem can be formulated in the Fourier space. When the linearized material equations are used and the phase matching conditions are required, the resulting equations look similar to the coupled mode theory (CMT). In order to emphasize the similarity we refer to the formulation as coupled multiple mode theory (CMMT). CMT can be viewed as a special case of CMMT where a very selective sampling of the Fourier domain is carried out. The paraxial wave equation formulated in the Fourier space take the following form:

$$\frac{\partial a_p}{\partial z} = \frac{ik}{n_b} \sum_{m,n} \delta n_{mn}\, a_{p+n-m}\, \exp[-ik\varepsilon^2 \Delta_1\, z/2], \qquad 3.3$$

where $\Delta_1 = 2(m-n)(m-p)$, $\Delta_2 = 2(n-p)(n-m)$ are the phase mismatch factors andb_p, a_p are plane wave amplitudes. The expansion of the field amplitude in the Fourier space is given by:

$$A(x,z,t) = \sum_m a_m(z,t)\, \exp[\, -ik\varepsilon mx \; - ik\varepsilon^2 m^2 z/2] \,. \qquad 3.4$$

Structure of equation 3.3 is similar to equation 3.1 except now there are multiple plane waves and each plane wave diffracts off all the transmission gratings. However as depicted by the phase mismatch factors most of the gratings are phase mismatched. A detailed derivation of these equations can be found in [13]. The material equation is derived in section 2.3:

$$\tau_{mn} \frac{\partial \delta n_{mn}}{\partial t} + (1 + I_0/I_{dark}) \delta n_{mn}(z,t) = i\, \gamma_{mn}/I_{dark} \{ a_m(z,t)\, a_n^*(z,t) \}, \qquad 3.5$$

where $I_{mn}(z,t) = a_m(z,t)\, a_n^*(z,t) + c.c.$. Equation 3.5 can be easily inferred from the equation 2.8 by noting that the electro-optic effect can be written as:

$$\delta n_{mn} = -1/2\, n_b^3\, r_{mn} E_{mn} . \qquad 3.6$$

The parameter r_{mn} is an effective linear combination of the electro-optic tensor elements, which depend on crystal orientation, polarization of the beams and the direction of the $\mathbf{E}_{mn}$. In equation 3.5, the coupling constants between the plane wave components are given by:

$$\gamma_{mn} = \pi/\lambda\, n_b^3\, r_{mn} \frac{E_{Dmn}}{(1+E_{Dmn}/E_{qmn})}. \qquad 3.7$$

Functional form of r_{mn} and the relevant values used in this chapter (for $BaTiO_3$) can be found in reference [7]. The parameter r_{mn} has a relatively weak dependence on the angles of propagation, while the factor $\frac{E_{Dmn}}{(1+E_{Dmn}/E_{qmn})}$ has a strong dependence on the grating wave number k_{mn}. As a result the coupling constant has a Lorentzian shape as a function of grating wave number, which peaks at the Debye wave number and has a broad width. The broad angular scattering present in the fanning process is a consequence of the grating wave number dependence of the coupling constant, (section 3.4).

A simplified version equation 3.3 can be attained by neglecting all the phase mismatched terms:

$$\frac{\partial a_p(z,t)}{\partial z} = \frac{ik}{n_b} \sum_n \delta n_{pn}(z,t)\, a_n(z,t). \qquad 3.8$$

In section 3.4 the consequences of this approximation are investigated for fanning. Equation 3.8 and 3.5 can be used to model a number of two-dimensional wave mixing phenomena such as two-wave mixing with arbitrary pump beams, and beam fanning. In

the next section we present numerical simulations studying the beam fanning phenomenon.

3.4 Numerical simulations of beam fanning

Beam fanning is the process of self-induced scattering observed in almost all photorefractive crystals. In its most common manifestation a single beam entering one face of a crystal fans out in the horizontal and/or vertical directions. It is now well established that fanning is an example of stimulated photorefractive scattering and is caused by beam coupling between the incident beam and radiation scattered by inhomogeneities in the entrance face or within the bulk of the crystal [3-9]. The fanned output consists of a bundle of closely spaced filaments figure 1.1, and the bundle has an envelope with a large angular width. Through the linearized material theory we model the spatio-temporal dynamics of the wide envelope. The filamentation can be included only with the full nonlinear material equation [10]. However as shown in reference [7] by comparing experiments with numerical simulations, the steady-state behavior of the envelope seems to be independent of the filamentation process.

A more thorough account of results summarized in this section can be found in reference [11]. The numerical modeling is carried out with equations (3.3 or 3.8) and 3.5. The system of ordinary differential equations are solved by split-step method. First the equations 3.3 is solved for the angular wave amplitude distribution along z for a given index distribution. Then from the calculated wave amplitudes, the index distribution for the next time step is found by solving equations 3.5. The validity of the results are checked by doubling the time and z steps and also by doubling the number of plane waves for given angular window.

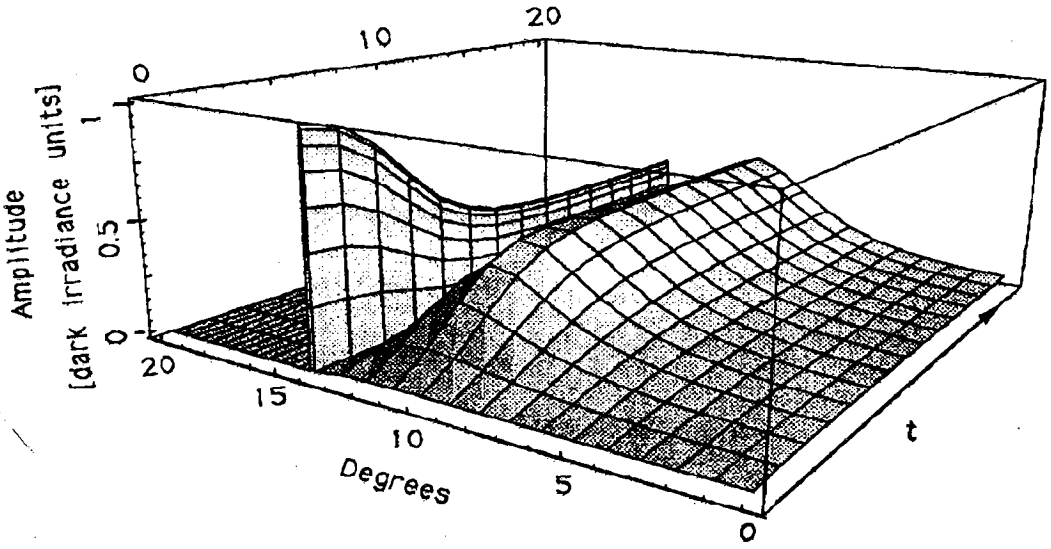

Figure 3.2. Temporal evolution of fanning at the output of a photorefractive crystal characterized by parameters that are typical for $BaTiO_3$. The wave amplitudes are indexed by the angle of propagation measured with respect to the +c-axis.

Figure 3.2 shows temporal behavior of the angular distribution of the waves at the output plane. The initial conditions assume a single plane wave incident at 14 degrees with respect to the +c axis and remaining spectrum consist of spectral noise with average intensity two orders of magnitude less than the pump wave. The wide angular distribution of the fanning envelope remains the same all along the dynamics, with center of the distribution at about 9 degrees and a width of 3 degrees. The dynamics is on the order of typical two-wave mixing dynamics (about 10 times the decay time at the equivalent dark irradiance). The shape of the angular spectrum of the fanned output resembles very much a Lorentzian function reflecting the angular dependence of the coupling constants in equation 3.7. The peak of the angular distribution shifts closer to the +c axis as the interaction length or the average coupling constant is increased. For an infinite interaction length all the input power is expected to be traveling in the +c direction.

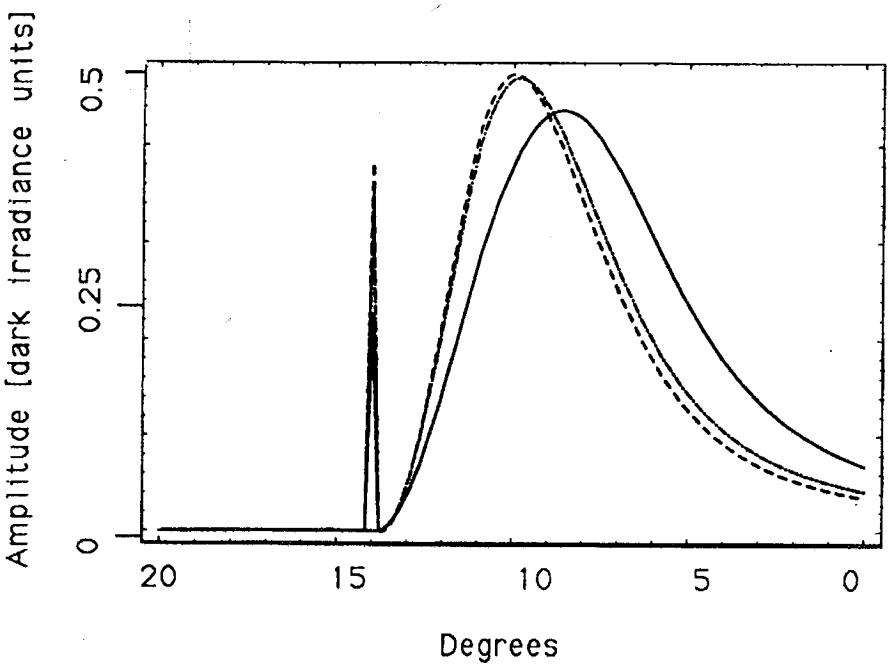

Figure 3.3. Steady-state fanning spectrum at the output of a photorefractive crystal. The dashed curve is case with the crystal seeded by surface scattering. The curve situated very near the dashed curve is the case with scattering centers distributed through out the interaction volume. Solid curve is the case with the crystal seeded by twice the surface scattering present for the dashed curve.

Two alternative models for the noise that starts the fanning process are compared. First one is the surface scattering at the input face which can be modeled as a boundary condition. The second approach is the volume scattering which is modeled by adding a constant term to the paraxial wave equation, equation 3.8. Figure 3.3 shows that with appropriate scaling [11], the two methods give very similar qualitative behavior. Two-wave mixing process as described in section 3.2 predicts an exponential increase in scattered waves. As a result the noise situated at the input plane gets amplified the most

and it is expected to constitute a large part of the fanned output. When the surface noise level is doubled (keeping the total average intensity constant) the output angular distribution changes significantly (figure 3.3). This feature of the surface scattering has been used to initiate fanning in $KNbO_3$ crystal [12].

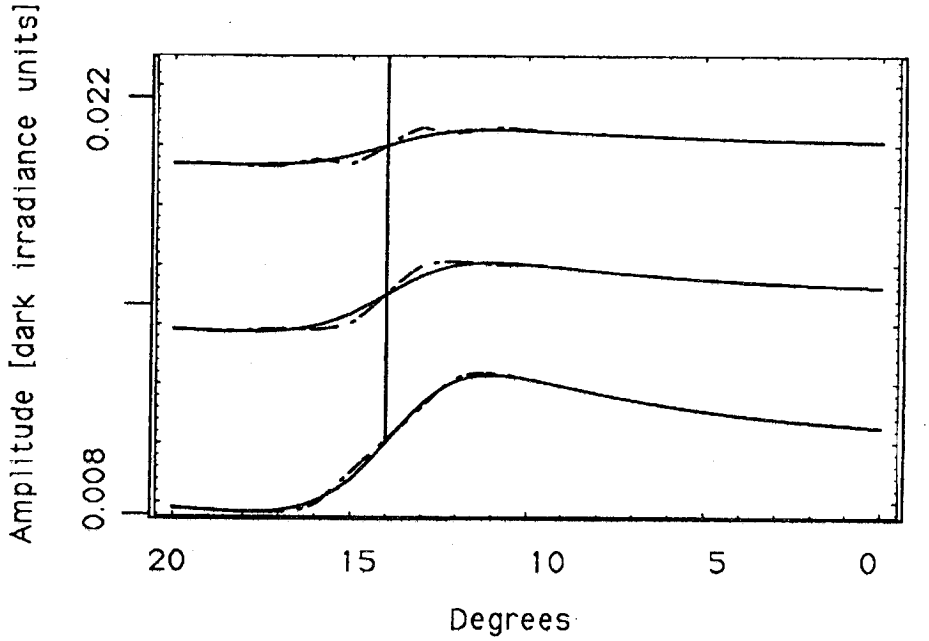

Fig. 3.4. Comparison of the plane-wave amplitudes after propagation of 50 (upper curves), 100 (middle curves), and 200 micrometers (lower curves) with (dashed curves) and without (solid curves) non-phase-matched terms in the wave equation.

The numerical simulations with and without non-phase matched terms are compared for interaction distances L = 50, 100, 200 micrometers (equations 3.3. vs. 3.8). The results in figure 3.4 shows that the two models predict different results only for very small interaction lengths. For interaction lengths of 200 micrometers the two solutions nearly overlay, with the exception of a small ripple. For typical propagation paths of a few millimeters in photorefractive crystals, we conclude that the non-phase-matched terms have little effect on the behavior of beam fanning.

3.5. Summary

Various geometrys for unidirectional wave propagation in photorefractive crystals are considered. Couple mode theory for two-wave mixing is summarized. The analytical solutions to CMT shows that in the diffusion dominated material response one of the beams can be amplified via the energy exchange between the two waves. A coupled multiple mode theory is developed with linearized material response. The resulting equations can be used for modeling various phenomena such as beam fanning and two-wave mixing with arbitrary pump waves. The numerical simulations of spatio-temporal behavior of beam fanning is described. Fanning exhibits quick dynamics where the angular distribution is nearly independent of time. The fanned output strongly depends on the seeding level. The location of the scatterers (volume or surface) result in similar qualitative behavior, and the seeding can be modeled as a boundary condition at the input plane. Phase-mismatched terms in equation 3.3 have very small effect on the fanning output, and these terms can be neglected for interaction lengths larger than few hundred microns..

References for Chapter Three

[1] P. Gunter and J.-P. Hulgnard, Chapter 2, in Photorefractive Materials and Their Applications, **Vol. 2**, edited by P. Gunther and J.P. Huignard (Springer-Verlag, Berlin, 1989).

[2] P. Yeh, *Introduction to Photorefractive Nonlinear Optics* (Wiley-Interscience Publications, 1993).

[3] V. V. Voronov, I. R. Dorosh, Y. S. Kuz'minov, and N. V. Tkachenko, Kvantovaya Elektron. (Moscow) 7, 2313 (1980) [Soy. J. Quantum Electron. 10, 1346 (1980)].

[4] V. V. Obukhovskii and A. V. Stoyanov, Kvantovaya Elektron. (Moscow) 12, 563 (1985) [Soy. J. Quantum Electron. 16, 367 (1985)].

[5] R. A. Rupp and F. W. Drees, Appl. Phys. B 39, 223 (1986).

[6] G. Zhang, Q. X. Li, P. P. Ho, S. Liu, Z. K. Wu, and R. R. Alfano, Appl. Opt. 25, 2955 (1986).

[7] M. Segev, Y. Ophir, and B. Fischer, Opt. Commun. 77, 265 (1990).

[8]. G. C. Valley, J. Opt. Soc. Am. B 4, 14 (1987); erratum 4, 934 (1987).

[9] T. R. Moore and D. L. Walters, J. Opt. Soc. Am. B 6, 1806 (1988).

[10] A. A. Zozulya, M. Saffman, D. Z. Anderson, Phys. Rev. Lett., **73**, 6, 818 (1994).

[11] M. Segev, D. Engin, A. Yariv, G. C. Valley, Opt. Lett., **18**, 12, 956 (1993).

[12] P. Gunter, E. Voit, M. Z. Zha, and J. Albers, Opt.Commun. 66, 210 (1985).

[13] D. Engin M. Segev, S. Orlov, A. Yriv, G. C. Valley, J. Opt. Soc. Am. B. **11**, 9, 1708 (1994).

Chapter four

Competition between double phase conjugation and fanning, and the study of conjugation fidelity; simulations

4.1 Introduction

Double phase conjugate mirror (DPCM) is a unique device in which the two mutually incoherent pump beams are phase conjugated simultaneously [1]. It belongs to a class of phase conjugators called the mutually pumped phase conjugators (MPPC) [2(ch.6)]. From a theoretical point of view the double phase conjugate mirror is considered to be the most simple among the MPPC's. In DPCM pump beams nearly counter propagate. The geometries for various (MPPC) are shown in figure 4.1.

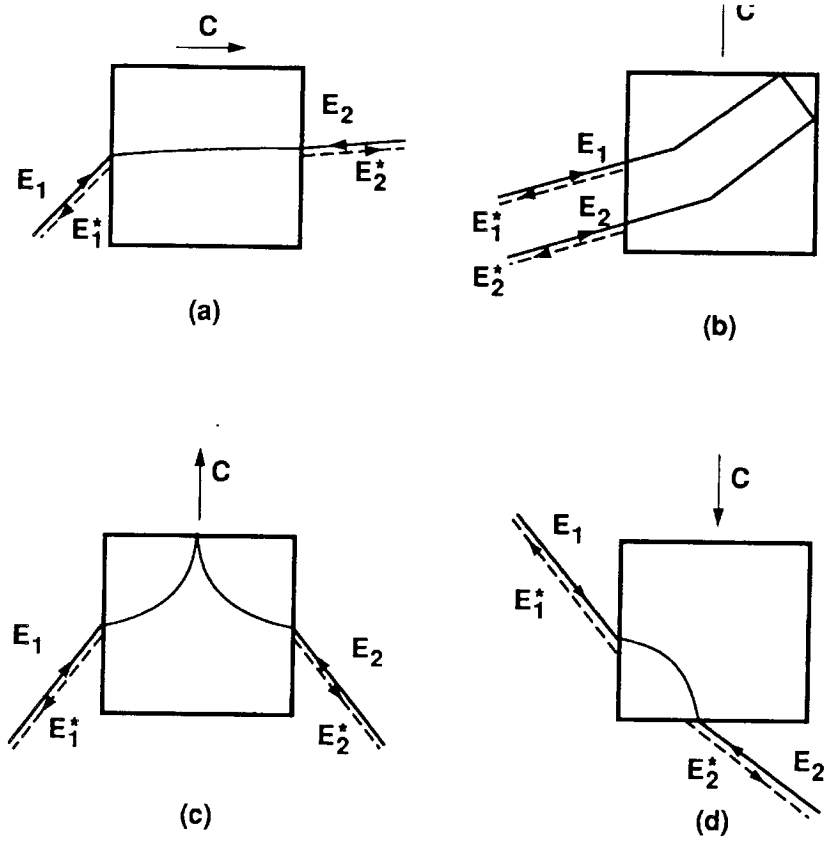

Figure 4.1. Various MPPC geometries [2, ch. 6]. (a) the double phase conjugate mirror, (b) the mutually incoherent beam coupling [3], (c) the bird-wing phase conjugator [4], (d) the bridge phase conjugator [5].

The ability to couple two incoherent beams with phase conjugation characteristics make this device an attractive candidate for spatially coupling two sources that have small numerical apertures. Some particular device applications are image processors [6, 7], multimode-to-single mode fiber couplers [8], phase conjugate interferometers [9], and coupled laser devices [10].

The basic description of the phenomenon is as follows: two mutually incoherent, nearly counterpropagating pumps are incident on to a photorefractive crystal. Since the two pump beams are mutually incoherent, they cannot write reflection gratings. However each

beam, in the absence of the other, is unstable and fans, i.e. the noise present due to imperfections in the material gets amplified, resulting in noisy transmission gratings and a broad angular scattering of the incident beam (section 3.4). When the two beams are present the instability becomes much more selective. The selectivity arises due to an efficient grating sharing process. For each pump beam there is a large set of possible transmission gratings that can become unstable. But only one grating (for plane wave pumps) corresponding to a unique wave number belongs to both of these sets, i.e. it is shared by the counterpropagating waves (figure 4.2.). The above geometry was considered for the first time as a model for the Double Phase Conjugate Mirror (DPCM) in the one-dimensional theory (1-D) theory [1].

The coupled mode (1-D) theory that will be discussed in section 4.2 identifies the basic physics of grating sharing process. However, the plane wave theory can say very little about the quality of phase conjugation. From the applications point of view quantifying conjugation fidelity and the factors effecting the fidelity are of prime importance. For this reason various two-dimensional numerical models have been developed [11-15]. One of the approaches is described in sections 4.3-8, where the problem is formulated in the Fourier space and a linearized material response is assumed. The resulting coupled multiple mode equation is solved numerically and the quality of phase conjugation is studied under various system parameters, such differing seeding levels and input pump ratios. Numerical simulations illustrate the competition of phase conjugation and fanning processes.

4.2 Coupled mode theory for double phase conjugate mirror, (1-D theory)

This simple 4-wave mixing model was first proposed by DPCM's coinventors [1]. The model identifies the grating sharing process as the mechanism that leads to the phase

conjugate outputs. The k-space picture of the 4-wave mixing process is shown in figure 4.2.

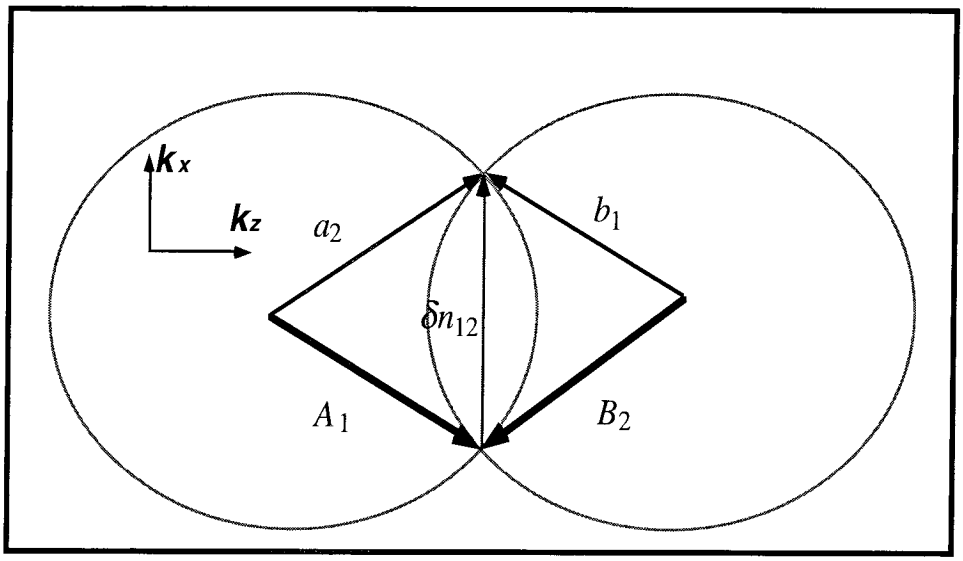

Figure 4.2. k-space picture of the 4 wave mixing geometry in DPCM, pump beams are shown with thick k-vectors.

Each pump wave goes through a two-wave mixing process with a nearly copropagating seed wave via a transmission grating (section 3.2). The grating sharing process refers to the fact that the same transmission grating is written by the counterpropagating waves. The process can be quantified through a coupled mode theory approach:

$$\tau_{12}\frac{\partial \delta n_{12}}{\partial t}+(1 + I_0/I_{dark})\delta n_{12}(z,t) = i\,\gamma_{12}/I_{dark}\{\, a_1(z,t)\, a_2^*(z,t)+b_2(z,t)\, b_1^*(z,t)\,\}$$

$$\frac{\partial A_1(z,t)}{\partial z} = \frac{ik}{n_b}\,\delta n_{12}(z,t)\; a_2(z,t)$$

$$\frac{\partial a_2(z,t)}{\partial z} = -\frac{ik}{n_b}\,\delta n_{12}(z,t)\; A_1(z,t)$$

$$\frac{\partial b_1(z,t)}{\partial z} = -\frac{ik}{n_b}\delta n_{12}(z,t)\ B_2(z,t)$$

$$\frac{\partial B_2(z,t)}{\partial z} = \frac{ik}{n_b}\delta n_{12}(z,t)\ b_1(z,t), \qquad 4.1$$

where the boundary conditions are such that at the respective input planes the seed beams are very small compared to the pump beams. The steady-state solution to equation 4.1 can be found exactly [2(ch.6)]. For the case of equal pump intensities one gets the following transcendental equation for the square root of the reflectivity, $\rho = |a_2/B_2| = |b_1/A_1|$:

$$\rho - s = \tanh[\rho\ \gamma L/(\gamma L)_c] \qquad 4.2$$

where a small seed, s, level is included in the model as a boundary condition for the scattered waves. It is important to note that the seed level corresponds to the component of the noise corresponding to the phase conjugate mode.

It is instructive to expand equation 4.2 for small $\varepsilon = \frac{(\gamma L - (\gamma L)_c)}{(\gamma L)_c}$ and reflectivity:

$$0 = \rho\ [\varepsilon - |\rho|^2] - s. \qquad 4.3$$

When the seed level is set to zero, equation 4.3 has only a uniform, zero solution for gain values below the threshold, $(\gamma L)_c$ (or $\varepsilon < 0$). Above the threshold a solution with finite reflectivity is realized. In this regime the reflectivity, $|\rho|^2$ increases linearly with gain, ε. In the presence of seeding, a finite output exists even below the threshold. Very near the threshold the component of the seeding is amplified as $\rho = s/\varepsilon$. For small seed levels the reflectivity output is unaffected by the seed level. For larger gain values reflectivity saturates due to depletion of the pump beams.

Linearizing equations 4.1 through the undepleted pump approximation gives the following time dependent solutions for the scattered wave amplitudes and the shared transmission grating amplitude above the threshold:

$$\begin{pmatrix} |a_2| \\ |b_1| \\ |\delta n_{12}| \end{pmatrix} = \sqrt{\varepsilon} \begin{pmatrix} z \\ (L-z) \\ 1 \end{pmatrix} \exp[\varepsilon\, t] \qquad 4.4$$

where the wave amplitudes are normalized by the pump beam intensities. Above the threshold the phase conjugate mode is unstable and it exponentially grows in time. The growth rate changes sign at the threshold. Below the threshold the growth rate is negative. If the seeding is turned off, the phase conjugate output decays to zero. In the presence of c.w. seeding (small) the reflectivity follows: $\rho = s/\varepsilon\,(1 - \exp[\varepsilon\, t])$. At the threshold the dynamics become very slow. The slowest dynamic is expected to be at the threshold. This point will become important for identifying the threshold in the numerical simulations.

The above model can be modified for the other interesting cases where the pump intensities are unequal and for the case of differing pump (optical) frequencies. For the case of unequal pump intensities the model predicts a higher threshold and for the case of differing frequencies it predicts the beam steering phenomena. Experimentally, in both of these practical cases the quality of phase conjugation deteriorate as the asymmetry between the pump beams is increased. Often finite reflectivities with poor phase conjugate qualities are realized. Because the 1-D theory only considers plane wave pump beams, it cannot address the question of conjugation fidelity. As it will be shown in the following sections, it is possible to address conjugation fidelity with pump waves consisting of few plane wave components.

4.3. Coupled multiple mode theory with linearized material response

The paraxial wave equations for the two set of counterpropagating waves can be formulated in the Fourier space (see equation 3.3):

$$\frac{\partial a_p}{\partial z} = \frac{ik}{n_b} \sum_{m,n} \delta n_{mn}\, a_{p+n-m}\, \exp[-ik\varepsilon^2 \Delta_1\, z/2]$$

$$\frac{\partial b_p}{\partial z} = \frac{-ik}{n_b} \sum_{m,n} \delta n_{mn}\, b_{p-n+m}\, \exp[ik\varepsilon^2 \Delta_2\, z/2], \qquad 4.5$$

where the counter propagating wave amplitudes are expanded in spatial Fourier domain:

$$A(x,z,t) = \sum_m a_m(z,t)\, \exp[\, -ik\varepsilon mx \, - \, ik\varepsilon^2 m^2 z/2]$$

$$B(x,z,t) = \sum_m b_m(z,t)\, \exp[\, ik\varepsilon mx \, + \, ik\varepsilon^2 m^2 z/2] \qquad 4.6$$

$$\delta n(x,z,t) = \sum_{m,n} \delta n_{mn}(z,t)\ \ exp[-ik(m-n)x\varepsilon \, - \, ik\varepsilon^2 (m^2 - n^2) z/2].$$

The detailed derivation of equations 4.5 can be found in [16]. The expansion for the change in the index of refraction has the form of $A\,A^*$ and $B\,B^*$. When the phase mismatch terms are neglected in equation 4.5, the equation takes a simpler form:

$$\frac{\partial a_p(z,t)}{\partial z} = \frac{ik}{n_b} \sum_n \delta n_{pn}(z,t)\, a_n(z,t)$$

$$\frac{\partial b_p(z,t)}{\partial z} = \frac{-ik}{n_b} \sum_n \delta n_{np}(z,t)\, b_n(z,t). \qquad 4.7$$

As in the fanning simulations the linearized material response is assumed for the multiple plane wave analysis.

$$\tau_{mn}\frac{\partial \delta n_{mn}}{\partial t}+(1 + I_0/I_{dark})\delta n_{mn}(z,t) = i\,\gamma_{mn}/I_{dark}\{ a_m(z,t)\, a_n^*(z,t)+b_n(z,t)\, b_m^*(z,t) \}$$

4.8

The set of equations 4.7 and 4.8 can be used to model any bi-directional multiple wave propagation problem where the counterpropagating waves are mutually incoherent. The equations are solved in a fashion similar to the unidirectional propagation simulations described in chapter 3. For a given index distribution equations 4.7 can be solved for the wave amplitudes. Equation 4.8 can then be solved for index changes for the next time step from the calculated wave amplitudes. The computation cycle is repeated until solution comes a steady state. In the next section we will show the results of simulations carried out for the double phase conjugate mirror.

4.4. Coupled multiple mode theory simulations for the double phase conjugate mirror, introduction:

Equations 4.7 and 4.8 with the boundary conditions are solved numerically using the split-step method. The results in this section and in the subsequent sections can be found in reference 16. We used 21 plane waves separated by 0.5 degrees, covering a total angular spectrum of 10 degrees. We verify the validity of our results by doubling the number of integration steps in time and space, and by doubling the number of plane waves (for the same angular spectrum).

Figure 4.1a shows the configuration of the DPCM device and the orientations of the beams and the crystal. In agreement with the usual experimental conditions, the z axis (the principle optical axes) is not parallel to the c axis (we used an angular separation of 12 degrees between the two axes), to obtain a higher gain [17].

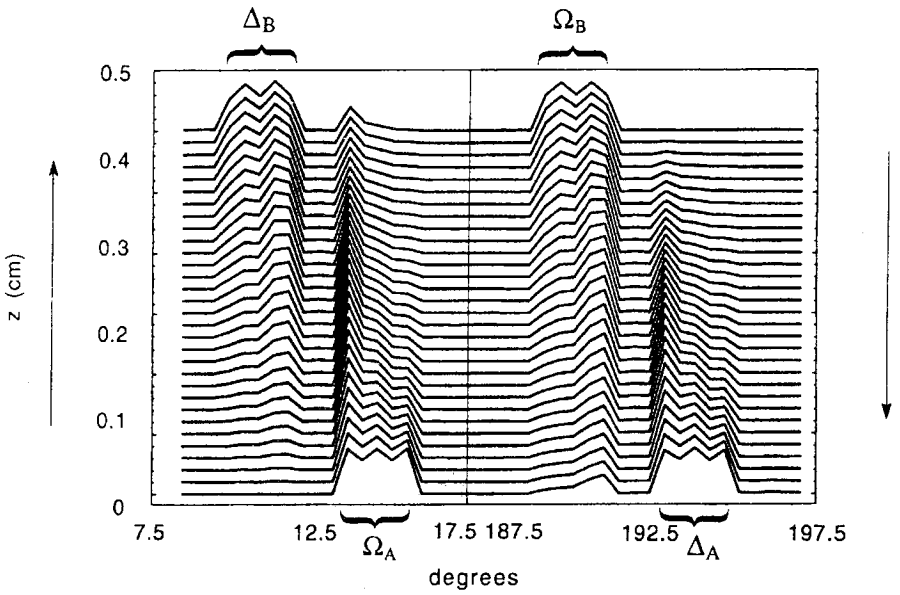

Figure 4.3 illustrates the steady-state far-field amplitudes of the two beams as functions of the propagation direction (z). In figure 4.3a all the angles are measured from the forward c-axis. At the input plane (z=0 for beam A and z=L for beam B) each beam consists of 5 plane waves (spanning an angular width of 2 degrees) with an average amplitude of approximately 1. The remaining plane waves are taken to be "white" noise with constant amplitude (10^{-3}) and pseudo random phase (between π and-π).

As each beam propagates through the crystal, it diffracts and evolves into the phase conjugate of the other beam (top left and bottom right). We refer to the plane waves that make up the phase conjugate beams as Δ_A, Δ_B (phase conjugates of beams A and B, respectively).

In figure 4.4, we refer to the 5 plane waves that initially make up the "image" borne on each beam as Ω_A, Ω_B (for beams A and B, respectively). In Figure 4.4 the input beams are top right (Ω_B) and bottom left (Ω_A). Note that the phase-reversed image acquires an additional bias phase (in this figure, it is approximately 10 degrees) which has been also observed experimentally [18].

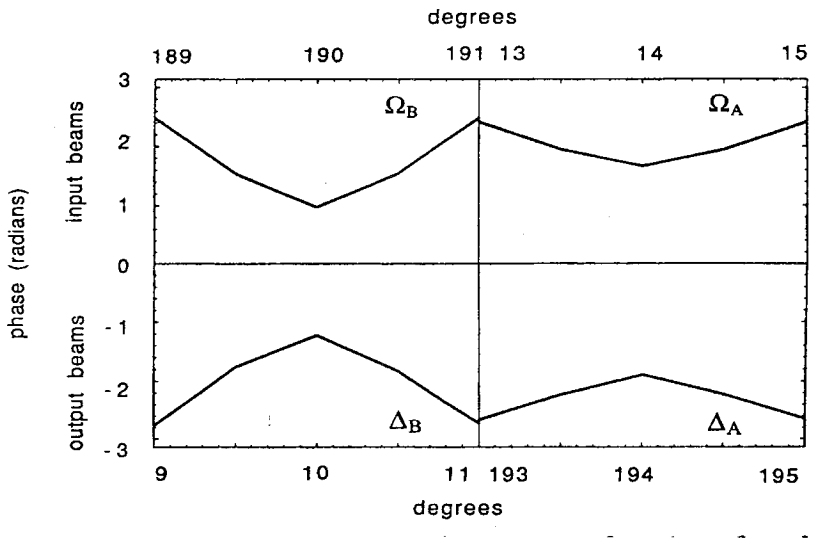

Figure 4.4 illustrates the phase profiles of the steady-state input and output beams (phase conjugated) at z=0 and z=L (plane waves that belong to the image portions of the beams, i.e. Ω_A, Ω_B, Δ_A, Δ_B, are shown only).

Figure 4.3, and 4.4 shows the basic results of the coupled multiple mode simulations for DPCM. The phase conjugation can be realized with pump beams consisting of few plane waves.

4.5 Conjugation fidelity (quality of phase conjugation) vs. reflectivity, simulations

In this section various differences between phase conjugate fidelity (C.F) and the phase conjugate reflectivity (C.R) will be shown. C.R. measures the energy output of the device, however it cannot differentiate between the noise and the signal components of this output. C.F. is the spatial correlation of the pump and phase conjugate output and it has the ability to quantify the quality of phase conjugation. These figures of merits are defined in the following way:

$$T_B(t) = \frac{\sum_{i \varepsilon \Delta_A} |b_i(0,t)|^2}{\sum_{i \varepsilon \Omega_B} |b_i(L,0)|^2} \qquad 4.9$$

$$CR_B(t) = \frac{\sum_{i \varepsilon \Delta_B} |a_i(L,t)|^2}{\sum_{i \varepsilon \Omega_B} |b_i(L,0)|^2}$$

$$CF_B(t) = \frac{\sum_{i \varepsilon \Omega_B \cup \Delta_B} a_i(L,t) b_i(L)}{\sqrt{\sum_{i \varepsilon \Delta_B} |a_i(L,t)|^2 \sum_{i \varepsilon \Omega_B} |b_i(L)|^2}},$$

where T_B, CR_b, CF_b, are the intensity transmission, conjugate reflectivity, and conjugate fidelity of beam B, respectively. The sums are taken over the sets of plane waves Ω_A, Ω_B, Δ_A, Δ_B, which are defined in the previous paragraph and are illustrated in Figures 4.3 and 4.4. Conjugation reflectivity and intensity transmission are defined in an analogous manner to the 1-D theory and as it will be shown in the later sections, many of the predictions of the 1-D theory are found in the coupled multiple mode simulation. Conjugation fidelity can be defined only when the pump waves have multiple plane wave components. C.F. is a complex number and perfect conjugation is realized when the amplitude of the conjugation fidelity is equal to unity. Similar functions for beam A can be realized by interchanging (a_i's and b_i's), (Ω_A and Ω_B), (Δ_A and Δ_B) and (z=L and z=0) in equations 4.9.

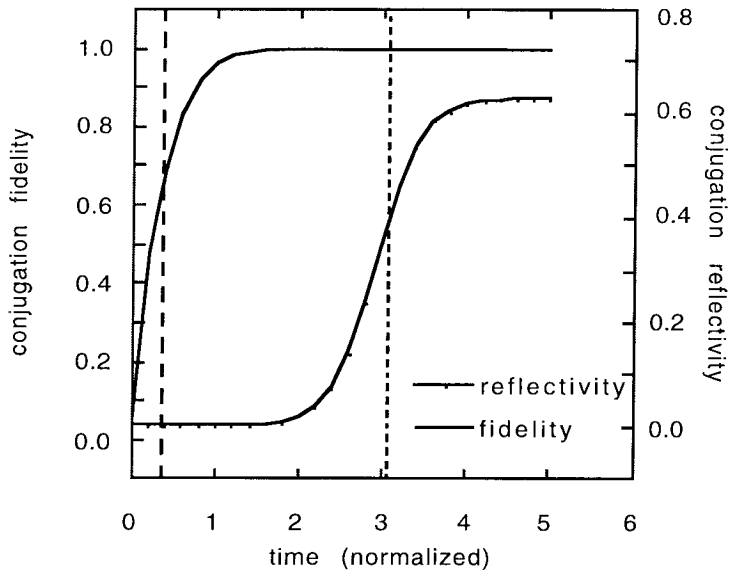

Figure 4.5 illustrates the temporal evolution of fidelity and reflectivity. Conjugation fidelity achieves a steady-state value before the conjugation reflectivity.

Figure 4.5 shows the temporal evolution of conjugation fidelity and reflectivity. Conjugation fidelity achieves a large value, relatively early in the dynamics when the conjugation reflectivity is still small. From this observation, we conclude that phase conjugate mode is favored (sees the most gain) even in the linear regime, when the pump beams are not depleted. We note that the functional behavior of the reflectivity dynamics is qualitatively very similar to the predictions of 1-D theory. Temporal evolution of the conjugation fidelity resembles an exponential behavior. Dynamics exhibited by C.F. and C.R. goes along with observations in experiments, chapter 5. Typically the information on the phase conjugate beams become recognizable significantly before the reflectivity achieves a steady-state value.

Multiple runs for different gain values are carried out, with the same pump beams that are illustrated in figures 4.4, 4.3. The seed to beam intensity ratio is 10^{-6}. The steady-state values for C.F and C.R. are shown in figure 4.6. As predicted by 1-D theory, conjugation reflectivity exhibits a threshold behavior and increases linearly with gain for

small reflectivity values. The threshold value can be determined from the figure 4.5 as 1.2. Note that this value is different from 2, which is the prediction of the 1-D theory.

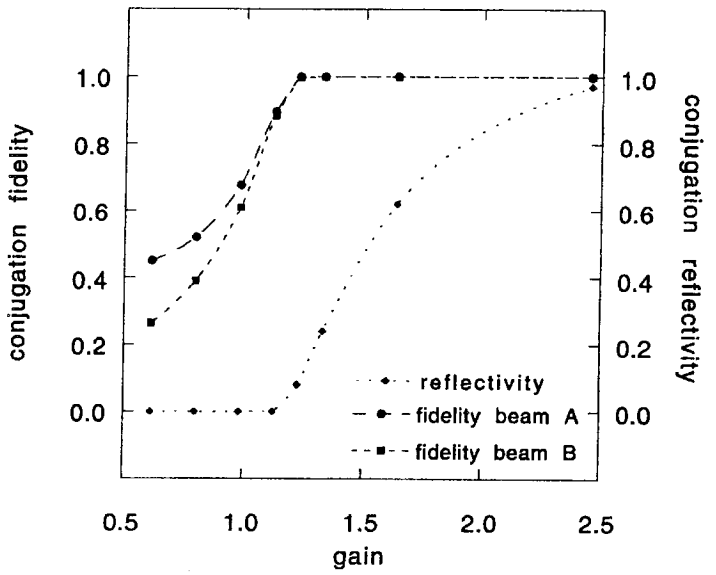

Figure 4.6 shows the steady-state conjugation fidelities (for both beams) and the conjugation reflectivity as functions of gain. $\gamma_0 L$ (coupling-coefficient times length product, or gain), where γ_0 is the coupling coefficient between the central spatial components of the two beams.

Conjugation fidelity on the other hand achieves very large values at the threshold and it increases monotonicaly for gain values below the threshold. The monotonic increase of the fidelity below the threshold can be understood within the frame work of 1-D theory. The component of the seeding that correspond to the phase conjugate mode is expected to be amplified by a factor $1/\varepsilon$ below the threshold. So as the threshold is approached the phase conjugate mode is amplified more strongly than the other linear modes and a sharper increase in conjugation fidelity is observed.

For phase and amplitude information on the pump beams other than the once in figure 4.3 and 4.4, different thresholds are obtained. This way we were able to get a range of thresholds between 0.5 and 2.0, however we were not able to understand the

dependence. A square wave with flat phase profile acts just like the coupled mode theory (1-D), section 4.2 with a gain threshold of 2. As discussed in chapter 5, the dependence of the threshold on the spatial information carried by the beams is observed in the experiments [19].

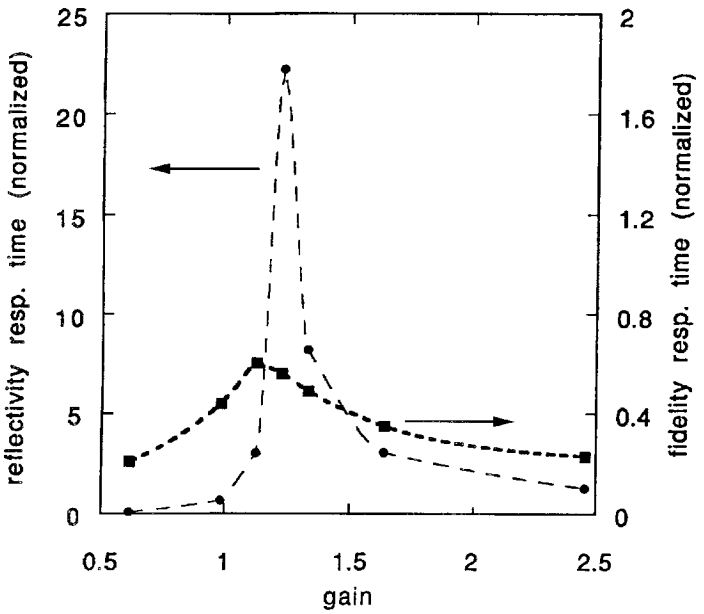

Figure 4.7 fidelity and reflectivity response times versus gain.

The temporal response times of C.F. and C.R. as functions of gain are shown in figure 4.7. For all the gain values conjugation fidelity achieves a large value much earlier than the conjugation reflectivity. The slowing down of the dynamics at the threshold predicted by the 1-D theory is apparent for conjugation reflectivity. A less obvious peaking of the conjugation fidelity response time is also present at gain value smaller than the threshold.

4.6 Effects of spatial noise (seeding), simulations:

Increasing the amplitude of the seed levels, flattens the threshold characteristics of DPCM.

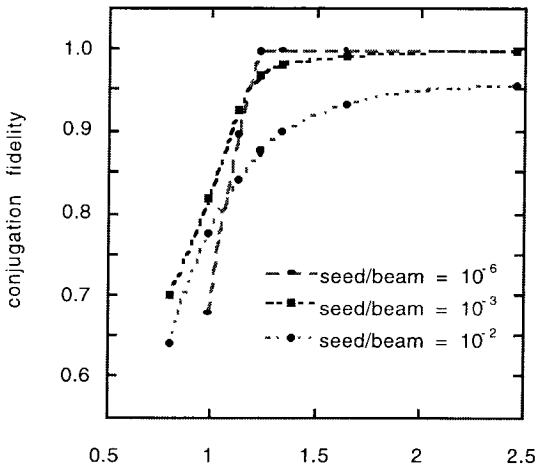

Figure 4.8 illustrates fidelity as a function of gain for three different seed levels (seed/beam intensity ratio of 10^{-2}, 10^{-3}, 10^{-6}).

Conjugation fidelity as a function of gain for three different seed levels is shown in figure 4.8. For small seed levels the effect of increased seeding is only apparent near the threshold. The sharp corner exhibited at the threshold, flattens as the seed level is increased. More fanning is expected for larger seed levels, section 3.4. Near the threshold the reflectivity due to the phase conjugate output is small and the increased contribution from fanning shows up as a decrease in conjugation fidelity. At very large seed levels phase conjugate output itself begins to fan, resulting in poor conjugation fidelity for even large gain values.

For small seed levels the effect on reflectivity is only visible near the threshold where the sharp behavior is smoothened, figure (4.9a). 1-D theory predicts a reflectivity output proportional to the square of the seed level below the threshold. Such dependence is expected to result in smoothening of the reflectivity threshold. However, primarily the component of the noise that corresponds to the phase conjugate mode is expected to be amplified below the threshold, and the decrease in conjugation fidelity as observed in figure 4.8 is not expected. From both observations we conclude that the contribution from

fanning exists for these seed levels. For very large seed levels the reflectivities are smaller than the ones obtained for lower seed levels (at large gain values). At these large seed levels the phase conjugate output itself fans, resulting in lower reflectivities.

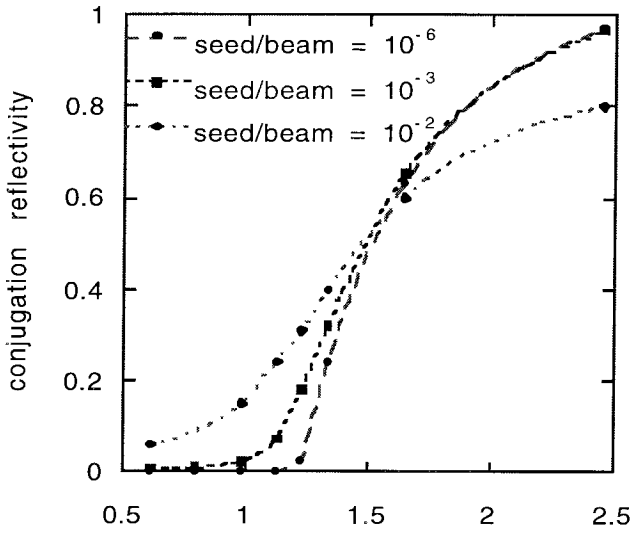

Figure 4.9a illustrates reflectivity as a function of gain for the above seed levels.

Response time for conjugation reflectivity as a function of gain is studied for different seed levels, figure 4.10. In accordance with 1-D theory, the response time of the reflectivity is reduced for larger seed levels. Again the most dramatic changes are observed around the threshold, where the peaking of the response time is less apparent. However the peak gain value does not change. We find that in our simulations obtaining the threshold gain value from the reflectivity dynamics is more reliable.

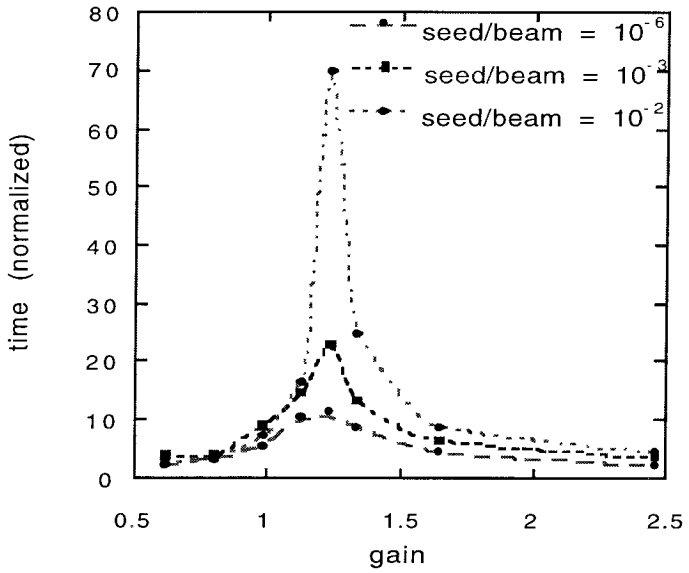

figure 4.9b. reflectivity response time vs. gain for three different seed levels.

4.7 Effects due to intensity ratio of the pump beams and asymmetric phase conjugation, simulations

Asymmetric phase conjugation is observed in experiments when the pump beams have different intensities. This is a practically important case, and for many of the applications, worsening of the conjugation fidelity in asymmetric pumps, limits the usefulness of the device.

Varying the intensity ratios for the pump beams result in a shift of the threshold as it was predicted by the 1-D theory. Looking at the peaks of the reflectivity response time versus gain curves (figure 4.10a), we determine the new thresholds as 1.25, 1.55, 1.85, and 2.1 for increasing intensity ratio, respectively. For the same intensity ratios 1-D theory predicts smaller shifts in the threshold: 1.25, 1.37, 1.56, 1.71. From these results, we conclude that the shift in the threshold just like the threshold value itself seems to

depend on the information borne by the pump beams. In figure 4.10, the flattening of the transmission-gain curve and the reduced peaking of the reflectivity response time-gain curve are interpreted as the manifestations of the increasing fanning activity for larger intensity ratios.

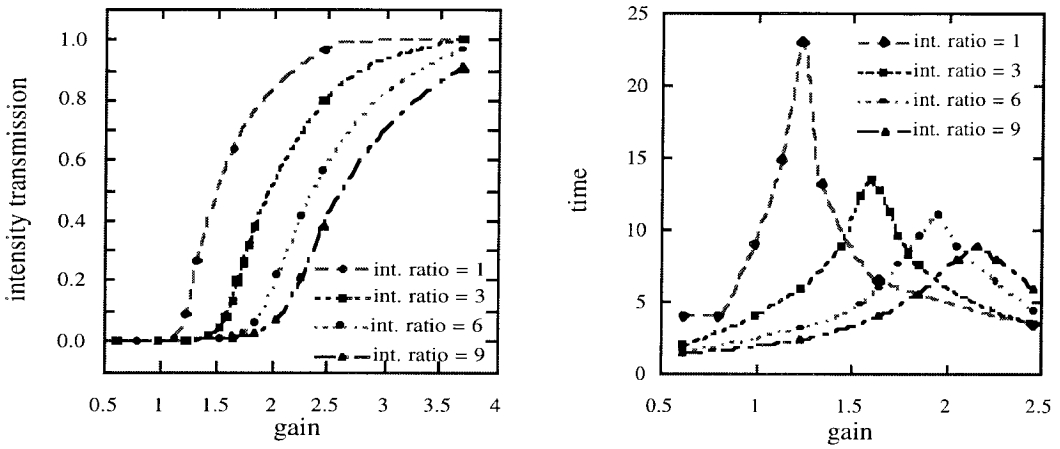

Figure 4.10. intensity transmission vs. gain and reflectivity response time vs. gain curves for various input pump intensity ratios. The seed waves propagating with the weak beam are proportionally weaker than the seed waves propagating with the stronger beam.

Varying the intensity ratio of the two beams strongly affects the fidelity-gain curves for the two beams (figure 4.11). The weaker beam is conjugated more poorly at a given gain value. Notice that the conjugation fidelity on the side of the strong input beam is slightly flattened for larger intensity ratios, but the threshold seems unaffected. On the other hand, the fidelity on the side of the weak input beam is not only flattened but also shifted towards higher gain values. The result is a consequence of the asymmetric fanning process. The strong beam fans more, and as a result the weak beam is more poorly phase conjugated.

The asymmetric phase conjugation has been observed experimentally [19]. The stronger beam bleaches the fanning gratings of the weak beam and enables relatively high

conjugation quality on its input side. The opposite process, however, is inefficient. The weak beam is not able to eliminate the appearance of fanning gratings that are generated by the interaction of the strong beam with the seed noise.

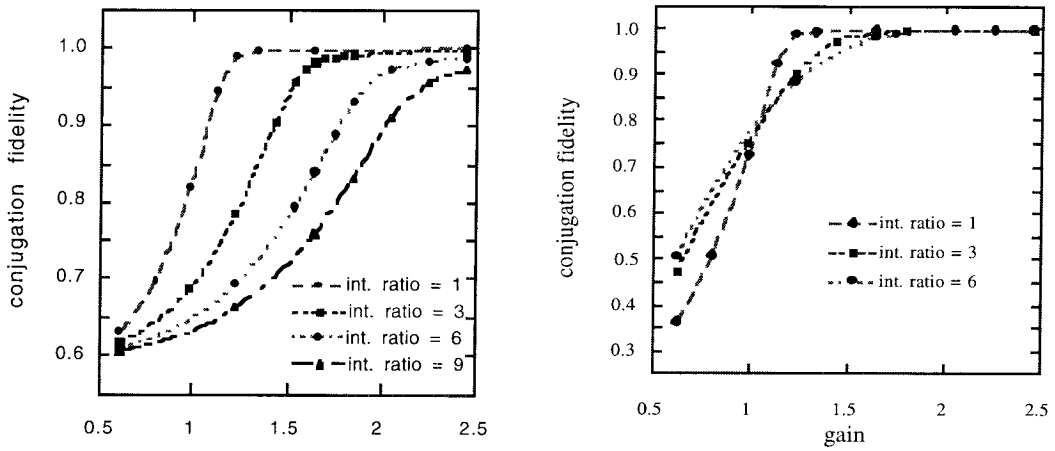

Figures 4.11 fidelity-gain curves for intensity ratios of 1, 3, 6, and 9. The conjugation is significantly asymmetric; weak beam on the right and strong beam on the left.

4.8 Summary and conclusions

We introduce the geometry of the DPCM and summarize the results the coupled mode theory, 1-D theory. When the problem is formulated in the Fourier space, the problem takes the form a coupled multiple mode theory. This formulation allows the study of phase conjugation process with complicated pump beam structures. The simulations show various competition effects between the fanning process and the phase conjugation. The competition results in reduced conjugation quality which is quantified as conjugation fidelity. We find that the conjugation fidelity exhibits a sharp threshold, as a function of coupling constant, signifying dominance of the phase conjugate mode both in the linear regime and the non-linear regime. We find that effects of the spatial noise (seeding) on the

conjugation fidelity is only noticeable below the threshold. We predict the asymmetric phase conjugation when the pump waves have different intensities, as observed in the experiment, section 5.4. The stronger beam fans more, resulting in poorer conjugation quality on the input side of the weaker beam.

It should be mentioned here that some of the quantitative aspects of the interaction were not recovered when the sampling of the spatial frequencies was doubled [16]. However the qualitative behaviors were the same. A careful study of the various sampling strategies can be useful in this approach, i.e. sampling more densely near the pump and phase conjugate beams may be appropriate. Also less dense sampling may be appropriate for modeling fanning process. These strategies ultimately may lead to simple, but informative coupled multiple mode theories that include only few spatial frequency components.

References for Chapter Four

(1) S. Weiss, S. Sternklar and B. Fischer, Opt. Lett. 12, 114 (1987), Appl. Phys. Lett.50, 483 (1987) and Opt. Eng. 26, 423 (1987).

[2] P. Yeh, Introduction to Photorefractive Nonlinear Optics (Wiley-Interscience Publications, 1993).

[3] R. W. Eason and A. M. C. Smout, Opt. Lett. 12, 51 (1997).

[4] M. D. Ewbank, Topical Meetings on Photorefractive Materials, /Effects, and Devies. Technical Digest Vol. 17 (OSA, 1987), pp. 179.

[5] D. Wang, Z. Zhang, Y. Zhu, S. Zhang, P. Ye, Opt. Comm. 73, 495 (1989).

[6] S. K. Kwong, G. A. Rakuljic, and A. Yariv, Appl. Phys. Lett. 48, 201 (1986).

[7] R. J. Anderson, E. J. Sharp, G. L. Wood, W. W. Clark, Q. Vuong, G. J. Salamo,and R. R. Neurgaonkar, Opt. Lett. 18, 986 (1993).

[8] A. Chiou, P. Yeh, C. Yang, and C. Gu, Opt. Lett. 20, 1125 (1995).

[9] J. Feinberg, Opt. Lett. 8, 569 (1983).

[10] S. Sternklar, S. Weiss, M. Segev, and B. Fischer, Opt. Lett. 11, 528 (1986).

[11] A. A. Zozulya, Opt. Lett. 16, 545(1991); V. V. Eliseev, V. T. Tikchoncuk, A. A.Zozulya, J. Opt. Soc. Am. B. 8, 12(1991).

[12] O. V. Lyubomudrov, V. V. Shkunov, Kvantovaya Elektron. 19, 1102 (1992). S.Sternklar, Opt. Lett., 20, 3 249 (1995).

[13] D. Shaw, Opt. Comm 94, 458 (1992).

[14] A. A. Zozulya, M. Saffman, D. Z. Anderson, Phys. Rev. Lett. 73, 6, 818 (1994).

[15] W. Krolikowski, M. Cronin-Golomb, Opt. Comm. 89, (1992). M. Segev, D.Engin, A. Yariv, G. C. Valley, Opt. Lett. 18, 1828 (1993). A. A. Zozulya, M. Saffman,D. Z. Anderson, J. Opt. Soc. Am B 12, 2, 255 (1995). M. R. Belic, J. Leonardy, D.Timotijevic, F. Kaiser, J. Opt. Soc. Am. B. 12, 9 (1995).

[16] D. Engin, M. Segev, S. Orlov, A. Yariv, G. C. Valley, J. Opt. Soc. Am. B. 11, 9,1708(1994).

[17] Y. Fainman, E. Klancnik, Sing H. Lee, Opt. Eng, 25, 2 (1986).

[18] S. Sternklar, S. Weiss, M. Segev, B. Fisher, App. Opt., 25, 24 (1986).

[19] S. Orlov, M. Segev, A. Yariv and G. C. Valley, Opt. Lett. **19**, 578 (1994).

Chapter five

Experimental investigation of conjugation fidelity and critical slowing down in double phase conjugation

5.1 Introduction

In this chapter we summarize the experimental studies carried out in parallel with the modeling efforts described in chapter 4 for the double phase conjugate mirror. The results of these studies are also presented in references[1,2]. The first study concentrates on determining conjugation fidelity experimentally. Here, various dependencies of conjugation fidelity on system parameters are studied, i.e. gain and pump intensity ratios. The second study was designed to study the characteristic temporal behavior predicted by the coupled mode theories, namely the critical slowing down. This study also points out various theoretical and experimental similarities between Double phase conjugate mirror and various other critical phenomena [2].

5.2 Experimental setup

The experimental setup for the four-wave mixing experiment is shown in figure 5.1a. The pump beams originating from a multimode 488-nm Ar-ion laser are expanded and collimated before being divided into two arms by the beam splitter 50/50 (BS). The

multimode Ar-ion laser has a 3 cm coherence length and it is polarized in the plane of the optical system (extraordinary polarization). Intensity ratio between the two pump beams is controlled by the variable absorber (VA) on one of the optical arms. Passing through a US Air Force resolution chart (T), image bearing collimated beams go through a single lens imaging system. In order to simulate the linearized material response in the experiment the $BaTiO_3$ crystal is placed between the image and the focal planes of the resolution chart. This way a spatially uniform intensity pattern is observed with in the crystal. Controlling the gain via a third erasure beam also helps to guarantee relatively small intensity modulations within the crystal. The third erasure is incoherent to both of the pump beams and has an ordinary polarization in order to minimize the fanning of the third beam. The angle between the two pump beams inside the crystal is approximately 8 degrees (this is also the angle where the peak of a fanning distribution arises in the absence of the second beam).

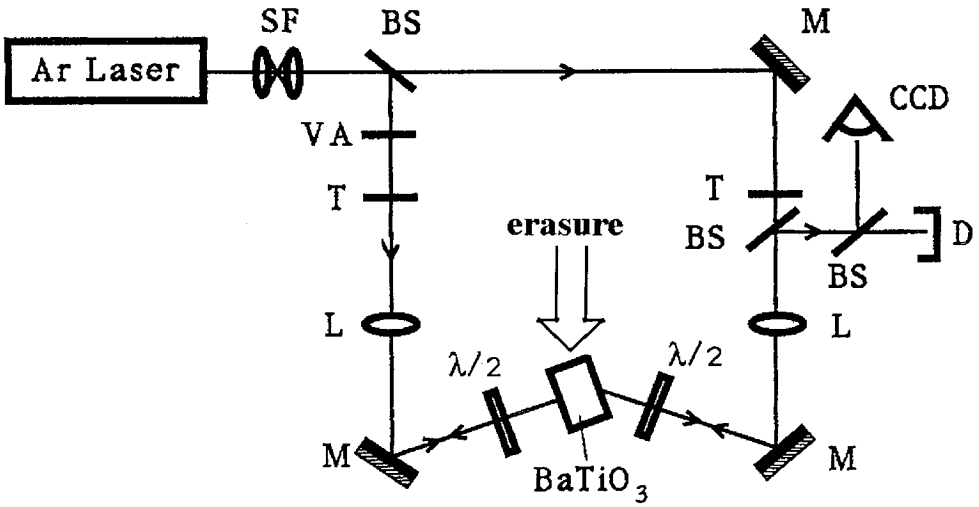

Figure 5.1a. experimental setup for the DPCM studies.

Care is taken to maximize the overlap of the two pump beams. The diameter of the beams in the crystal are roughly a millimeter and the interaction region is in the shape of a rectangle with dimensions 1cm by 1 mm. The half wave plates on both arms are also used to control the gain of the interaction (other than uniform erasure beam). This technique is especially useful for temporal measurements where varying the average intensity is not desirable. The phase conjugate output on one of the arms is collected by a second beam splitter which then is magnified and captured by a CCD camera. Reflectivity of the output is measured by a reversed biased photodiode detector. When the quality of phase conjugation is measured [1], a scanning variable slit across the magnified image plane is used and the transmitted power in various locations is measured. In this the visibility of various bars in the resolution chart are measured and the visibility is used to quantify conjugation fidelity.

Two important issues in getting good phase conjugate outputs is concerned with minimizing competing processes such as phase conjugation via backscattering [4] and conical beam formation [5,6]. Phase conjugation via backscattering is stimulated by backward traveling coherent seeding which may be supplied by reflections from volume imperfections or the crystal edges. Beams are situated away from the corners and the crystal is submerged in an index matching fluid in order to minimize reflections. Presence of the backscattering process is checked by blocking one of the pump beams and looking for the phase conjugate output for the other beam. The conical beam formation is typically observed when the angle between the pump beams is very small and/or when the information carrier by the pump beams is very simple (Gaussian or plane waves). The process essentially arises from the degeneracy of the grating sharing process in the third spatial dimension. The far field pattern of the resulting conical ring output (on each side) consists of a circle. The circle intersects the plane of incidence on two points, one being the phase conjugate direction and the other being the transmitted pump beam. It is found in

ref[1] that the degeneracy which is responsible for the conical ring can be reduced by rotating the images on the resolution charts by 45 degrees, this way the bars are neither parallel nor perpendicular to the plane of incidence. Very little is understood about the exact nature of the symmetry and degeneracy for image bearing beams. For the purposes of comparing our results with the two-dimensional simulations described in chapter 4, we minimized the conical ring formation. Figure 5.1b shows the angular spectrum of the waves traveling to the right in figure 5.1a. The angular spectrum is shown both above and below the threshold.

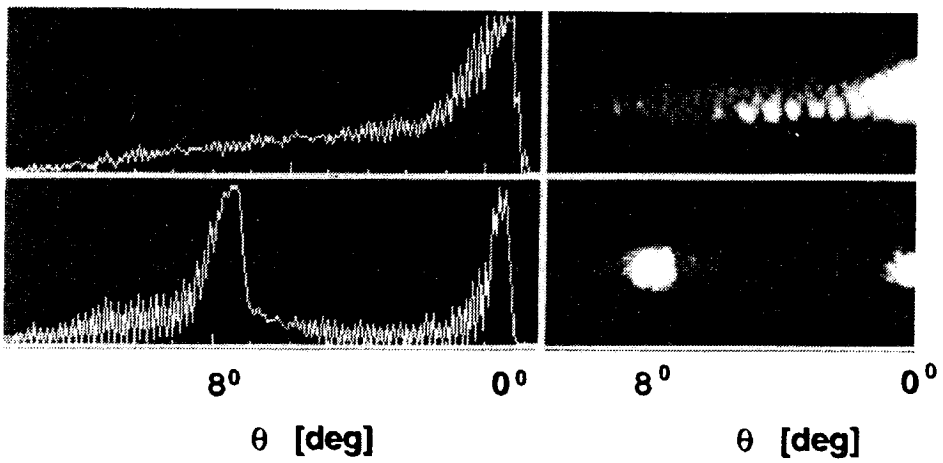

Figure 5.1b. The angular spectrum (the far field, photographs, right; averaged intensity profiles, left) of one of the output beams below (upper section) and above (lower section) the transition point (gain threshold). The intensity of the small features in the upper right photograph is much smaller than the single (phase conjugate) peak in the lower right photograph.

The figure shows that below the threshold the fanning process in the presence of the second beam is taking place, the wide angular distribution can be compared with the

angular distributions acquired in chapter 3 (figure 3.3). Angular distribution below the threshold typically exhibits structured patterns as well, (upper right picture). Above the threshold the wide angular spectrum collapses into the phase conjugate output. This is exactly the type of behavior captured by the generalized coupled mode simulation, chapter 4.

5.3 Measurement of the conjugation fidelity and its comparison to reflectivity

In this section we describe the measurement technique used to quantify the quality of phase conjugation [1, 7] and measure its gain dependence. The result is compared to the measured conjugation reflectivity dependence on gain. Figure 5.2 shows a phase conjugate output where the conjugation quality is quite high.

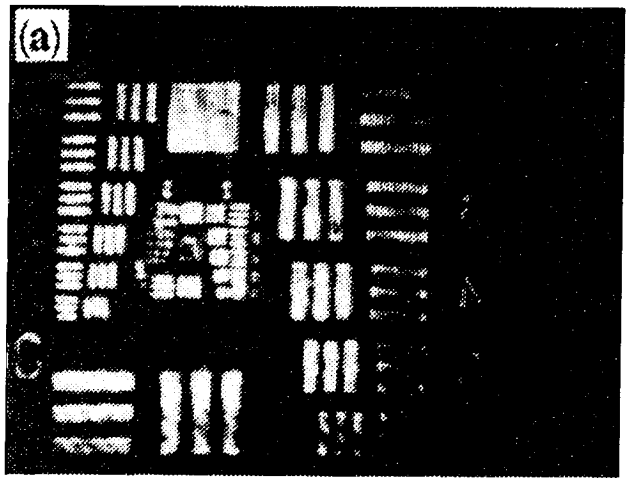

(a)

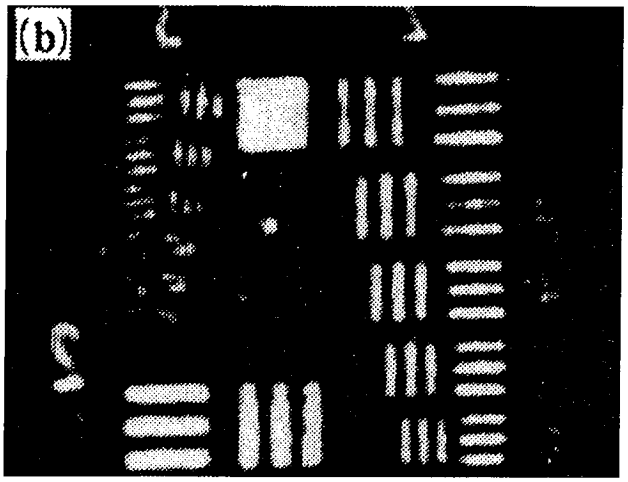

(b)

Figure 5.2a,b phase conjugate outputs from ref[1, 7], with good conjugation quality. b) magnified central portion of the chart.

The best resolution in the phase conjugate image is 40 micrometers, limited only by the apertures of our optical components, and the maximum observed phase-conjugate reflectivity is 35 %. Conjugation quality is quantified in the following way: A specific group of elements in the resolution chart is chosen, element #1, group #2, which consists of three bars at the density of 4.00 line pairs/mm in the original image plane. Using the scanning variable slit, the optical intensities are measured in a sequence of bars that are bright-dark-bright in the original image, denoted by υ_1, υ_2, and υ_3. The conjugation fidelity is quantified with these three measurements of the intensity using the following function:

$$F = \frac{0.5\,(\upsilon_1+\upsilon_3) - \upsilon_2}{\max(\upsilon_1,\upsilon_3) + \upsilon_2}, \qquad 5.1$$

where υ_1, υ_2, and υ_3 are the optical intensities measured in a sequence of bars that are bright–dark–bright in the original image. It should be noted that mathematically the fidelity defined in equation 5.1 is not equivalent to the definition in equation 4.9. However we expect similar type of functional (gain dependence) characteristics for a simple bar structure.

The normalized conjugation reflectivity is defined as the intensity integrated over the entire region of the image, $\upsilon_1 + \upsilon_2 + \upsilon_3$, divided by its maximal obtainable value. We measure the fidelity and the reflectivity as function of the power of the erasure beam I_e. [4]

$$\gamma(I_e) = \frac{\gamma_0}{1 + (I_e / I_0)}, \qquad 5.2$$

where $I_0 = I_1 + I_2$, I_1 and I_2 are the intensities of the interacting beams and γ_0 is the coupling constant for $I_e = 0$. The PR gain is defined as coupling coefficient γ times the

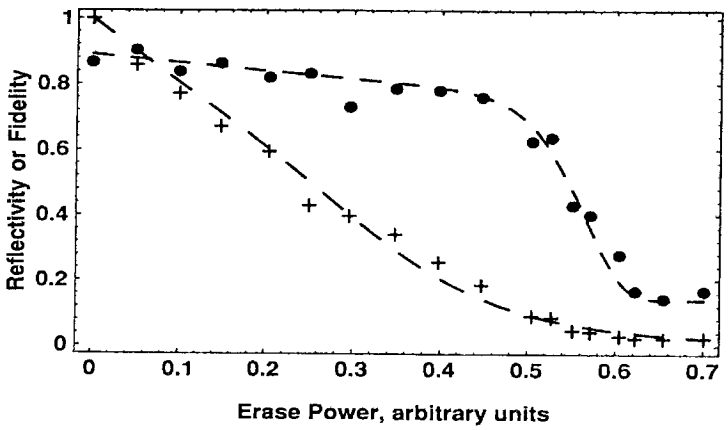

Figure 5.3. Phase-conjugation fidelity (circles) and reflectivity (crosses) as a function the power of the erasure beam, from ref[1]. Note the fidelity threshold at erase power of 0.55 a.u. The curves are only a guide to the eye.

interaction length L (in our experiment L = 7 mm). The results shown in Figure 5.3 reveal a sharp fidelity threshold at $I_e = 0.55$ (in arbitrary units). From the optical power of the input beams and the beams' cross sections, we estimate the average I_0 to be roughly 0.32 ± 0.05 (in arbitrary units). The relative sharp behavior of fidelity compared with the reflectivity is apparent , this result is in agreement with the 2-D numerical simulations described in the previous chapter [8,9]. The fidelity achieves a large value for gain values right above the threshold, hence the phase conjugate mode is apparent early on before the pump waves are depleted.

It is also an interesting observation that the threshold for different image resolutions appear to be different. Figure 5.4 shows phase conjugate images for various gain values.

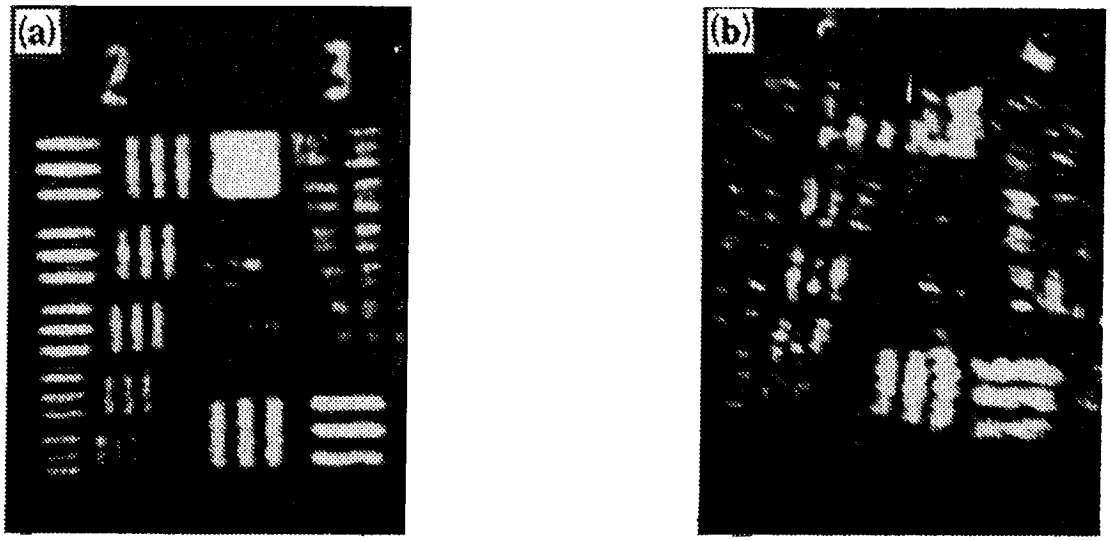

(a)

(b)

(c)

Figure 5.5. Phase-conjugate images at (a) maximal, (b) high, and (c) low gain for an input image that contains elements of both resolutions. Note that most of (c) is below threshold.

In figure 5.5 for a given gain value the bars with lower spatial resolution are conjugated better (i.e. higher conjugation fidelity). Bottom right-hand side of the whole image is better conjugated than the remaining part of the image. Distortions experienced by the vertical bars result in apparent bending of the bars. Such large-scale distortion may be due to the convective nature of the instability first pointed out in reference [10] and measured in reference [11]. These observations show the complexity of the actual problem and the number of possible distortion mechanisms that results in lower conjugation fidelity. In

reference[1] the image resolution dependence of the conjugation fidelity is studied in depth and quantified with the technique described earlier in this section.

5.4 Effects due to intensity ratio of the pump beams and asymmetric phase conjugation, experiments

When the intensity of the pump beams are equal typically the quality of phase conjugation is similar on the two sides. However as the process is made asymmetric, for example, by making intensities of the two pumps different, the conjugation fidelity on the side of weak input beam worsens considerably [1]. This constitutes one of the important limitations of this device from a practical point of view [12]. Figure 5.6. shows the two phase conjugate outputs for the same gain value.

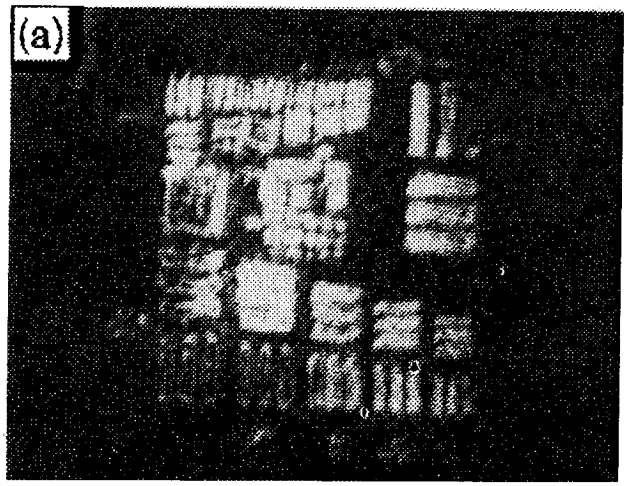

(a)

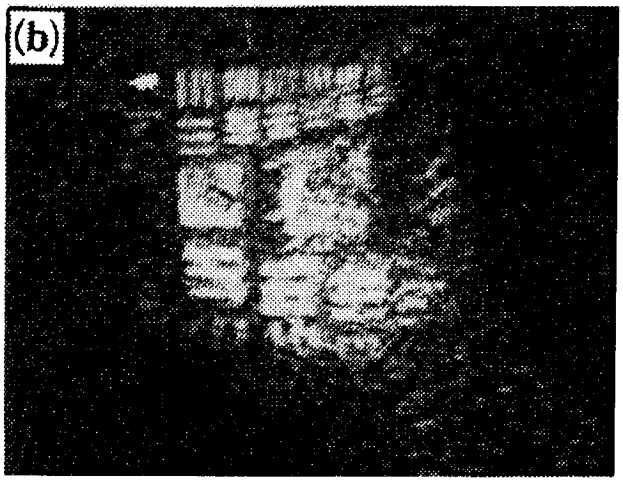

(b)

Figure 5.6. Phase-conjugate images for unbalanced input beams of intensity ratio 1:5: (a) the beam that leaves the face on which the beam of intensity 5 enters (i.e., the phase conjugate replica of the strong beam). (b) the beam that leaves the face on which the beam of intensity 1 enters (i.e., the phase conjugate replica of the weak beam).

The coexistence of fanning and phase conjugation is apparent in figure 5.6 b. The strong beam partially diffracts from the shared gratings (phase conjugation) and partially fans. It is interesting to note that in figure 5.6 b the conjugation is best realized in the upper right corner. The opposite corner seems to suffer the most from the fanning process. Again it is clear that a complicated spatial distortion on the phase conjugate beam results from the asymmetric phase conjugation.

5.5 The dynamics of double phase conjugation

In this section we describe the study of the phase conjugation dynamics described in detail in reference [2]. Primarily the dynamics of the reflectivity is studied. The reflectivity measured by the photodiode is recorded via a computerized data acquisition

system. The typical dynamics observed was on the order of few seconds to few hundred seconds. Since the increased average intensity quickens the response of the material an alternative scheme is used to control the gain. In $BaTiO_3$ the photorefractive coupling is large for the extraordinarily polarized light and almost negligible for the ordinary polarization, and one can control the coupling coefficient by varying the polarization of the interacting beams. In this way the extraordinary polarization provides the highest gain, and ordinary polarization gives the smallest gain. The coefficient γ may be expressed [1, 2] as a function of the polarization angle ϕ of the input beams

$$\gamma(\phi) = \frac{\gamma_0}{1 + I_{ord} / I_{ext}} \approx \frac{\gamma_0}{1 + \tan^2\phi},$$

5.3

where $\phi = 0$ corresponds to the maximal gain (extraordinary polarization), and I_{ext} and I_{ord} are the sums of the intensities of the extraordinarily and ordinarily polarized beams, respectively. Note that the above equation assumes that the intensity ratio of the ordinary to extraordinary component do not vary significantly spatially. For example in the cases where strong fanning is observed, large noniformities in this ratio should be expected, since only the extraordinary polarization component fans.

A typical dynamics of the phase conjugation is as follows: early on in the dynamics the features of resolution chart become recognizable. As the dynamics proceeds primarily the overall intensity of the output changes while the quality of phase conjugation remains the same. In the beginning part of the dynamics, parts of the image become recognizable earlier (i.e. the right bottom corner in figure 5.5). The features with lower resolutions tend to appear earlier than those with higher resolution. We first concentrated on one of the features on the resolution chart. The feature is isolated and focused into the photodetector. A typical dynamics is very similar in the functional form to the one predicted by the

numerical simulations, (figure 4.5). A response time is defined as the time it would take the reflectivity to achieve 1/e value of its steady-state value. Figure 5.7 shows the gain dependence of the reflectivity response time; the reflectivity is shown in the same figure.

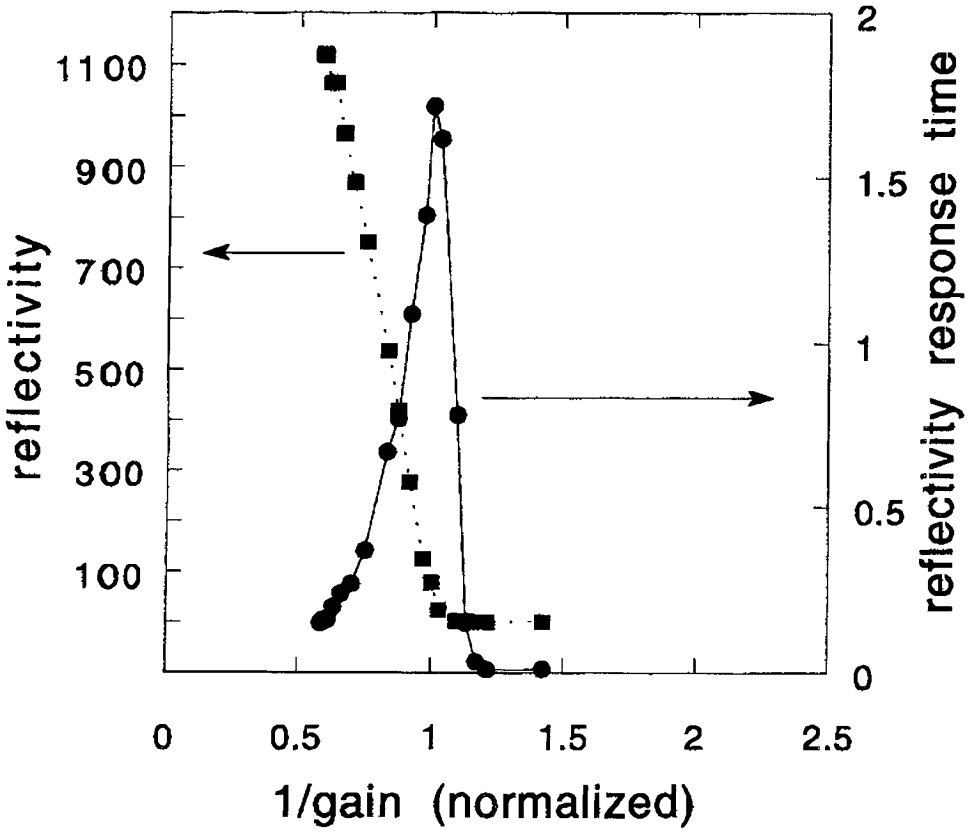

Figure 5.7. Experimental results of the phase-conjugate reflectivity and response time as a function of inverse gain for a single resolution element (1.26 line pairs/mm) of the image. The curves are only a guide to the eye.

The reflectivity response time achieves its maximum value right at the threshold as predicted by the numerical simulations, figure 4.5. Below this value no recognizable phase conjugate output can be seen, although fanning is apparent. Below the threshold gain value the response time of the fanning process becomes large very quickly as the gain is increased. This is one of the first observations of critical behavior in phase conjugate optics [13].

When the reflectivity time response due to the entire resolution chart is measured a broader functional dependence is observed (vs. gain). We believe that this is primarily due to variations in the threshold exhibited by different resolutions on the chart. However the physics of the resolution dependence of the steady-state results and the dynamics is not understood.

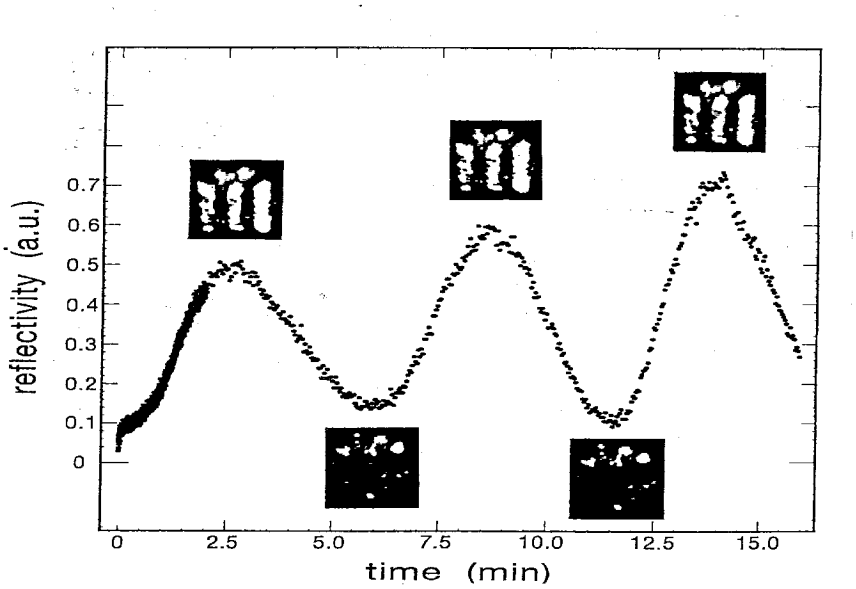

Figure 5.8 periodic dynamics exhibited by the reflectivity and phase conjugate outputs at correlation with the external parameters was found.

A more complicated dynamic than what was predicted by simulations, (figure 4.5). is also observed. This dynamical behavior in figure 5.8 becomes observable especially near the threshold. The reflectivity in figure 5.8 exhibits a periodic behavior. The phase conjugate outputs show that at the minima the conjugation quality is very low whereas at the maxima the quality is good. The behavior is believed to be intrinsic to the process and no observable correlation with the exterman parameters was found.

5.6 Summary

The quality of phase conjugation and the dynamics of phase conjugation is studied in detail. Conjugation fidelity, as predicted by the generalized coupled mode analysis (chapter. 4), achieves a high value even very close to the threshold. Various effects not predicted by the numerical simulations are observed as well. Different resolutions exhibit different thresholds and complicated spatial distortions coexist with the phase conjugate output. The temporal behavior of the reflectivity exhibits a strong gain dependence as predicted by the simulations, and the dynamics slow down considerably near the threshold (critical slowing down). Near the threshold oscillatory dynamics is observed as well, the origin of which is believed to be intrinsic to the interaction

References for Chapter Five

[1] S. S. Orlov, M. Segev, A. Yariv, and G. C. Valley, Opt. Lett. **19**, 578 (1994).

[2] D. Engin, S. S. Orlov, M. Segev, G. C. Valley, and A. Yariv, Phys. Rev. Lett. **74**, 1743 (1995).

[3] H. Haken, Synergetics (Springer-Verlag, New York, 1978), Chap. 8.

[4] G. C. Valley, J. Opt. Soc. Am. B **9**, 1440 (1992). (and references there in)

[5] A. P. Mazur, A. D. Novikov, S. G. Odulov, M. S. Soskin, M. V. Vasnetov, J. Opt. Soc. Am. B, **10**, 1408 (1993).

[6] Q. B. He, P. Yeh, C. Gu, R. R. Neurgaonkar, J. Opt. Soc. Am. B, Vol. **9**, 114 (1992).

[7] S. Orlov, *Holographic Storage Dynamics, Phase Conjugation, and Nonlinear Optics in Photorefractive Material*, Ph.D. thesis, Caltech, 1996.

[8] M. Segev, D. Engin, A. Yariv, and G. C. Valley, Opt. Lett. **18**, 956 (1993).

[9] D. Engin, M. Segev, S. S. Orlov, A. Yariv, and G. C. Valley, J. Opt. Soc. Am. B **11**, 1710 (1994).

[10] A. A. Zozulya, Opt. Lett. **16**, 545 (1991).

[11] N. V. Bogodaev, V. V. Eliseev, L. I. Ivleva, A. S. Korshunov, S. S. Orlov, N. M. Polozkov, and A. A. Zozulya, J. Opt. Soc. Am. B **9**, 1493 (1992).

[12] A. Chiou, P. Yeh, C. Yang, and C. Gu, Opt. Lett. **20**, 1125 (1995).

[13] M. Goulkov, S. Odoulov, R. Trott, Ukrainian Phys. J. **36**, 7, 1007(1991).

Chapter six

Treating double phase conjugation as a pattern forming system outside of equilibrium and amplitude equation formalism

6.1 Introduction

Large number of physical systems exhibit spatio-temporal pattern formation when the system is driven away from equilibrium,- a phenomenon that goes under names of dissipative structures, synergetics, and self-organization [3]. Examples include patterns in hydrodynamic systems such as thermal convection in pure fluids and binary mixtures, Taylor-Couette flow, parametric-wave instabilities, as well as patterns in solidification fronts, oscillatory chemical reactions and excitable biological media and nonlinear optics. The pattern formation in all these very different physical systems have large number of similarities and they can be approached from a unified point of view. The basic phenomena is as follows: a system originally under equilibrium external conditions is put under

nonequilibrium external conditions, for instance in DPCM the turning on of the mutually incoherent pump beams incident on to the photorefractive crystal. Typically in these systems one or more control parameters determine the degree to which the system is out of equilibrium. The coupling constant in DPCM, or the effective electro-optic coefficient represents the control parameter. As the control parameter is increased originally stable modes (corresponding to various wave numbers and frequencies) become unstable above a threshold. For a given control parameter a family of modes become unstable and their amplitudes grow in time. As the amplitudes of the modes become large enough the system becomes nonlinear and the unstable modes begin to compete with each other. The competition results in further selection of the modes that survive at long times. In general the nonlinear system has multiple solutions and the solution that wins at long times depends strongly on the dynamics (mode competition).

In DPCM [1-9] we found that phase conjugate mode appears early on in the dynamics (chapter 4), pointing out the fact that phase conjugate mode is one of the most unstable linear modes. However for a fixed gain value, various nearby modes are expected to become unstable as well and at long times the surviving output of the system will be determined by the nonlinear interaction between these modes. The linear modes near the phase conjugate mode can be found through the linear stability analysis. The linear stability analysis carried out for the plane wave pump beams is presented in section 6.3. The analysis derives a dispersion relationship, linear stability spectrum, which governs the spatio-temporal behavior of a wave packet (superposition of linear modes) in the linear regime. The convective behavior mentioned in previous chapters manifests itself as a group velocity term in the linear stability spectrum for DPCM. In section 6.3 the origin of the large-scale distortions due to the convective behavior is described in detail.

The amplitude equation formalism carries the linear theory (linear stability spectrum) to the weakly nonlinear regime. It is a theoretical approach that has successfully quantified number of important experimental observations in pattern forming systems. The

equation captures the spatio temporal behavior of these systems near the threshold and has a universal form. The amplitude equation is introduced in section 6.4 for DPCM and its form is motivated by physical arguments. (Detailed derivation is presented in section 6.6.) In section 6.5 the spatio-temporal dynamics predicted by the amplitude equation is illustrated. In this weakly nonlinear regime, fronts [18] are the building blocks of the nonlinear dynamics and through the linear front selection analysis the front solution that survive at long times can be determined. In the nonlinear regime also a possibility of another transition (threshold) arises. At this transition point the system loses its convective behavior, and becomes an oscillator (absolute instability). The possibility of such a transition is also investigated in section 6.5.

6.2 Starting equations:

The propagation of nearly counterpropagating, monochromatic optical waves in photorefractive materials is governed by the following equations:

$$i\,e - i\,\alpha^2\,\partial_x^2 e + \alpha\,\partial_x i = -\,(1+\alpha\partial_x e)^2\partial_t e - e\,i\,\alpha\,\partial_x e - \alpha\partial_x i\,\partial_x e$$

$$\exp(j\,(k\,L - \beta)z)\;\left(\partial_z A - j\;\beta\,A - j\;\beta\,\partial_x^2 A + j\;2\;\gamma_0 e\,A\right) + c.c. = 0 \qquad \text{6.1a-c}$$

$$\exp(-j\,(k\,L - \beta)z)\;\left(\partial_z B + j\;\beta\,B + j\;\beta\,\partial_x^2 B - j\;2\;\gamma_0 e\,B\right) + c.c. = 0.$$

Here, z, x, t are normalized by the length of the interaction region L, the inverse of the transverse component q_0 of the wave number for the pump beams, and the dielectric relaxation time τ_a, respectively. The space charge field, $e = E_{sc} q\,/(k_B T k_D)$ is normalized by the amplitude of the maximum field possible, which occurs when the grating wave number

is equal to the Debye wave number, k_D [9]. The intensity profile (with slow temporal variation) due to the counter propagating incoherent beams, i, is normalized by the conserved total incident intensity, and the beam amplitudes are normalized by the incident pump beam amplitude. (Note that in this article j refers to $\sqrt{-1}$.) Only the degenerate case with equal pump intensities is considered. Another important point is that A, B are complex amplitudes while e, i are real amplitudes.

Eq(6.1a) can be derived from Kukhtarev's equations[7,10] for $N_A << N_D$ and for fast electronic recombination. Here only the non-local response of the material due to charge transport is considered. A brief description of the derivation of eq(6.1a) is presented at section 2.3. Eqs (6.1b,c) are the paraxial wave equations for the counter propagating beams. The magnitudes of the parameters $\alpha = q_0/k_D$ and $\beta = (q_0/2k)\, q_0\, L$ reflect the relative importance of the transverse spatial derivatives in eqs(1a-c), due to the grating wave number dependence of the photorefractive effect and due to wave propagation respectively. For typical experimental conditions for phase conjugation β is orders of magnitude larger than α ($\beta \approx 2\ 10^4, \alpha \leq 1$). When $2\, q_0$ is considered to be a grating wave number (see sec(6.3)) then the β parameter can be shown to be proportional to the Q-parameter [11] of the particular volume hologram. Thus a large β value signifies a thick hologram. In eqs(6.1b,c) we define the control parameter $\gamma_0 = (L\, k/2\, n_b)\ r\ (k_D\, k_B\, T/q)$ [7], where r is the effective electro-optic coefficient. In this article the slow dependence of r on the grating wave number is neglected.

6.3 Linear Stability Analysis:

The linear stability analysis is a straightforward generalization of the linearized 1-D theory. It captures the convective nature of the instability in a simple way and renders the source of this behavior easier to trace. There have been earlier studies of the same problem [4, 11], However those studies start with a simpler material equation and ignore the effects of the

grating wave number dependence of the photorefractive effect. Our results agree with them in the simplified limits.

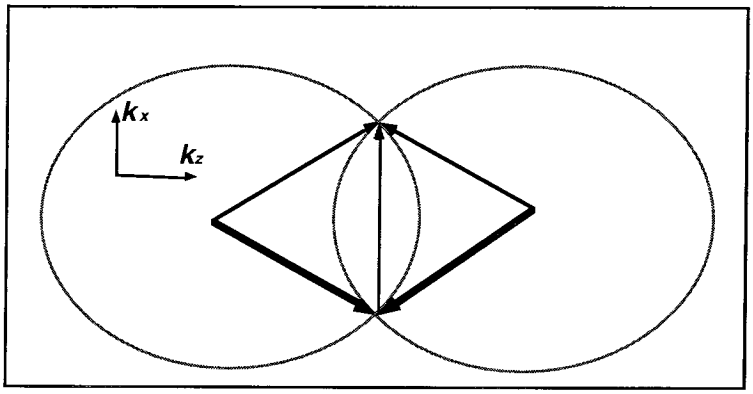

Figure 6.1 k-space picture of the four-wave mixing process, the single transmission grating is shared by the counterpropagating waves.

In our analysis the pump waves are taken to be nearly counter propagating plane waves, fig(6.1) and we consider a system with infinite transverse size. The linearized 1-D [1] theory takes into account only the efficiently shared, phase matched grating which we will refer to as the phase conjugate mode. The theory finds that the grating becomes unstable (an exponential growth in time) above a threshold value for the coupling constant, i.e. the growth rate of the grating goes from a negative value to a positive value crossing the threshold (critical slowing down [2]). It also finds that the phase velocity of this most unstable grating is zero and the spatial growth of the phase conjugate waves from the boundaries is linear instead of exponential in z. From these results the theory concludes that the system is an oscillator (also known as an absolute instability). The transverse dimension can be added to this theory by simply considering a slow transverse modulation to the most unstable grating. The analysis includes other possible gratings that have slightly larger or smaller wave numbers. These modes can become unstable through an imperfect grating sharing mechanism: for these modes the gratings written by the counter

propagating waves have slightly different wave vectors and hence the diffraction of the pumps from each other's gratings are phase mismatched, fig(6.2).

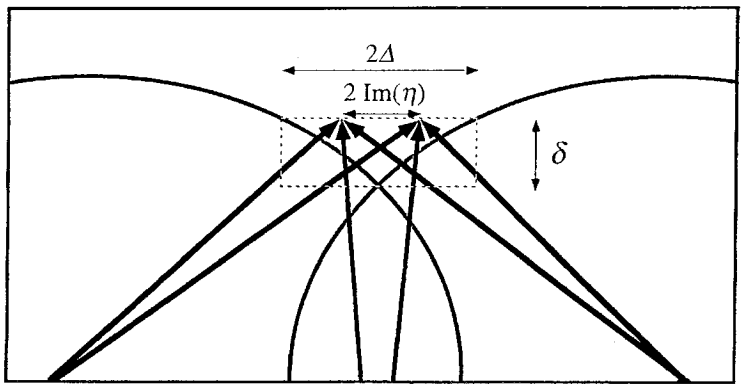

Figure 6.2 the imperfect grating sharing process.

For a system with finite interaction length the phase mismatch is allowed and for a slightly larger coupling constant these nearby modes become unstable.

A classification of the instability based on the existence of a threshold (change of sign for the growth rate) or z dependence of the phase conjugate wave amplitudes can be misleading. A correct classification of the instability requires the study of the entire spectrum of unstable modes. In order to illustrate the differences between an absolute instability and a convective instability, it is instructive to consider a noise source with broad spatial spectrum.

The source is spatially localized in the infinite transverse system and it is turned on and off in a short time, fig(6.3a, b). From this noise only the grating modes that are unstable will start growing in time. Thus, a wave packet will develop with spatial spectrum that correspond to the set of unstable modes. The characteristics of the motion of this wave packet is governed by the linear stability spectrum which gives the relevant dispersion relationship. If the wave packet is stationary in space, then the grating amplitude locally grows exponentially in time and the system is called an oscillator (absolute instability),

fig(6.3a). However if the wave packet not only grows exponentially in time but also moves in some direction then locally the grating amplitude decays and the system is called an amplifier (convective instability), fig(6.3b).

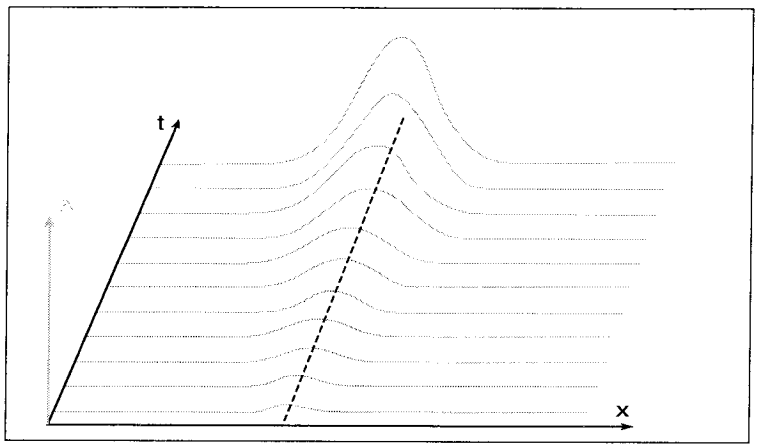

Figure 6.3a spatial dynamics in absolute instability

In terms of these definitions, a nonzero group velocity term in the linear stability spectrum at threshold translates into a convective system, since the finite propagation speed always overcomes the slow exponential growth near threshold. The above classification of the instability has important consequences when a finite transverse system is considered.

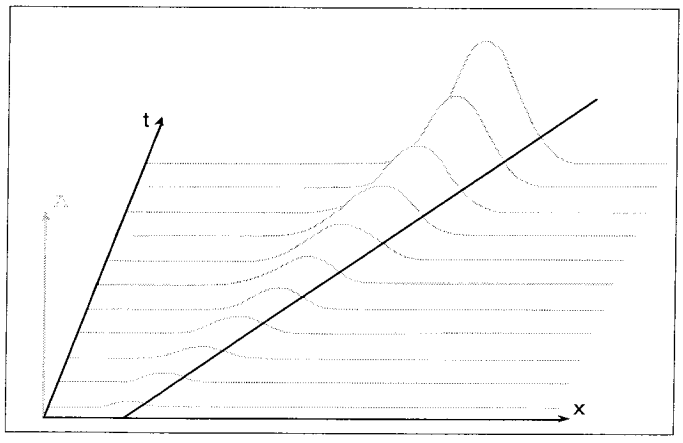

Figure 6.3b. spatial dynamics in convective instablity

In the convective case, the disturbance that grows most strongly is the amplified noise from one of the boundaries and the developed grating is sensitive to temporal fluctuations in the boundary noise. In an absolutely unstable system the transverse boundaries are not as critical in determining the characteristics of the growing grating amplitude. For the 4-wave mixing system the noise is thought to be due to scattering of the pump beams from stationary imperfections in the material and hence it is independent of time [15]. In this case the consequences of the above classification become more subtle. In what follows we describe the derivation of the linear stability spectrum. The linear instability spectrum is crucial to distinguish between the oscillator and amplifier case, and we now describe its derivation.

We consider a slow transverse modulation of the most unstable grating wave number q_c which is $q_c = 2$ in our notation:

$$e = \exp[j\ (2 + \delta)\ x] \exp(-j\ \Omega\ t)\ \bar{e}_\delta(z) + c.c. \qquad 6.2a$$

The waves consist of the undepleted pumps and the scattered plane waves from the modulated grating.

$$A\ = \exp(-j\ x) + \exp[j\ (1+\delta)\ x] \exp(-j\ \Omega\ t)\ \bar{a}_\delta(z) + c.c. \qquad 6.2b$$

$$B\ = \exp(-j\ x) + \exp[j\ (1+\delta)\ x] \exp(-j\ \Omega\ t)\ \bar{b}_\delta(z) + c.c. \qquad 6.2c$$

Here Ω is complex frequency and defines the linear stability spectrum. Looking for solutions of this form in eqs(6.1a-c) we arrive at the following linear system:

$$\begin{bmatrix} 1 & j\tilde{\gamma}/2 & j\tilde{\gamma}/2 \\ j\,2\gamma_0 & \partial_z+\Delta & 0 \\ -j\,2\gamma_0 & 0 & \partial_z-\Delta \end{bmatrix} \begin{bmatrix} \bar{e}_\delta \\ \bar{a}_\delta \\ \bar{b}_\delta \end{bmatrix} = 0 \qquad 6.3$$

with the boundary conditions $\bar{a}_\delta(0)=0$, $\bar{b}_\delta(1)=0$. Here the dephasing factor $\Delta = j\,\beta\,(\delta^2 + 2\,\delta)$ is the degree of phase mismatch between the shared grating and the scattered waves. In the 1-D theory the dephasing factor is zero since the shared grating is perfectly phase matched fig(6.1). We define $\tilde{\gamma} = \alpha\,(2+\delta)\,/\,[-j\,\Omega + 1 + (\alpha\,(2+\delta))^2]$, which captures the wave number dependence of the two-wave mixing gain, Γ [1]. In our notation Γ is given by $2\,\gamma_0\,\tilde{\gamma}$. Also note that $-j\,\tilde{\gamma}/2$ is the ratio between the space charge field amplitude and the spatially varying intensity pattern. The 1-D theory self-consistently shows that this ratio is purely imaginary ($\pi/2$ phase shifted grating) and hence the phase velocity of the grating is zero.

The system of ordinary differential equations is solved by assuming an exponential solution and finding the eigenvalues (exponents of the spatial growth) and eigenvectors of the resulting linear system. In this way the pair of complex eigenvalues η, $-\eta$ are given by $\eta^2 = \Gamma\Delta + \Delta^2$, and the most general solutions are of the form:

$$\bar{a}_\delta = \Gamma/2\,C_1\,\exp(\eta\,z) + \Gamma/2\,C_2\,\exp(-\eta\,z)$$

$$\bar{b}_\delta = (\eta - \Delta - \Gamma/2)\,C_1\,\exp(\eta\,z) - (\eta + \Delta + \Gamma/2)\,C_2\,\exp(-\eta\,z) \qquad 6.4a,c$$

$$\bar{e}_\delta = -j\,\tilde{\gamma}\,[(\eta - \Delta)\,C_1\,\exp(\eta\,z) - (\eta + \Delta)\,C_2\,\exp(-\eta\,z)]$$

The k-space picture for nonzero modulation δ is shown in fig(6.2). Notice that in fig(6.2) the scattered wave vectors are not on the index ellipsoid, this points out the nonzero phase

velocity for the particular mode . Hence the scattered waves have optical frequencies that are slightly different from the pump waves. The boundary conditions fix the phase between the two evanescent waves at positions $z=0$ and $z=1$ and this allows only a certain band of eigenvalues. In other words, Γ must be a function of Δ through the following transcendental equation:

$$- 2/\Gamma = \sinh(\eta)/\eta \qquad 6.5$$

eq(6.1a) can be written in the following manner;

$$-j\,\Omega = -1 - \alpha^2 (2+\delta)^2 - \gamma_0\, \alpha\, (2+\delta)\, (-2/\Gamma). \qquad 6.6$$

and with $\Gamma(\Delta)$ from eq(6.5), this gives a convenient expression for the spectrum. The modulation δ dependence coming from wave propagation via $\Gamma(\Delta)$ and from the photorefractive effect (the terms involving α) are separable.

Close to the threshold we expect only the modes very close to the phase conjugate mode to become unstable. It is then instructive to derive an expansion of the spectrum for slow modulation of the phase conjugate mode. The expansion of $1/\Gamma$ for small Δ can be evaluated by assuming an expansion in eq(6.5) and solving the resulting set of equations for the coefficients iteratively, to yield.

$$-2/\Gamma = 1 + \Delta/3 + 4/45\, \Delta^2 + 19/945\, \Delta^3 + 8/2025\, \Delta^4 + O(\Delta^5) \qquad 6.7$$

Using this expansion, the stability spectrum eq(6.6) takes the following form:

$$\mathrm{Re}(-j\,\Omega) = -\,(1 + \alpha^2\,4 + 2\,\alpha\,\gamma_0) - \delta\,(\alpha^2\,4 + \alpha\,\gamma_0) + \delta^2\,(32/45\,\alpha\,\gamma_0\,\beta^2 - \alpha^2) + O(\delta^3) \quad 6.8a$$

$$\mathrm{Im}(-j\Omega) = -\delta\,(4/3\,\alpha\,\gamma_0\,\beta) - \delta^2\,(4/3\,\alpha\,\gamma_0\,\beta) + O(\delta^3). \quad 6.8b$$

The real part of the stability spectrum corresponds to the exponential growth or decay rate of the amplitude of the unstable mode, while the part of the imaginary term proportional to δ is the group velocity term. The non-zero group velocity in the x direction classifies the instability as a convective one. For typical experimental parameters for phase conjugation, the angle between the two pump beams is a few degrees. For this regime typically β is a few orders of magnitudes larger than α and the stability spectrum can be conveniently expressed as:

$$\mathrm{Re}(-j\,\Omega) = -\,2\,\alpha\,(\gamma_0 - \gamma_{0c}) + 32/45\,\beta^2\,\delta^2\,\alpha\,\gamma_0 + O(\beta^3\,\delta^3), \quad 6.9$$

where $\gamma_{0c} = -\,(1+4\,\alpha^2)/(2\,\alpha)$ is the threshold value for the control parameter, corresponding to the two-wave mixing gain of -2.

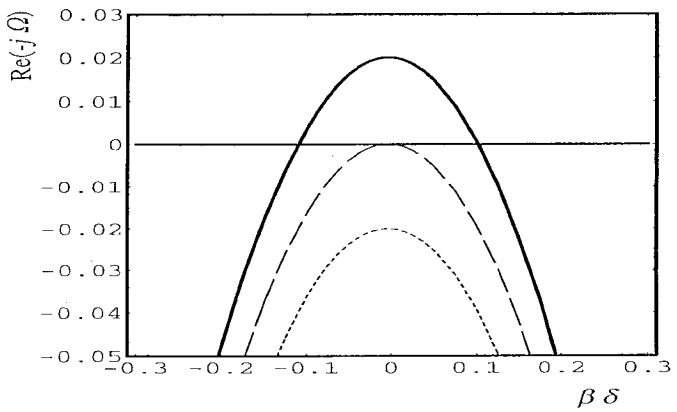

Figure 6.4 illustrates the growth rate for the modes centered around the phase conjugate mode becoming unstable as the threshold is crossed. The band has a maximum

at the phase conjugate mode, and the quadratic drop in the growth rate away from this mode is dominated by the phase mismatching effect.

Notice that for zero spatial modulation the real part of the spectrum changes sign as the control parameter is increased (becomes more negative) above the threshold value (as predicted by the 1-D theory).

Fig(6.4) illustrates the band of modes centered around the phase conjugate mode becoming unstable as the threshold is crossed. The band has a maximum at the phase conjugate mode, and the quadratic drop in the growth rate away from this mode is dominated by the phase mismatching effect.

Although the phase conjugate mode has zero phase velocity, eq(6.8), the group velocity is non-zero. Thus as illustrated in fig(6.3b): a grating wave packet consisting of these unstable spatial modes in an infinite transverse system would propagate towards the positive x direction. For dielectric relaxation time of 1sec and a grating period of 2 μm, the group velocity is about 0.1cm/sec. As mentioned before, a more realistic noise source in wave mixing experiments is time independent. In this case it is instructive to consider a semi-infinite system with spatially distributed, time independent noise fig(6.7b, small t). In this system, the noise at the lower boundary ($x = 0$) is amplified the most as the disturbance propagates to positive x, effectively outlining an exponentially growing envelope. So although the z dependence of the phase conjugate waves is linear, an exponential x dependence is expected in the linear regime. A finite transverse interaction region, that usually comes about due to the finite size of the pump beams, can be conveniently modeled in this simple picture with an absorbing transverse boundary to the $+x$ side of the first boundary. The noise generated disturbance grows and propagates through the interaction region, only to be eventually absorbed by the right boundary. For a typical group velocity of 0.1 cm/sec and transverse width (width of the pump beams) of 1mm, the disturbance crosses the interaction region in 1 sec. The exponential envelope is one of the first sought after predictions of the convective behavior (in the context of large-

scale distortions in the phaseconjugate beams) [13]. We must note that the absorbing nature of the second boundary is assumed here for simplicity. However this assumption does not change the main conclusions of this article.

For the large β regime, the wave number dependence of the photorefractive effect is only important for determining the threshold value of γ_0, eq(6.9), however notice that effectively the two-wave mixing gain threshold, $\Gamma = -2$, remains the same. A very important point in eq(6.9) is that the spectrum can be expressed as a function of $\delta\ \beta$ in this regime and the above expansion is good only for small $\delta\ \beta$. This point will become important for understanding the range of validity of the amplitude equation. Also notice that in fig(4) the growth rate is plotted as a function of $\delta\ \beta$; in this way the dependence of the results on β can be scaled out.

As the angle between the two pump beams become smaller the magnitude of β become closer to unity and the effects of the grating wave number dependence of the coupling constant becomes more important. Fig(6.5) illustrates the effects on the real part of the spectrum for different α values. The most unstable mode now deviates from the phase conjugate mode.

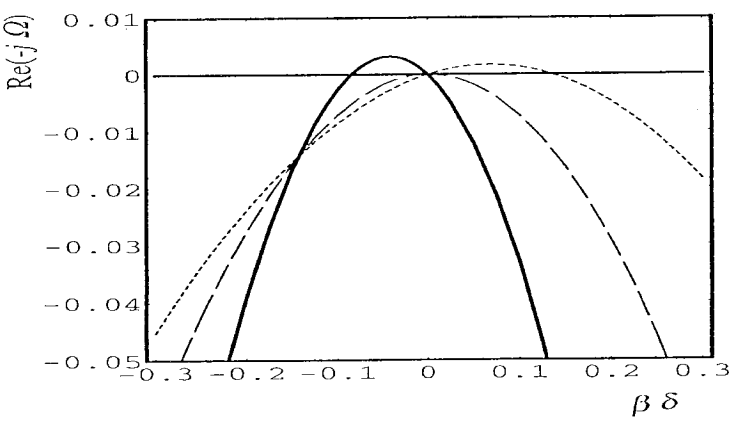

Figure 6.5 grating wave number dependence of the lin. stab. spectrum for three different $\alpha = q_0/k_D$ values

It is found that the most unstable mode is pulled towards the maximum of $\tilde{\gamma}$ which corresponds to the grating wave number equaling the Debye wave number. This shift also yields a less negative threshold than expected with γ_{0c}. A more dramatic deviation from the phase conjugate mode was observed with materials with mixed (local and nonlocal) response [14]. The leading order corrections to the threshold value and the most unstable mode can be calculated through a straightforward perturbation analysis. The results are the following:

$$\gamma_{1c} = \gamma_{0c} + (1 - 4\,\alpha^2)^2/(1 + 4\,\alpha^2)\ 45/128\ 1/\beta^2 + O(1/\beta^4) \qquad 6.10a\text{-}c$$

$$\delta_{1c} = (1 - 4\,\alpha^2)/(1 + 4\,\alpha^2)\ 45/64\ 1/\beta^2 + O(1/\beta^4).$$

Since the most unstable mode is not the phase conjugate mode in this regime a finite phase velocity for this grating can be calculated from eq(6.10b) and eq(6.8b).

$$v_{1c} = (1 - 4\,\alpha^2)/(1 + 4\,\alpha^2)\ 15/16\ \alpha/\beta + O(1/\beta^3).$$

For dielectric relaxation times of microseconds the phase velocity should be measurable through an interference experiment between the phase conjugate and the pump beams. It is important to note that for a complete quantitative study of the regime with very small angles between the two pump beams (pump beams almost counter propagating) two additional scattered plane wave amplitudes need to be considered [16]. It can be shown approaching this regime that the correction terms to the stability spectrum are proportional to Γ/β^2, and hence as β approaches unity the complete problem needs to be solved. However we

expect the basic qualitative picture of increasing deviation from the phase conjugate mode to remain.

6.4 **The Amplitude equation:**

In section(6.3) the linear stability spectrum that governs the linear spatio-temporal behavior of the system is derived and its implications are described. In this section we will introduce the amplitude equation, that extends the linear theory to the weakly nonlinear regime. Here, we attempt to motivate the form of the amplitude equation via physical arguments. A rigorous derivation of this equation from the starting equations eqs(6.1a-c) can be found in Appendix 6.A.

As shown in fig(6.4) near the instability threshold we find that only a small family of the modes around the phase conjugate mode becomes unstable and contributes to a growing instability as depicted in fig(6.3b). Hence near the threshold the first few terms of the small modulation $\delta\ \beta$ expansion of the dispersion relationship, eqs(6.8a,b) are expected to govern the spatio-temporal behavior of the growing instability. At the same time in this regime weak nonlinearities are expected to result in the saturation of the exponentially growing disturbance. The balance between these effects are described by the amplitude equation:

$$\tau_0\, \partial_t A + \tau_0\, s_0\, \partial_x A = \varepsilon A + 2\, s + \xi_0^2 (1+j\, c_1)\, \partial_x^2 A - g_0\, |A|^2 A. \qquad 6.11$$

The derivation (see Appendix 6.A) utilizes a multiple scale perturbative approach. In the analysis, the slow temporal and spatial variables are separated via an appropriate scaling by the smallness parameter, $\varepsilon = (\gamma_0 - \gamma_{0c})/\gamma_{0c}$. Physically the slow temporal and spatial variables can be directly inferred from fig(6.4). As the threshold is crossed, the growth rate of the unstable modes changes sign and it increases linearly with ε. This, critical

slowing down effect is described by the slow temporal variable. At the same time the quadratic spectrum of unstable modes, starting from a null width, widens as $\varepsilon^{1/2}$. The slow spatial variable governs the behavior of the instability amplitude that consists of this small family of unstable modes. The dependence of the wave and grating amplitudes in eqs(6.1a-c) on the amplitude $A(x,t)$ is given by the following relations:

$$\begin{pmatrix} \overline{A_p} \\ \overline{B_p} \end{pmatrix} = 1 - |A(x,t)|^2(1+4\alpha^2)^2/\alpha^2 \begin{pmatrix} z^2 \\ (1-z)^2 \end{pmatrix} + o(\varepsilon^{3/2})$$

$$\begin{pmatrix} a \\ b \end{pmatrix} = j\, A(x,t)(1+4\alpha^2)/\alpha \begin{pmatrix} z \\ (1-z) \end{pmatrix} \exp(j\,x) + o(\varepsilon^{3/2}) \qquad 6.12a\text{-}c$$

$$e = A(x,t)\exp(j\,2x) - j\,A(x,t)^2 \frac{(1+8\alpha^2)}{2\,\alpha\,(1+16\alpha^2)} \exp(j\,4x) + o(\varepsilon^{3/2})$$

where the counterpropagating waves in eqs(6.1b,c) are divided into the pump and the scattered waves as:

$$A = \overline{A_p}(z,t)\exp(-j\,x) + a(z,x,t)$$
$$B = \overline{B_p}(z,t)\exp(-j\,x) + b(z,x,t). \qquad 6.13a,\ b$$

The seeding, s, (see eq(6.11)) is introduced into the problem as boundary conditions on the scattered waves at their respective input planes. In eq(6.12a) the depletion of the pump waves is apparent. The depletion is proportional to the square of the amplitude $A(x,t)$ and it increases quadratically with z starting from the waves respective input plane. On the other hand the scattered waves are linearly proportional to the amplitude $A(x,t)$ and the waves increase in amplitude linearly with z as they traverse the interaction region. At this

order we find two grating amplitudes: one with the most unstable grating wave number and another with spatial frequency double the former. As described in the appendix A, the second harmonic term arises from the nonlinearities in the material equation eq(6.1a). Another interesting point is that the grating amplitudes eq(6.12c) are independent of z.

Next, we express the coefficients of the amplitude equation in terms of the system parameters. As expected the coefficients of the linear terms can be calculated from the linear stability spectrum.

$$\tau_0^{-1} = \gamma_{0c}\left[\partial_{\gamma_0}(-j\,\Omega)\right]_{0,\gamma_{0c}} = (1+4\,\alpha^2)$$

$$s_0 = \left[\partial_{\delta}\mathrm{Im}(-j\,\Omega)\right]_{0,\gamma_{0c}} = (2/3)\,\beta\,(1+4\,\alpha^2) \qquad 6.14a\text{-}d$$

$$\tau_0^{-1}\,\xi_0^2(1+j\,c_1) = -1/2\left[\partial_{\delta}^2(-j\,\Omega)\right]_{0,\gamma_{0c}} = \alpha^2 + 16/45\,\beta^2(1+4\,\alpha^2) + (1/3)\,j\beta\,(1+4\,\alpha^2).$$

Note that the linear constants are the first few terms in the small modulation expansion of eq(6.6). They include the quadratic drop in the growth rate away from the phase conjugate mode and the group velocity term.

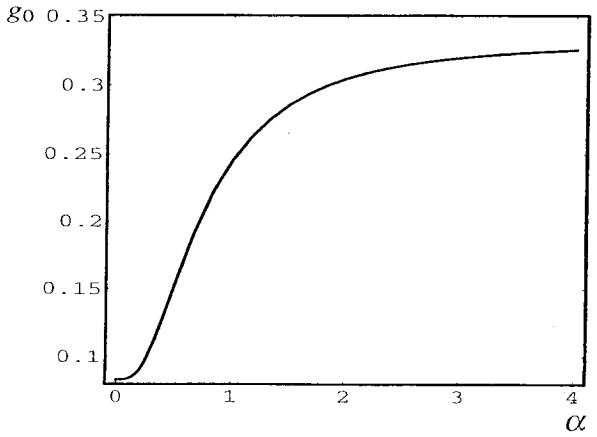

Figure 6.6 illustrates the strong dependence of the nonlinear coefficient on α.

The nonlinear coefficient is given by:

$$g_0 = 1/3 - (1+28\alpha^2+208\alpha^4+512\ \alpha^6)/[(1+16\alpha^2)\ 4(1+4\alpha^2)^3]$$

the factor of one third in this expression agrees with the results of the 1-D theory where the nonlinear saturation comes about due to the depletion of the pumps. The second term in this expression is due to the nonlinear terms in the material equation eq(6.1a). Fig(6.6) illustrates the strong dependence of the nonlinear coefficient on α. In an experiment this dependence can be observed by measuring the slope of the reflectivity (intensity) versus two-wave mixing gain curves for different angles between the pump beams, just above the threshold. According to the amplitude equation the slope should be inversely proportional to g_0.

An interesting advantage of the amplitude equation is the simplicity with which the finite transverse size of the interaction region can be treated (ref(3), sec(5.A)). For square pump waves the finite transverse size can be modeled as simple boundary conditions for the amplitude equation. Gaussian pump beams on the other hand can be modeled by a n amplitude equation whose linear coefficients are spatially varying. Both of these techniques assume that the introduction of the finite transverse size does not change the coefficients of the amplitude equation which were calculated for an infinite transverse system. Here we will give necessary conditions for the correctness of this assumption. The condition is related to the small modulation expansion of the linear stability spectrum. Clearly the first few terms of this expansion which are included in the amplitude equation are not sufficient if the transverse size is too small. This consideration results in the following condition: $L_x > L_z\ q_0/(2\ k)$. This condition also implies that the phase mismatch allowed due to the finite transverse size is much smaller than the one allowed by the finite

size in z direction (note that this is also the case for infinite transverse size). As described in section(6.3), the degree of phase mismatch allowed in the system determines the relative gain seen by the phase conjugate mode and the nearby modes (imperfect grating sharing) and if the above condition is not met the transverse phase mismatch is expected to contribute to the linear problem. In this article the most simple finite interaction region, that can be modeled as boundary conditions for the amplitude equation, is considered. Again for simplicity the two transverse boundaries are taken to be absorbing boundaries. These simple cases are considered here in order to make the major points of this article clear. The major conclusions of this article do not rely on this choice.

Lastly we would like to mention some of the obvious implications of the amplitude equation. Ignoring the spatial derivatives in eq(6.11), the prediction of critical slowing down can be easily inferred analytically. The seed term in this equation goes along with the analogy drawn in ref(2) between 1-D theory and the mean field theory for ferromagnetism. The convective behavior is clearly reflected through the group velocity term.

6.5 The weakly nonlinear regime:

The amplitude equation introduced in section(6.4) is of the form of a complex Ginzburg-Landau equation. The equation arises in many different dynamical systems and a large amount of work has been devoted to understanding its behavior. Utilizing this body of knowledge we will generalize the qualitative dynamical picture in fig(6.3) to the weakly nonlinear regime.

We first consider a system infinite in the transverse direction, with a spatially localized noise turned on for a short time. In this case a wave packet consisting of the unstable modes grows exponentially in time and at the same time propagates in the positive x direction with the group velocity eq(6.14b), as discussed before. Fig(6.7a) illustrates the extension of the dynamics of the disturbance into the nonlinear regime. The exponential

growth saturates due to the nonlinearity and the tails of the pulse steepen and eventually transform into particular shapes known as the selected front solutions, [3, 18].

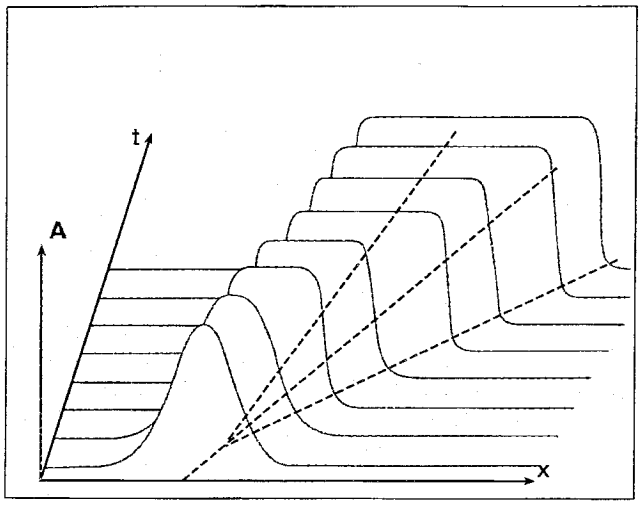

Figure 6.4a spatial dynamics in weaklly nonlinear regime, infinite transverse dimension, spatially localized noise is turned on for a short time

The fronts connect the uniform nonlinear state, which is a simple non-linear plane wave mode, to the zero amplitude solution. The velocities of the two fronts are different from the group velocity (dashed lines in fig(6.7a)). The left front moves at a velocity slower than the group velocity while the right front has a larger velocity. Effectively the width of the disturbance grows in time at a velocity equal to difference of the two front velocities. This widening of the disturbance can be thought of as the continuation of the growth process into the nonlinear regime. For larger ε (normalized coupling constant), the difference between the velocities is expected to increase. However in the convective regime both fronts move in the positive x direction, and eventually at any fixed x the disturbance is bound to decay away. Another interesting point concerns the uniform nonlinear state. The states laid down by the two fronts can be different, so that a transition region between the different uniform nonlinear states may also be expected at some interior point.

In a semi-infinite system with a spatially distributed, time independent noise source, only the right front develops, fig(6.7b). At the left end of the disturbance the exponential growth from the lower boundary saturates. However a simple front cannot form. This follows from the fact that the continuous noise source drowns out the zero amplitude solution which is necessary for the formation of the left front solution (moving in the negative x direction).

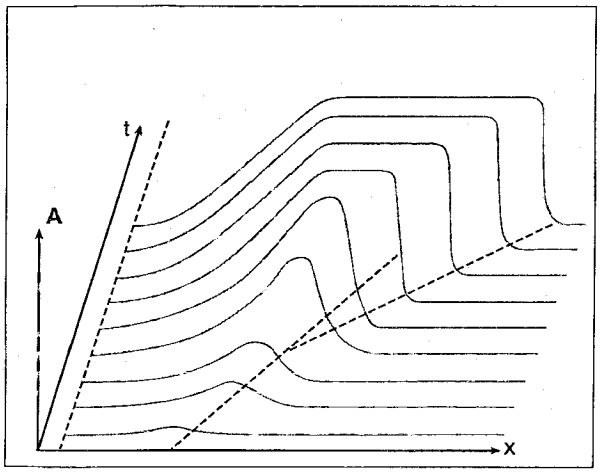

Figure 6.4b spatial dynamics in semi-infinite system with time independent noise source

The length over which the solution grows to saturation at the left end, $\ln(s^{-1})\varepsilon^{-1}\, s_0\, \tau_0$, can be quite large near threshold and for small noise strength, s. It should result in large-scale distortions in the phase conjugate beams and the detailed shape can be easily calculated by a numerical solution of the amplitude equation. For typical parameters, (τ_d=1sec, $\beta = 2\ 10^4$, $s = 10^{-4}$, $2\gamma_0\tilde{\gamma} = -3$) the length scale of the distortion is a few millimeters. Considering an upper absorbing boundary (finite interaction region) somewhat simplifies the behavior. Eventually the right moving front solution is absorbed by the boundary, so that the uniform nonlinear state laid down by the front solution should relax to the most unstable mode produced by the growth from the noise. In this more physical geometry with the two boundaries, the effects of the propagating front can only

show up in the transients of the system. Clearly with the absorbing boundary, if the noise is turned off the instability is eventually absorbed by the upper boundary and the disturbance cannot be sustained.

A dramatic change can happen for large enough control parameter if the left front velocity in fig(6.7a) changes direction. Such a transition [19] might be expected since the difference between the two front solutions normally increases with increasing ε (increasing growth). Fig(6.7c) illustrates the expected dynamics in the semi-infinite system where at time t^* the control parameter is increased above the transition value.

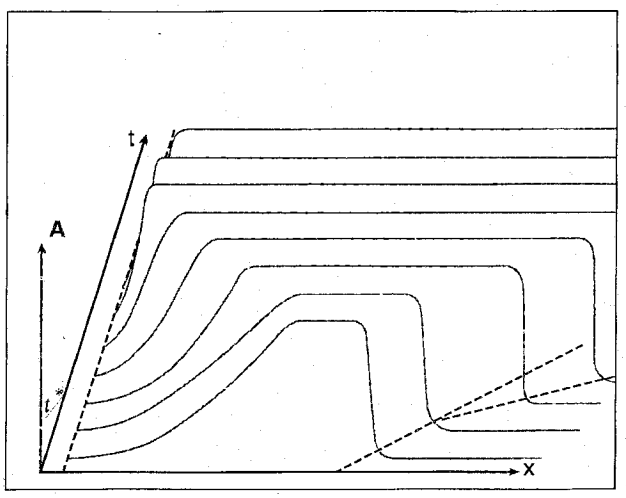

Figure 6.5. transition to absolute instability

After the control parameter is increased, a left front traveling to the negative x direction develops. In this regime the growth dominates the advection, and the relatively steep backward traveling front fills the region left behind by exponential growth from the left boundary. Now the healing length at the left boundary depends only the parameters of the amplitude equation (the characteristic length $\approx\xi_0$, eq (6.14d)) and not on the size of the noise. Furthermore in this regime the system is absolutely unstable (an oscillator) and the grating amplitude is sustained even in the absence of noise.

The above description of the dynamical picture heavily relies on the nonlinear front solutions with characteristic velocities and spatial decay rates. Since the amplitude equation is a nonlinear partial differential equation, multiple front solutions are expected to exist. The question of front selection in the complex Ginzburg-Landau equation [18, 20] has been addressed as a generalization of the rigorous analysis by Aronson and Weinberger for the nonlinear diffusion equation [21]. It is worth pointing out that the generalization, to date, is purely heuristic. There is no completely convincing derivation of the selection results to be presented below. Nevertheless, there are rather complete and precise predictions, and these can be tested by numerical calculations and by experiments.

A linear front selection analysis is the simplest approach to the front selection problem [21]. Although entailing a purely linear argument, it makes predictions for the nonlinear front solution selected at long times. A slightly more careful version is the "pinch point" analysis [22].

The analysis formulates the dynamics far in the tail of the front where it can be expressed in terms of a superposition integral. At long times the integral is dominated by the stationary phase point and it is required that in the frame of the selected front disturbance the amplitude neither grows nor decays in time. This leads to three different statements for the complex linear stability spectrum [20], $\Omega = \Omega_r + j\ \Omega_i$ which is now a function of the complex wave number, $\delta = q - j\,\kappa$. For given κ the real part of the wave number $q(\kappa)$ is chosen to maximize the growth rate,

$$\left(\frac{\partial \Omega_i}{\partial q}\right)_\kappa = 0 \qquad 6.15$$

yielding a one-parameter family of front velocities characterized by their asymptotic spatial decay rate, $v(\kappa) = -\Omega_i(\kappa)/\kappa$. Finally the selected velocity is chosen to minimize $v(\kappa)$.

The amplitude equation eq(6.11) has a negative nonlinear coefficient which classifies the bifurcation at zero ε as a supercritical one. For this case the front selected by the linear front selection analysis is the surviving front at long times. Applying this analyses to the linear part of the amplitude equation is straightforward and the selected wave number and velocity are as follows:

$$\kappa = -/+ \varepsilon^{1/2}/[\xi_0(c_1^2+1)^{1/2}] \qquad 6.16a\text{-}c$$

$$q = -c_1 \kappa$$

$$v = s_0 +/- \varepsilon^{1/2}\, 2\, \xi_0(c_1^2+1)^{1/2}/\tau_0.$$

Here, negative κ corresponds to the right front, in fig(6.7a). Eqs(6.16a,b) indicate that as the control parameter is increased the front solutions become spatially steeper and the velocities deviate from the group velocity. Note that the difference between the velocities increase with increasing ε. For large enough ε, the left front becomes stationary. This value of ε_a at which the transition to absolute instability occurs is given by:

$$\varepsilon_a^{1/2} = s_0\tau_0/[2\xi_0(c_1^2+1)^{1/2}]. \qquad 6.17$$

The transition value of ε_a is about 0.3 and for large β it is independent of any geometrical factors such as the angle between the pumps. The small value of ε_a is encouraging since the amplitude equation is expected to be correct near the threshold. However calculating κ_a from eq(6.16a) one finds that $\kappa_a\beta$ is close to unity and hence the small modulation expansion eq(6.9) may not expected to approximate Ω well.

Next we apply the linear front selection analysis to the starting equations, eqs(6.1a-c) and compare the results to the ones calculated from the amplitude equation. For this we

have to solve eq(6.5) numerically and calculate $(-2/\Gamma)$ as a function of the complex modulation wave number. The resulting values can be used in eq(6.6) to evaluate, Ω. For large β the analysis simplifies considerably. In this regime Ω can be treated as a function of $\kappa\beta$. We are interested in κ values of order $1/\beta$. For such small values of κ, the shift in the real part of the wave number eq(6.16b) is of order $1/\beta^2$ and can be neglected. So for a given κ the $q(\kappa)$ that maximizes the growth rate is zero. In this case $(-2/\Gamma)$, η^2, $\Delta \approx 2\kappa\beta$ in eq(5) are all real and $(-2/\Gamma)$, Δ are parametric functions of η^2. For a given real value of η^2 eq(5) gives $(-2/\Gamma)$ which in turn can be used in $\eta^2 = \Gamma\Delta + \Delta^2$ to be solved for $2\kappa\beta$.

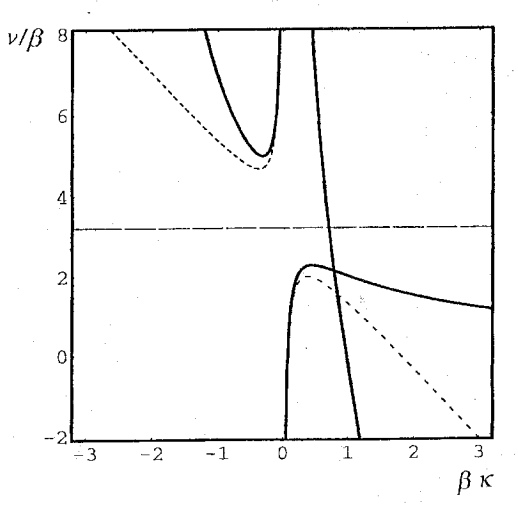

Figure 6.6 shows the family of front solutions selected for given spatial decay rate, $\nu(\beta\kappa)/\beta = -\Omega_i(\beta\kappa)/(\beta\kappa)$ as a function of $\kappa\beta$ for $\varepsilon = 0.05$, $\beta \approx 10^3$, $\alpha \approx 1$.

Fig(6.8) shows the family of front solutions selected for given spatial decay rate, $\nu(\beta\kappa)/\beta = -\Omega_i(\beta\kappa)/(\beta\kappa)$ as a function of $\kappa\beta$ for $\varepsilon = 0.05$, $\beta \approx 10^3$, $\alpha \approx 1$. Here, again positive $\kappa\beta$ corresponds to the fronts moving in the negative x direction. In this expression the geometric factor β is scaled out and hence the result presented in fig(6.6)

are independent of the angle between the pump beams. Clearly, the amplitude equation (dashed curve) works well for small $\beta\ \kappa$. However for $\beta\ \kappa$ values close to unity and larger the amplitude equation predicts a slower velocity for the right front solutions and a faster velocity for the left front solutions. Also note that an additional branch for the left fronts is attained from the starting equations. We expect that this branch may become important for the question of front selection as will be discussed in the next section. In addition other branches with η^2 less than - π^2can be found for the starting equations. However as seen from eq(6.4a-c) these branches correspond to an oscillatory z dependence. From the view point of matching the linear solution to the nonlinear uniform solution, the existence of such a front solution is unlikely hence we neglect these branches.

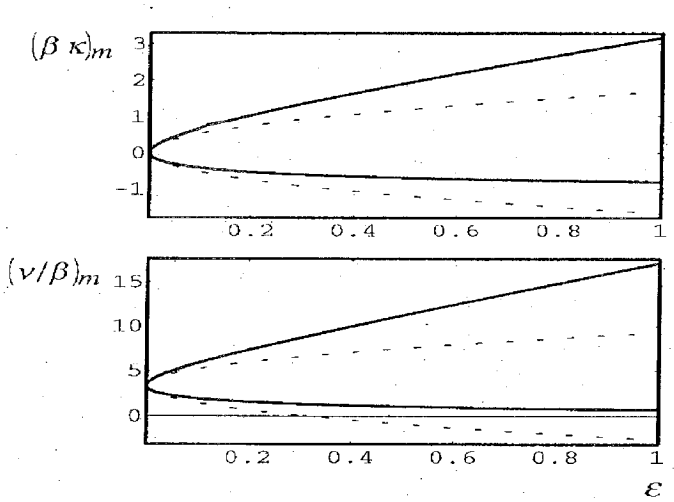

Figure 6.7a,b. selected fron solution predicted by the amplitude eqution (dashed), by the starting equations (solid).

According to the linear front selection criteria the maxima of the curves in fig(6.6) correspond to the selected fronts at long times. Fig(6.7a,b) illustrates the selected front velocities and spatial decay rates for different control parameter values. As shown in fig(6.7b) the selected front velocities are at most an order of magnitude larger than the group velocity. For typical parameters (τ_d=1sec, $\beta = 2\ 10^4$), front velocities in the figure

are less than 20cm/sec. For ε values less than 0.1 the predictions of the amplitude equation agree well with results obtained from the starting equations. The amplitude equation predicts a slower moving right front for larger values of ε. For the left front, the dependence of the front velocity on ε is much weaker than expected from the amplitude equation. However the velocity difference between the two fronts continues to increase with increasing ε. As seen in the figure, the solid curve does not cross the zero velocity near the parameters predicted by the amplitude equation and hence the transition to absolute instability does not take place.

In the remaining part of this section, we compare our approach for the classification of the instability to the one in ref(4). Utilizing observations from both works (both essentially employing a linear analysis) we will argue that in the large β limit and non-diffracting pump beams the linear analysis concludes that the transition to absolute instability does not take place. Then we describe some possible nonlinear front selection scenarios which the linear analysis cannot account for and which may lead to absolute instability for this simple geometry.

Ref(4) solves the linear problem exactly for nondiffracting pump and scattered beams in two dimensions. Similar to the pinch point analysis of the front selection problem, the poles of the Laplace transform of the exact solution are sought. The poles dominate the long time asymptotic of the inverse Laplace integral and hence a pole with a positive growth rate corresponds to an absolute instability. We have approached the problem from the point of view of front selection. Applying the linear front selection analysis, we look for saddle points of the complex linear stability spectrum and identify the transition point as the point when the growth rate (for the left front) at this saddle point become positive. It can be shown that the two analyses above lead to the same conditions on the liner stability spectrum eq(6.15). One of the main differences in this article is the starting equations. In our analysis we treat a more complicated material equation and we also allow the diffraction of the scattered beams, although the pump beams are non

diffracting waves. We already have shown that for the large β limit the wave number dependence of the photorefractive effects does not greatly influence the linear problem. The diffraction term in our formulation comes about as the δ^2 term in $\Delta = j\ \beta\ (\delta^2 + 2\ \delta)$, eq(6.3). The point is that essentially the wave number dependence of the linear stability comes about through Δ, eq(6.6). The saddle points are identified as:

$$\frac{d\Omega}{d\delta} = \frac{d\Omega}{d\Delta}\frac{d\Delta}{d\delta}. \qquad 6.18$$

Hence a saddle point in δ also corresponds to a saddle point in Δ. Ref(4) proves that for the small modulation δ limit a saddle point in δ does not exist, and then this clearly implies that the nonexistence of a saddle point in Δ. So from these observations we can conclude that even for very large modulations δ the sought after saddle point does not exist. From the point of view of a linear analysis we conclude that a transition to absolute instability does not take place for nondiffracting pump beams.

However front propagation is a nonlinear problem and there are examples known (Section(6.B.4) in ref(3), Section(4.2) in ref(14)) where nonlinear effects lead to a different selected front velocity than predicted by the linear analysis. Well into the nonlinear regime there is the possibility of the selection of a different front than the one predicted by the linear analysis, and then the transition to absolute instability may take place if a left front traveling towards negative x direction is selected, as in fig(6.7c). The question of non-linear front selection and front selection in situations with multi-branched dispersion curves, such as in fig(6.8), is poorly understood, and we can only point out possible scenarios for the breakdown of the "linear selection" predictions. For example in fig(6.8) we pointed out that for the starting equations (solid curves) two branches of front families are found at positive $\beta\ \kappa$. For an ε value about 0.1 the value of $(\beta\ \kappa)_m$ for the maximum

of the branch becomes larger than the $(\beta\kappa)_c$ value for the crossing point of the two branches. For larger ε values one can argue that two spatial decay rates are possible for a given front velocity. Out of the two, the smaller one will usually give the asymptotic dependence at large x. The most localized front, i.e. the one with the largest $\beta\kappa$ value, is then the one at the crossing point of the two branches, and might dominate the dynamics for $\varepsilon > 0.1$ (Section(3) in ref(20)), For $\varepsilon = 0.3$ the front velocity corresponding to the crossing point of the two branches (at $(\beta\kappa)_c$) becomes negative, and this would indicate a transition to absolute instability. For typical parameters the transition should result in a behavior as depicted in fig(6.7c), (τ_d=1sec, $\beta = 2\ 10^4$,$s\ =10^{-4}$, ε=0.3) where the expected change in the rate of spatial growth from the left boundary is from 2 cm^{-1} (convective instability) to 10 cm^{-1} (absolute instability). A possible way to study the effects of such multiple front branches would be to design a simpler equation, similar to the amplitude equation, that reproduces the linear stability spectrum characteristics The only certain way, however, to characterize the instability predicted by the starting equations seems to be to rely on careful numerical studies.

6) Summary and conclusions:

We have demonstrated an intuitive generalization of the 1-D [1] theory to a 2-D [4] theory by considering all the unstable grating modes nearby the phase conjugate mode. The generalization leads to a dispersion relationship, the linear stability spectrum, which captures the convective nature of the instability. We find that for typical experimental conditions (large β) the wave number dependence of the photorefractive effect has a small influence on the linear problem. However as β approaches unity (very small angle between the pump beams) the effects of the photorefractive effect are expected to become much more important.

We then derive the amplitude equation for the large β limit, which extends the linear analysis into the weakly nonlinear regime. In calculating the nonlinear coefficient the higher diffraction orders can be neglected due to the large selectivity of the most unstable volume hologram. However the contribution from the grating components with double the spatial frequency (and from other nonlinear terms in eq(6.1a)) leads to a strong wave number dependence for the nonlinear coefficient, eq(6.14d). At large angles between the pump beams the value of the coefficient approaches the one predicted by the 1-D theory where the saturation comes about due to the depletion of the pump beams. The sign of this coefficient characterizes the bifurcation at the threshold as a supercritical one, and the non-zero group velocity immediately implies that the instability is convective (i.e. the system is an amplifier at the threshold). The amplitude equation then provides an easy formulation for calculating the spatial distribution of the noise-driven solution in this regime, including the nonlinear saturation.

The possibility of a transition to an absolute instability is discussed in terms of selection criteria for the propagation velocity of a nonlinear front (the building block for constructing a physical picture for the spatial dynamics in the nonlinear regime). The simplest theory of selection, relying on a purely linear arguments, is investigated for the amplitude equation (where a transition to absolute instability is predicted) and for the starting equations. The comparison gives the expected result that the predictions of the amplitude equation are good only near the threshold. The early break down of the equation is primarily related to the fact that the small modulation expansion of the linear stability spectrum is actually an expansion in powers of $\beta\,\kappa$. As a result we find that the transition to absolute instability does not take place near the parameters predicted by the amplitude equation. However it is possible that such a transition may take place through other scenarios which the linear analysis cannot account for. We describe one such possibility that arises due to the multiplicity of the linear front branches and argue that the nonlinear

front solution corresponding to the crossing point of the two branches may be the selected front. In this case, the transition to absolute instability does take place near the threshold. It is also important to mention that in the experiments the spatial content of the pump beams play an important role: when the pump beams are simple plane waves conical light scattering appears to develop instead of phase conjugate beams [14]. Only when enough spatial information is added to the pump beam is the phase conjugate beam propagating in the backward direction with respect to the incident wave obtained. So experimentally, the physical problem is two dimensional only when the pump beams have enough spatial information, i.e. the pump beams diffract before exiting the crystal We are therefore cautious in calling the simple 4-wave mixing geometry studied above DPCM. However, the gain mechanism for the conical rings is the same grating sharing process, and the formation of the conical rings is attributed to the multiplicity of the perfectly shared gratings in the third dimension. At the present the effects of diffraction on the underlying physics is unclear. The amplitude equation formalism, allowing the treatment of both modulation and nonlinearity, provides a possible scheme to investigate this phenomenon theoretically.

In conclusion, we have derived an amplitude equation that governs the spatio-temporal behavior of the two-dimensional grating amplitude in the nonlinear regime, near the threshold. The equation renders the very difficult study of the nonlinear dynamical problem much more manageable. The regime in which the equation is expected to work well is precisely described.

Appendix A: Derivation of the Amplitude equation

Here we extend the linear analysis in section(6.3) to the nonlinear regime. The formulation presented below [17] is a standard perturbative approach to systems that exhibit spatial instability near a critical point. The approach has been rediscovered in many different contexts and bears a strong resemblance to the mean-field Landau theory of equilibrium phase transitions. Near the threshold the nonlinearities are weak and the spatial

and temporal modulations of the most unstable mode become slow. The balance between these effects is described by the amplitude equation. In what follows we will derive this equation for the regime $\beta >> 1$ (thick hologram). This derivation follows in close analogy with the appendix in ref(3).

We first express the right and left moving wave amplitudes in eq(6.1b,c) as a sum of the pump and scattered waves:

$$A = \overline{A_p}(z,t) \exp(-j x) + a(z,x,t) \qquad \text{6.A 1a-b}$$

$$B = \overline{B_p}(z,t) \exp(-j x) + b(z,x,t).$$

In our notation the bar on the amplitudes implies that the amplitude only depends on z and the amplitudes $\overline{A_p}$, $\overline{B_p}$ keep track of the depletion of the pump beams. In this notation the intensity profile is given by $i = 1 + 1/2(\overline{A_p}^* a + \overline{B_p}^* b) + c.c.$.

Near the transition point we define a perturbation parameter $\varepsilon = (\gamma_0 - \gamma_{0c})/\gamma_{0c}$, and we wish to separate fast and slow scales for x and t. The slow scales of the modulation are defined as:

$$X = \varepsilon^{1/2} x \ , \ T = \varepsilon t. \qquad \text{6.A2}$$

We will consider a, b, e ... to be given by products of functions of fast and slow variables. From the chain rule for differentiation we therefore must make the replacements

$$\partial_x \rightarrow \partial_x + \varepsilon^{1/2} \partial_X, \ \partial_x \rightarrow \partial_t + \varepsilon \partial_T. \qquad \text{6.A3}$$

In this analysis (to the order we take the expansion) ∂_X terms will show up only in linear terms in the amplitude equation which will come about at $O(\varepsilon^{3/2})$. These linear coefficients can be inferred from the linear stability analysis. For convenience we will ignore these terms in the present derivation and refer back to the linear stability analysis for their contribution. We now expand eqs(6.1a-c) consistently in $\varepsilon^{1/2}$,

$$
\begin{aligned}
a &= \varepsilon^{1/2} a_0 + \varepsilon a_1 + \ldots \\
b &= \varepsilon^{1/2} b_0 + \varepsilon b_1 + \ldots \\
e &= \varepsilon^{1/2} e_0 + \varepsilon e_1 + \ldots \\
i &= 1 + \varepsilon^{1/2} i_0 + \varepsilon i_1 + \ldots \\
\overline{A_p} &= 1 + \varepsilon \overline{A_{p1}} + \ldots \\
\overline{B_p} &= 1 + \varepsilon \overline{B_{p1}} + \ldots
\end{aligned}
\qquad \text{6.A4a-f}
$$

At $O(\varepsilon^{1/2})$ the eqns(1a-b) is of the form:

$$
L \begin{pmatrix} e_0 \\ a_0 \\ b_0 \end{pmatrix} + \begin{pmatrix} \alpha\ \partial_x\ i_0 \\ j\ 2\ \gamma_{0c}\ e_0 \exp(-j\,x) \\ -j\ 2\ \gamma_{0c}\ e_0 \exp(-j\,x) \end{pmatrix} = 0 \qquad \text{6.A5}
$$

where the linear operator L is defined as:

$$
L = \begin{pmatrix} 1 - \alpha^2\,\partial_x^2 & 0 & 0 \\ 0 & \partial_z - j\beta - j\beta\ \partial_x^2 & 0 \\ 0 & 0 & \partial_z + j\beta + j\beta\ \partial_x^2 \end{pmatrix} \qquad \text{6.A6}
$$

and the solution at this order is the phase conjugate mode:

$$a_0 = \overline{a_0}\exp(j\,x) = j\,(1+4\alpha^2)/\alpha\,A_0(T)\,z\;\exp(j\,x)$$

$$b_0 = \overline{b_0}\exp(j\,x) = j\,(1+4\alpha^2)/\alpha\,A_0(T)\;(1\text{-}z)\exp(j\,x) \qquad \text{6.A7a-c}$$

$$e_0 = \overline{e_0}\exp(2j\,x) + c.c. = A_0(T)\;\exp(2j\,x) + c.c.$$

where, we allow the amplitude of the threshold solution A_0 to vary with the slow time scale, T. Here, $\overline{a_0}$, $\overline{b_0}$, $\overline{e_0}$ are solutions to the linear equation (identical to the linearized 1-D theory):

$$L_0\begin{pmatrix}\overline{e_0}\\ \overline{a_0}\\ \overline{b_0}\end{pmatrix} = \begin{pmatrix} 1 & j\,\tilde{\gamma}/2 & j\,\tilde{\gamma}/2 \\ j\;2\;\gamma_{0c} & \partial_z & 0 \\ -\;2\;\gamma_{0c} & 0 & \partial_z \end{pmatrix}\begin{pmatrix}\overline{e_0}\\ \overline{a_0}\\ \overline{b_0}\end{pmatrix}. \qquad \text{6.A8}$$

The boundary conditions are $\overline{a_0}(0) = 0$, $\overline{b_0}(1) = 0$. At the first nonlinear order, $O(\varepsilon)$ the depletion of the pump beams appear.

$$\partial_z\begin{pmatrix}1 & 0\\ 0 & 1\end{pmatrix}\begin{pmatrix}\overline{A_{p1}}\\ \overline{B_{p1}}\end{pmatrix} = j\;2\;\gamma_{0c}\begin{pmatrix}\overline{a_0}\,\overline{e_0}^*\\ -\overline{b_0}\,\overline{e_0}^*\end{pmatrix} \qquad \text{6.A9a-b}$$

$$\begin{pmatrix}\overline{A_{p1}}\\ \overline{B_{p1}}\end{pmatrix} = -\,|A_0(T)|^2(1+4\alpha^2)^2/\alpha^2\begin{pmatrix}z^2\\ (1\text{-}z)^2\end{pmatrix}.$$

At this order we also have:

$$L\begin{pmatrix} e_1 \\ a_1 \\ b_1 \end{pmatrix} + \begin{pmatrix} \alpha\ \partial_x\ i_1 \\ j\ 2\ \gamma_{0c}\ e_1 \exp(-j\ x) \\ -j\ 2\ \gamma_{0c}\ e_1 \exp(-j\ x) \end{pmatrix} = \begin{pmatrix} -\alpha\ e_0\ \partial_x e_0 - e_0\ i_0 - \alpha^2\ \partial_x e_0\ \partial_x i_0 + \alpha^2\ i_0\ \partial_x^2 e_0 \\ -j\ 2\ \gamma_{0c}\ e_0\ a_0 \\ j\ 2\ \gamma_{0c}\ e_0\ a_0 \end{pmatrix}.$$

6.A10

Notice that on the right there are no secular terms of the form (exp(2 $j\ x$), exp($j\ x$), exp($j\ x$)). In the second and third rows of this equation the nonlinear terms that depend on the fast variable x, varying as exp(3 $j\ x$) or exp(-$j\ x$), correspond to higher diffraction orders. For $\beta >> 1$ it can be shown that these terms are strongly phase mismatched to the most unstable mode and can be neglected. We expect corrections from these terms to be of order Γ/β^2 and emphasize the point that these terms have to be considered for very small angles between the two pump beams (the thin hologram limit). However the nonlinear terms in the first row with x dependence of the form exp(4 $j\ x$) are not necessarily small and we have to keep the contributions from these terms. With the above considerations the solutions at this order can be expressed as:

$$a_1 = \overline{a_1} \exp(j\ x)\ ,\ b_1 = \overline{b_1} \exp(j\ x)$$

$$e_1 = \overline{e_{10}} \exp(\ 2j\ x) + \overline{e_{11}} \exp(\ 4j\ x) + c.c. \qquad 6.A11$$

The homogeneous problem for $\overline{e_{10}}$, $\overline{a_1}$, $\overline{b_1}$ is identical to the problem at $O(\varepsilon^{1/2})$ and $\overline{e_{11}}$ can be calculated from eq(A10) in a straight forward manner.

$$\overline{e_{11}} = -\ j A_0(T)^2/(2\alpha)\ \ (1 + 8\ \alpha^2)/(1 + 16\ \alpha^2)\ . \qquad 6.A12$$

Notice that this grating at double the most unstable wave number comes from the nonlinear terms in the material equation, eq(6.1a) and not from higher diffraction orders.

At $O(\varepsilon^{3/2})$ we introduce seed noise to the problem at the boundaries; $\overline{a_2}(0) = s_2$, $\overline{b_2}(1) = s_2$. We define $\overline{a_{2s}}$, $\overline{b_{2s}}$ as $\overline{a_2} = \overline{a_{2s}}+s_2$, $\overline{b_2} = \overline{b_{2s}}+s_2$ so that the linear problem for $\overline{a_{2s}}$, $\overline{b_{2s}}$ will have the same boundary conditions as in eq(6.A8). This introduces an additional term in the intensity distribution:

$$i_2 = i_{20} + i_{21} + i_s = 1/2(\overline{a_{2s}} + \overline{b_{2s}}) \exp(2jx) + 1/2(\overline{A_{p1}}^* \overline{a_0} + \overline{B_{p1}}^* \overline{b_0}) + s_2 \exp(2jx) + c.c. \quad \text{6.A13}$$

With the above definitions eqs(6.1a-c) become:

$$\tau_0^{-1} \xi_0^2 (1+jc_1) = -1/2 \left[\partial_\delta^2 (-j\Omega)\right]_{0,\gamma_{0c}} = \alpha^2 + 16/4L \begin{pmatrix} e_2 \\ a_{2s} \\ b_{2s} \end{pmatrix} + \begin{pmatrix} \alpha\, \partial_x i_{20} \\ j\,2\,\gamma_{0c}\, e_2 \exp(-jx) \\ -j\,2\,\gamma_{0c}\, e_2 \exp(-jx) \end{pmatrix} =$$

$$\begin{pmatrix} -\partial_t \overline{e_0} - \overline{e_{11}}\,\overline{i_0}^* (1+24\alpha^2) - 2j\alpha (\overline{e_{11}}\,\overline{e_0}^* + \overline{e_0}^2\,\overline{i_0}^* + \overline{i_{21}} + s_2) \exp(2jx) + c.c. \\ (-j\,2\,\gamma_{0c}\,\overline{e_0}\,\overline{A_{p1}} - j\,2\,\gamma_{0c}\,\overline{e_0}) \exp(jx) \\ (j\,2\,\gamma_{0c}\,\overline{e_0}\,\overline{B_{p1}} + j\,2\,\gamma_{0c}\,\overline{e_0}) \exp(jx) \end{pmatrix} 5\beta^2(1+4\alpha^2) + (1/3) j\beta (1+4\alpha^2)$$

6.A14

Here on the right only the secular terms are shown. With similar considerations the amplitudes e_2,a_2, b_2 can be expressed as in eq(6.A11) with amplitudes $\overline{e_{20}}$, $\overline{e_{21}}$. The secular part of eq(A14) becomes:

$$(1+4\,\alpha^2)\,L_0\begin{pmatrix}\overline{e_{20}}\\ \overline{a_{2s}}\\ \overline{b_{2s}}\end{pmatrix} =$$

$$\begin{pmatrix}-\partial_T A_0+A_0|A_0|^2\,(1+28\alpha^2+208\alpha^4+512\alpha^6)/[(1+16\,\alpha^2)4\alpha^2] - A_0|A_0|^2\,(1+4\,\alpha^2)^3[z^3+(1-z)^3]/(2\alpha^2) - 2j\,\alpha\,s_2\\ -j\,A_0|A_0|^2\,(1+4\,\alpha^2)^4/\alpha^3\,z^2 + j\,A_0(1+4\,\alpha^2)/\alpha\\ +j\,A_0|A_0|^2\,(1+4\,\alpha^2)^4/\alpha^3\,z^2 - j\,A_0(1+4\,\alpha^2)/\alpha\end{pmatrix}$$

6.A15

We would like to invert this equation but since the operator on the left has vanishing eigenvalues we must impose a "solvability condition," requiring that the vector on the right should not drive any eigenvector of the operator with zero eigenvalue. The condition for this is that the vector on the right hand side which we must now find, be orthogonal to the eigenvector with zero eigenvalue of the adjoint operator. The eigenvalue equation for the adjoint system (for zero eigenvalue) is of the form:

$$L_0^+\begin{pmatrix}\overline{e_0^+}\\ \overline{a_0^+}\\ \overline{b_0^+}\end{pmatrix} = \begin{pmatrix}1 & -j\,2\,\gamma_{0c} & j\,2\,\gamma_{0c}\\ -j\,\tilde{\gamma}/2 & -\partial_z & 0\\ -j\,\tilde{\gamma}/2 & 0 & -\partial_z\end{pmatrix}\begin{pmatrix}\overline{e_0^+}\\ \overline{a_0^+}\\ \overline{b_0^+}\end{pmatrix} = 0 \qquad \text{6.A16}$$

with boundary conditions $\overline{b_0^+}(0) = 0$, $\overline{a_0^+}(1) = 0$. The eigenvector is given by:

$$\begin{pmatrix}\overline{e_0^+}\\ \overline{a_0^+}\\ \overline{b_0^+}\end{pmatrix} = \begin{pmatrix}1\\ -j\,\alpha/(1+4\,\alpha^2)\,(z-1)\\ -j\,\alpha/(1+4\,\alpha^2)\,z\end{pmatrix}. \qquad \text{6.A17}$$

The inner product for the linear system is defined as:

$$\langle (x_1, x_2, x_3) \mid (y_1, y_2, y_3) \rangle = \int_0^1 dz \sum_i^3 x_i^* y_i \quad . \qquad 6.A18$$

The solvability condition requires the left-hand side of eq(6.A15) to be orthogonal to the adjoint eigenvector, eq(6.A17). The orthogonality condition results in the following amplitude equation :

$$-\partial_T A_0 + A_0 (1+4\alpha^2) - j\, 2\, \alpha\, s_2 + A_0 |A_0|^2 \left\{ \frac{(1+28\,\alpha^2+208\,\alpha^4+512\,\alpha^6)}{[(1+16\alpha^2)\,4\alpha^2]} - \frac{(1+4\alpha^2)^2}{(3\alpha^2)} \right\}.$$

(6.A19)

Returning to the unscaled units and expressing the amplitude as the amplitude for one of the scattered waves rather than the grating eq(6.A7a-c), we arrive at the general amplitude equation, ($A = \varepsilon^{-1/2} A_0 \; [-j\,\alpha/(1+\alpha^2)], \partial_T = \varepsilon^{-1}\, \partial_t, \; s = \varepsilon^{-3/2}\, s_2$).

$$\tau_0\, \partial_t A = \varepsilon A + 2\, s - g_0 |A|^2 A \qquad (6.A20)$$

References for Chapter Six:

(1) S. Weiss, S. Sternklar, and B. Fischer, Opt. Lett. **12**, 114(1987).

(2) D. Engin, S. Orlov, M. Segev, A. Yariv, G. Valley, Phys. Rev. Lett. **74**, 1743 (1995). M. Goulkov, S. Odoulov, R. Trott, Ukrainian Phys. J. **36**, 7, 1007(1991).

(3) M. C. Cross, P. C. Hohenberg, Rev. Mod. Phys. **65**, 851(1993).

(4) A. A. Zozulya, Opt. Lett. **16**, 545(1991); V. V. Eliseev, V. T. Tikchoncuk, A. A. Zozulya, J. Opt. Soc. Am. B. **8**, 12(1991).

(5) O. V. Lyubomudrov, V. V. Shkunov, Kvantovaya Elektron. **19**, 1102 (1992). S. Sternklar, Opt. Lett., 20, 3 249 (1995).

(6) D. Shaw, Opt. Comm **94**, 458 (1992).

(7) A. A. Zozulya, M. Saffman, D. Z. Anderson, Phys. Rev. Lett. **73**, 6, 818 (1994).

(8) W. Krolikowski, M. Cronin-Golomb, Opt. Comm. **89**, (1992). M. Segev, D. Engin, A. Yariv, G. C. Valley, Opt. Lett. **18**, 1828 (1993). A. A. Zozulya, M. Saffman, D. Z. Anderson, J. Opt. Soc. Am B **12**, 2, 255 (1995). M. R. Belic, J. Leonardy, D. Timotijevic, F. Kaiser, J. Opt. Soc. Am. B. **12**, 9 (1995).

(9) P. Gunter and J. P. Huignard, Eds., in *Photorefractive Materials and Their Applications,1* (Springer-Verlag, Berlin, 1989), Chap. 2.

(10) N. Kukhtarev, Sov. Tech. Phys. Lett. **2**, 438(1976).

(11) H. Kogelnik, Bell Sys. Techn. J. **48**, 2909 (1969).

(12) N. A. Korneev, S. L. Sochava, Opt. Comm. **115**, 539 (1995).

(13) N. V. Bobodaev, V. V. Eliseev, L. I. Ivleva, A. S. Korshunov, S. S. Orlov, N. V. M. Polozkow, A. A. Zozulya,, J. Opt. Soc. Am. B, **9**, 1493(1992).

(14) A. P. Mazur, A. D. Novikov, S. G. Odulov, M. S. Soskin, M. V. Vasnetov, J. Opt. Soc. Am. B, **10**, 1408 (1993). Q. B. He, P. Yeh, C. Gu, R. R. Neurgaonkar, J. Opt. Soc. Am. B, Vol. **9**, 114 (1992).

(15) M. Segev, D. Engin, A. Yariv, G. C. Valley, Opt. Lett. **18**, 956 (1993).

(16) M. Saffman, D. Montgomer, A. A. Zozulya, K. Kuroda, D. Z. Anderson, Phys. Rev. A. **48**, 4, 3209(1993).

(17) A. C. Newell, Lect. in App. Math. **15**, 157(1974).

(18) W. van Saarloos, P. C. Hohenberg, Physica D. **56**, 303(1992).

(19) M. C. Cross, Phys. Rev. Lett. **57**, 2935 (1986).

(20) W. van Saarloos, Phys Rev. A **39**, 6367(1989).

(21) A. Kolmogorov, I. Petrovsky, N. Piskunov, Bull. Univ. Moscow, Ser. Int. Sec. A **1**, 1 (1937). Aronson, D. G. , H. F. Weinberger, *Partial Differential Equations and Related Topics*, ed. J. A. Goldstein (Springer-Verlag, Heidelberg, 1975), p. 5.

(22) E. M. Lifshitz, L. P. Ptiaevskii, *Physical Kinetics*, (Pergamon New York, 1981), Vol. 10, Chap. 6.

Chapter seven

Photopolymerization dynamics

1.1 Introduction

Polymers are macromolecules that are built up by the linking together of a large number of much smaller molecules, called monomers. The reaction through which the monomers combine and form the polymers is called polymerization. Polymerization reaction is classified into step and chain polymerization [l(ch 1)]. In chain polymerization the average polymer size achieves a large steady value very early in the polymerization dynamics, while in step polymerization large polymers can be acquired only at the end of the polymerization reaction. In this chapter a summary of photoinitiated chain polymerization is described and a phenomenological model for the refractive index

change upon polymerization is presented. This model will be used to understand the grating dynamics observed in the holography experiments presented in chapter 8.

7.2 Photoinitiation mechanisms of free-radical polymerization

The monomers by themselves are typically inert and the chain polymerization reaction is initiated by a reactive species produced by bond cleavage or hydrogen-abstraction of a photoinitiator [2, 3]. When a photon is absorbed by the photoinitiator, a valence electron is excited to an unoccupied molecular orbital. Through rapid internal conversion the excited molecule reaches the lowest excited singlet state. In most of the photoinitiators singlet triplet energy splitting is usually small, and as a consequence intersystem crossing to the lowest excited triplet state proceeds rapidly and efficiently (1-0.9 quantum efficiency, [2]). The excited triplet state can go through unimolecular fragmentation (type 1) producing two reactive species (radicals) or it can form a single reactive species through bimolecular hydrogen-abstraction (type 2). The competing processes such as phosphorescence, and non-radiative decay of the triplets can often be neglected. However, quenching of the excited triplet states by oxygen results in the relaxation of the excited molecule to the ground state. Figure 7.1 shows various competing processes in producing reactive species from photoinitiators,

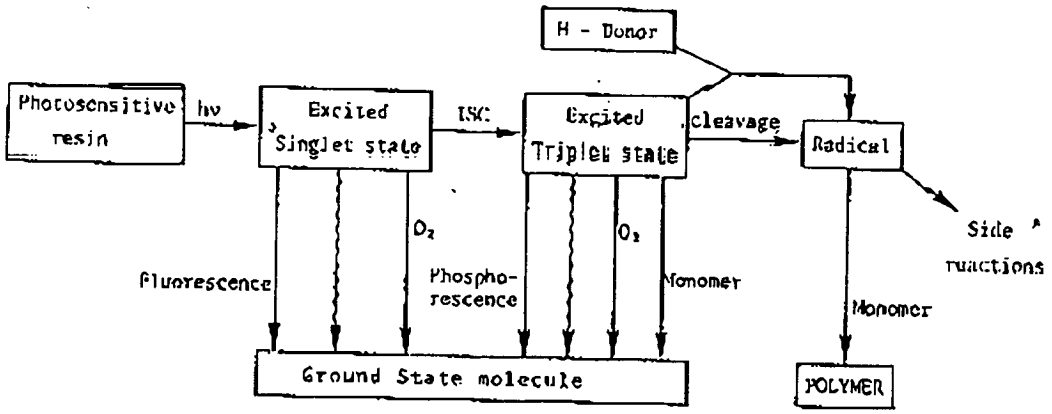

Figure 7.1. photoinitiation process, from reference [3]

The photoinitiation reaction can be represented as:

$$s + h \longrightarrow \dot{s} \qquad 7.1$$

where $\dot{s}$ is the reactive species. The local concentration of photoinitiators can change due to the production of radicals and diffusion. Equation 7.2 describes the two processes:

$$\frac{ds}{dt} - D_s \frac{d^2 s}{dx^2} = -\Phi I s \qquad 7.2$$

where s (mole/liters) is the molar concentration of photoinitiators and I is the incident intensity. Single spatial dimension is shown for simplicity (in accordance with

holography). The coefficient Φ depends both on the quantum efficiency of the photocleavage process and the cross section of photo-excitation. Equation 7.2 describes a straightforward dynamics where the initiator concentration is continuously being depleted. Photoinitiators are typically considered to be large molecules (compared to the monomers and oxygen) with diffusion constants less than $10^{-12} cm^2$ / sec [4]. In this work the initiator diffusion is neglected for the most part.

7.3 Chain propagation and termination

The reactive species that are produced by the photoinitiation, react with monomers, m_1 and produce reactive monomers. The propagation consists of the growth of the reactive monomers $\dot{m}_1$ by the successive additions of large numbers of monomer molecules, at each step producing a larger reactive polymer (or radical).

$$\begin{aligned}
&\dot{s} + m_1 \longrightarrow \dot{m}_1 \\
&\dot{m}_1 + m_1 \longrightarrow \dot{m}_2 \\
&\dot{m}_2 + m_1 \longrightarrow \dot{m}_3 \\
&\cdot \\
&\cdot \\
&\cdot \\
&\dot{m}_n + m_1 \longrightarrow \dot{m}_{n+1}.
\end{aligned} \qquad 7.3$$

The quick growth of the polymer molecule by successive addition of monomers is the characteristics of the chain polymerization. In step polymerization the growth of the

polymer takes place via the reaction of two large molecules. The chain propagation reaction rate is assumed to be independent of the size of the reactive species [l(ch.3-3)]. The propagation reaction is mainly limited by the mobility of the monomer molecules finding the reactive site on the large reactive polymers.

The propagation of the polymer chains can terminate by two different processes. In one scheme two growing reactive polymer molecules (radicals) react with each other forming one (coupling) or two non-reactive (disproportionation) (dead) polymer molecules.

$$\begin{aligned} \dot{m}_j + \dot{m}_k &\longrightarrow m_{j+k} \\ \dot{m}_j + \dot{m}_k &\longrightarrow \dot{m}_{j+k} \end{aligned} \qquad 7.4$$

From the view point of the polymerization reaction these non-reactive polymers no longer can react with another reactive species as in equation 7.3 and they do not contribute to the chain propagation. Again this is a critical point that differentiates between chain polymerization and step polymerization.

The propagation of the polymer chain can also terminate by bimolecular interaction of the reactive polymer molecule with an impurity within the solution, such as oxygen [5]. The reaction results in a non-reactive polymer molecule and other byproducts that no longer take part in the polymerization reaction.

$$\dot{m}_j + o \longrightarrow m_j \qquad 7.5$$

Typically oxygen termination reaction rate is much larger than the propagation rate in equation 7.3. Thus the oxygen tends to inhibit the growth of the reactive polymers very early in the propagation reaction, effectively inhibiting the polymerization process. Both of the termination reaction constants are generally taken to be independent of the reactive polymer size. For the case of termination by oxygen, the mobility of the oxygen is the important factor and the dependence on the radical size is not expected. Termination by the interaction of the two large radical molecules involve both the diffusion of the molecules through the pool of monomers (translational diffusion), and once the molecules are close enough the respective reactive ends of the molecules need to find each other (segmental diffusion) [l(ch. 3-lOb)]. It is more reasonable to expect the size independence to be accurate for the cases where the segmental diffusion is the rate limiting factor.

The above reactions can be expressed in terms of chemical rate equations:

$$\begin{aligned} \frac{d\dot{s}}{dt} &= -\frac{ds}{dt} - k_p \dot{s} m_1 - k_c o \dot{s} - 2k_t \dot{s} \sum_j \dot{m}_j \\ \frac{d\dot{m}_k}{dt} &= k_p \dot{m}_{k-1} m_1 - k_p \dot{m}_k m_1 - k_c o \dot{m}_k - 2k_t \dot{m}_k \sum_j \dot{m}_j \end{aligned} \qquad 7.6$$

where the diffusion of the radicals is ignored. Typically reactive species (radicals) concentrations come to a quasi-steady-state distribution early on in the polymerization

dynamics. Thus a large fraction of these reactive polymers are large molecules and their diffusion can be neglected compared to the smaller, monomers and oxygen. Because the propagation (k_p) and termination (k_t, k_c) rate constants are taken to be independent of the size of the reactive polymers, the equation 7.6 can be transformed into an equation for the total reactive polymer concentration $r = \sum_j \dot{m}_j$,

$$\frac{dr}{dt} = R_i - k_c or - 2k_t r^2 \qquad 7.7$$

where $R_i = -\frac{ds}{dt}$ the photoinitiation rate. Chain propagation effectively does not change the total number of reactive polymers (radicals) and it does not contribute to equation 7.7. The rate equations for monomers and oxygen include diffusion:

$$\begin{aligned} \frac{dm}{dt} - D_m \frac{d^2 m}{dx^2} &= -k_p mr \\ \frac{do}{dt} - D_o \frac{d^2 o}{dx^2} &= -k_p or \end{aligned} \qquad 7.8$$

Equations 7.7 and 7.8 can be solved selfconsistently for the monomer, oxygen and total radical molar concentrations. The polymerization dynamics ends when all the monomers are depleted (become part of a polymer chain). However these equations tell very little about the characteristics of the final polymer material, such as average length of polymer chains, and the distribution of chain lengths of the polymers. In principle the

following equation for the dead polymer chains can be acquired from the described reactions:

$$\frac{dm_k}{dt} = 2k_t \sum_j \dot{m}_j \dot{m}_{k-j} . \qquad 7.9$$

Clearly this is not a convenient expression from the point of view of calculations. There are numerical studies that start from this point, ref [6]. One can assume at least in the beginning of the polymerization dynamics (before gelation and increased viscosity changes the reaction constants) the average polymer chain length (distribution as well) is independent of time. This assumption is true as long as the illumination intensity is constant. This behavior follows from the relatively fast dynamics exhibited by the radicals. Radical chain distribution achieves a constant shape very early in the dynamics and the radical chain distribution defines a polymer length distribution, equation 7.9. So assuming that the polymer length distribution does not change for the most part of the polymerization dynamics, it is possible to define a (polymer) length independent equation for the dead polymers. As mentioned before molecular length distribution can be calculated for polymerization restricted to low conversions where all of the kinetic parameters (m, k_t, k_p, s, I) are constants, [l(ch 3.11, 7)].

$$\begin{aligned} N_x &= N_0(1-p)p^{x-1} \\ \langle x \rangle &= 1/(1-p) \\ p &= \frac{k_p m}{k_p m + \sqrt{2\Phi I s k_t}} \end{aligned} \quad , \qquad 7.10$$

where N_x, N_0, $\langle x \rangle$ are the number of polymers with length x, the total number of monomers and the average chain length respectively. Typically p is very close to one thus the average length of polymers tend to be in the order of thousands. Simplest way to model the polymer concentration dynamics is to assume that all the polymers that form have the same length, (for instance the average polymer length in equation 7.10). For every $\langle x \rangle$ monomers that are eaten up by the chain propagation process (not diffusion), one polymer molecule will be produced. This is described by the following rate equation for the molar concentration of polymers, p.

$$\frac{dp}{dt} = \frac{k_p}{\langle x \rangle} mr \, . \qquad 7.11$$

Equation 7.7, 7.8, 7.10 constitutes the dynamical model used in this study. The change in the index of refraction which comes about mainly due to the density changes, is assumed to be proportional to the polymer molar concentration. The proportionality constant is expected to depend on the characteristics of the final polymer network, i.e. average polymer length. This simplistic model assumes that the average length of the polymer

chains do not change considerably during the polymerization reaction. According ref[l(ch 3.11b)], the effects due to decrease in m, and the gelation (changing k_p, k_t) mainly result in the broadening of the polymer length distribution.

7.4 Refractive index changes upon photopolymerization

Large index changes take place upon chain polymerization. The positive index change mainly comes about due to large density changes of the sample upon polymerization. For this reason dilatometry has been used to measure polymerization dynamics in chain polymerization [8]. This large volume change is also a differentiating characteristic of the chain polymerization from step polymerization where small by-products of the reaction result in no appreciable volume change [1, 3-3c-3]. A smaller negative index change due to changes in the polarizabilities is also expected [9], for example in diacrylate and triacrylate monomers, the electronic polarizability decreases upon polymerization because a double bond is replaced by the two single bonds. A density change $\Delta\rho$ produces a following index change [9]:

$$\Delta n = \frac{(n^2+2)(n^2-1)}{6n}\frac{\Delta\rho}{\rho}. \qquad 7.12$$

For $n = 1.5$ this gives $\Delta n = 0.59\frac{\Delta\rho}{\rho}$. Index changes as large as 0.01 can be obtained by polymerization. In what follows we argue that the density change is proportional to the molar density of polymers. The experimental results presented in the next chapter shows the validity of this assumption.

The argument relies on the fact that during the polymerization reaction the monomer units are not destroyed, but they become part of a polymer unit. Thus the quantity $N_m(0) = N_m(t) + N_p(t)\langle x\rangle$, where N_m, N_p are moles of monomer and polymer molecules in the mixture, is expected to be conserved. The overall density changes because of the volume change associated with the more densely packed polymers. If on the average a monomer molecule occupies a volume, V_m, we assume that a polymer molecule occupies slightly less than the volume occupied by $\langle x\rangle$ monomers, in this way the density of monomer, polymer mixture can be expressed as:

$$\rho = \frac{N_m(0)\,M}{N_m V_m + N_p(\langle x\rangle V_m - \Delta V)} \qquad 7.13$$

where M is the molecular weight of the monomer unit. Initial and final densities during the polymerization reaction are given by $\rho_i = M/V_m$, $\rho_f = \rho_i(1 + \Delta V/(\langle x\rangle V_m))$. For small ΔV the volume change takes a form where the density changes are proportional to the polymer molar density:

$$\frac{\Delta\rho}{\rho} = \frac{p}{m(0)} \frac{\Delta V}{V_m}. \qquad 7.14$$

The proportionality of the index change to polymer molar concentration (or equivalently to degree of polymerization) is argued here in a very simplistic way. The linearity is assumed in a number of other studies [10, 8].

7.5 Summary

A standard model that is used for studying chain photopolymerization dynamics is described. The kinetic equations of the model capture dominant reactions that are expected to take place during the photopolymerization. Photoinitiators absorb incident photons and become reactive species which initiate the chain propagation. During the chain propagation the reactive species successively grow by eating up nearby monomers. The growth of these large reactive molecules terminate when two such molecules react or when the molecules reacts with oxygen. This model will be used to understand the rich dynamics exhibited in holographic photopolymerization studies presented in chapter eight.

References for Chapter Seven

[1] G. G. Odion, in *Principles of Polymerization* (Wiley-Interscience Publications, 1981)

[2] H. J. Hageman, Chapter 1 in *Photopolymerization and Photoimaging science and Technology*, edited by Norman S. Allen (Elsevier Applied Science, London, New York, 1989).

[3] C. Decker, in *Handbook of Polymer Science and Technology*, N. . Cheremisinoff, Ed. (M. Dekker, New York, 1989), vol. 3, pp. 541-608.

[4] Vadim V. Krongauz, Chapter 5 in *Processes in Photoreactive Polymers*, edited by V. V. Krongauz A. D. Trifunac (Capman and Hall, 1995).

[5] T. Koenig, H. Fischer, Chapter 4 in *Free Radicals*, Vol. 1, edited by J. K. Koci, (Wiley, New York, 1973).

[6] K. W. McLaughlin, D. D. Latham, C. E. Hoyle, and M. A. Trapp, J. Phys. Chem. **93**, 3643, (1989).

[7] L. H. Pebles, Jr., Chapter 2 in *Molecular Weight Distributions in Polymers*, (Wiley-Interscience, New York, 1971).

[8] E. A. Collins, J. Bares, F. W. Billmeyer, Chapter 5 in Experiments in Polymer Science, (Wiley-Interscience, New York 1973).

[9] W. J. Tomlinson, E. A. Chandross, in *Advances in Photochemistry*, J. J. N. Pitts, G. S. Hammond, K. Gollnick, Eds, (Wiley, New York, 1985), 12, pp. 201-281.

[10] J. de Boer, R. J. Visser, G. P. Melis, Polymer, **33**, 6 1123 (1992).

Chapter eight

Holographic Characterization of Photopolymers

8.1 Introduction

In this chapter we present a study of photopolymerization dynamics with holography. The kinetic model presented in chapter seven is taken as the starting point. This model is general; with some modifications it is applicable to number of holographic materials [9]. Expected dynamics for typical holographic experiments is a complicated aggregate behavior of number of time constants. A characterization scheme that isolates various mechanisms in the reaction is presented in section 8.3. The technique is verified with holography experiments in section 8.4. In the experiments photopolymerization of various multifunctional acrylate monomers is studied.

8.2 Linearized model

The kinetic equation for total radical, monomer, photoinitiator, oxygen and polymer molar concentrations are derived in chapter 7, equations 7.2, 7.7, 7.8 and 7.10. The proportionality of the refractive index change to the polymer molar concentration is implied everywhere in this study, unless specified otherwise. Holography involves the illumination of the photopolymer by a sinusoidally varying intensity pattern, $I = I_0 + I_1 \exp(i\kappa x) + c.c.$. In the regime where the intensity modulation is small, i.e. $I_0 >> I_1$, the kinetic equations take the following form for the d.c. spatial components:

$$\frac{ds_0}{dt} = -\Phi I_0 s_0$$
$$\frac{dr_0}{dt} = -2k_t r_0^{\,2} - k_c r_0 o_0 + \Phi I_0 s_0$$
$$\frac{dm_0}{dt} = -k_p r_0 m_0 \qquad \text{8.1a-e}$$
$$\frac{do_0}{dt} = -k_c r_0 o_0$$
$$\frac{dp_0}{dt} = \frac{k_p r_0 m_0}{\langle x \rangle}.$$

The contributions to the above equations from spatially varying components are of order $o(I_1/I_0)^2$. The photoinitiators are depleted with time constant $1/(\Phi I_0)$, which is proportional to the inverse of average spatial intensity. Before the photoinitiators get

totally depleted polymerization needs to take place. Polymerization rate is proportional to the radical concentration, r_0. Thus the radical concentration has to build up for the polymerization reaction to occur. Oxygen is typically much more reactive with radicals than the monomers ($k_c >> k_p$) and oxygen tend to consume the radicals, not allowing significant polymerization to take place (inhibition). The thresholding effect due to oxygen can be seen by dividing equations 8.1c and 8.1d and integrating the resulting equation [7(ch. 3.7)]. This results in the following relationship between the time dependent oxygen and monomer concentrations: $(m/m(0) = (o/o(0))^{k_p/k_c})$. The relationship implies that most of the oxygen must be consumed before a significant amount of polymerization takes place.

Typically radicals exhibit a very fast dynamics and a quasi-steady-state condition can be assumed for radicals [7, ch. 3.3b]. Below the threshold the quasi-steady-state value of the radical concentration is $r_{0s} = \Phi s_0 I_0 / (k_c o_0)$, and $k_c o_0$ is rate with which the quasi-steady-state condition is achieved. Above the threshold, all of the oxygen is completely consumed. In this regime, the quasi-steady-state radical concentration is proportional to the square root of the incident average intensity, $r_{0s} = \sqrt{\Phi s_0 I_0 / (2k_t)}$. Radicals achieve the quasi-steady-state value with rate $\sqrt{\Phi s_0 I_0 2k_t}$.

Below the threshold, the oxygen concentration decreases linearly in time $o_0(t) = o_0(0) - \Phi s_0(0) I_0 t$ for a cw illumination (assuming slow initiator depletion) and an effective threshold fluence can be found from this expression as: $E_t = o_0(0)/(\Phi s_0(0))$. Note that from the threshold fluence, the molar concentration of

oxygen can be calculated. Above the threshold the polymerization takes place with a rate proportional to the square root of average intensity, $k_p\sqrt{\Phi s_0 I_0/(2k_t)}$. This unique square root dependence of the photopolymerization dynamics has a number of important consequences which are discussed in the later sections. The square root dependence arises from the bimolecular termination reaction of two radicals. In reference [6], photopolymerization within a polymer matrix is studied in DuPont photopolymers. In these chemicals a chain transfer agent that has comparable reactivity with radicals as monomers, dominate chain termination and result in a linear dependence of the polymerization rate on intensity. We will show that for the reactions considered in this study, the square root dependence is dominant.

In the presence of the intensity modulation I_1, all the chemical concentrations also exhibit spatial variation primarily with the same spatial frequency κ. The total radical concentration can be written as:

$$r = r_0 + r_1 \exp(i\kappa x) + c.c. + o(I_1/I_0)^2, \qquad 8.2$$

where r_1 is the complex amplitude of the radical concentration component with spatial frequency κ. Similarly we can define, the complex amplitudes m_1, p_1, s_1. The chemical rate equations for these amplitudes have the following form:

$$\frac{ds_1}{dt} = -(D_s\kappa^2 + \Phi I_0)s_1 - \Phi I_1 s_0$$
$$\frac{dr_1}{dt} = -4k_t r_0 r_1 + \Phi(I_0 s_1 + I_1 s_0)$$
$$\frac{dm_1}{dt} = -(D_m\kappa^2 + k_p r_0)m_1 - k_p r_1 m_0 \qquad 8.3$$
$$\frac{dp_1}{dt} = \frac{k_p r_0 m_1}{\langle x \rangle} + \frac{k_p r_1 m_0}{\langle x \rangle},$$

where the oxygen concentration is neglected (conditions above the threshold are assumed).

The corrections to the above equations due to higher order spatial frequency components are of order $o(I_1/I_0)^3$. Under c.w. illumination with I_0, and I_1 both present, above equations exhibit a complicated dynamic behavior and it is very difficult to isolate various dynamical constants from looking at the aggregate dynamics.

The basic behavior can be summarized as follows: the spatially varying radical concentration, r_1 is for the most part under quasi-steady-state conditions. The radical distribution has both in phase and an out-of-phase (spatially) component with the intensity pattern, I_1. The in-phase component comes about from the $I_1 s_0$ term (regions with larger illumination see a larger production of radicals) and out-of-phase component comes from $I_0 s_1$ (regions with larger illumination also see a larger depletion of the initiators) in equation 8.3b. Early on in the dynamics (when the illumination is first started) the in-phase component is stronger (since the chemical solution have plenty of initiators) and this results in the formation of an in-phase grating as depicted by $k_p r_1 m_0$

term in eq 8.3d. As the polymerization continues the initiator concentration depletes, s_1 increases and for $I_0 s_1 > I_1 s_0$ the radical concentration becomes out-of-phase with the intensity distribution. The inphase grating formation early on in the dynamics, also results in the formation of an out-of-phase concentration of monomers m_1 (with respect to I_1), signifying the greater consumption of monomers in the bright regions. Thus both terms $k_p r_0 m_1 + k_p r_1 m_0$ in equation 8.3d are expected to become out-of-phase with the intensity pattern well into the dynamics and erase the in-phase grating (to an extend) written early on in the dynamics. At long times a fixed in-phase grating or an out-of-phase grating is expected depending on the values of the kinetic parameters. In the presence of strong monomer diffusion $k_p r_0 m_1$ term remains small (compared to the $k_p r_1 m_0$) causing little erasure of the in-phase grating. If the rate of photo-initiator decay (ΦI_0) is small compared to the photopolymerization rate, very little depletion of photo-initiators is expected (s_1 remains small), again leading to small erasure of the in-phase grating.

It is important to note that for realization of a fixed grating (by long time exposure) it is not essential to have strong monomer diffusion. If the polymerization reaction stops before completion, signifying the radical concentration decaying to zero, (due to depletion of the photo-initiators (large ΦI_0) or extreme slowing down of the polymerization rate due to gelation (crosslinking)) then it is possible to have a finite fixed grating. This will be discussed in section 8.6.

8.3 A characterization technique of the polymerization dynamics

As it was described in section 8.2, even in the case of low modulation (intensity) regime the photopolymerization dynamics and the expected dynamics exhibited by the grating amplitude, is an aggregate dynamics consisting of many time constants. In what follows we describe a technique through which it is possible to isolate dynamics exhibited by oxygen, monomers, initiators and the radicals and measure various kinetic parameters.

For characterization, it is favorable to make the initiator dynamics much slower than the polymerization dynamics. The ratio of the polymerization rate to photo-initiator decay rate is given by:

$$\frac{R_p}{R_{in}} = \frac{k_p}{\Phi I}\sqrt{\frac{s(0)\Phi I}{2k_t}}. \qquad 8.4$$

This ratio can be made large by increasing initiator concentration and by operating at low intensities. If the photo-initiator is of the kind that bleaches upon photo-cleavage, then the photo-initiator decay rate can be measured independently by a transmission experiment.

From experimental point of view it is advantageous to write a grating for a short time, during which the interference pattern is likely to be stable. The recipe for the characterization technique is to have one of the writing (stronger) beams on at all times, and turning the much weaker second writing beam on for short time during which a weak

grating is written. Since one strong beam is on at all times, (as describe in section 8.2) the d.c components of the chemical concentrations are expected to follow straightforward dynamics. The oxygen concentration will linearly decrease and when the oxygen is almost completely depleted the radical concentration very quickly achieves a quasi-steady-state value, $r_{0s} = \sqrt{\Phi s_0(0) I_0 / (2k_t)}$. The polymerization takes place exponentially with polymerization rate, $R_p = k_p r_{0s}$. Figure 8.1 illustrates the dynamics that is expected for the various dc kinetic concentrations.

When the second beam is turned on, spatially varying amplitude of the radical concentration quickly increases to the quasi-steady-state value which is in phase with the intensity pattern, $r_{1s} = s_0(0)\Phi I_1 / (4k_t\, r_{0s})$, (with time constant $\tau_1 = 1/(4k_t r_{0s})$). During the time second beam is on (Δt) which is chosen to be short compared to polymerization dynamics, $m_{10} = -k_p m_0(0) r_{1s} \Delta t$ (out-of-phase with I_1) can achieve only a small value. The in phase component, $k_p m_0(0) r_{1s}$ in equation 8.3c dominates, and an inphase grating, $p_1 = -m_{10} / \langle x \rangle$ develops during Δt, figure 8.2.

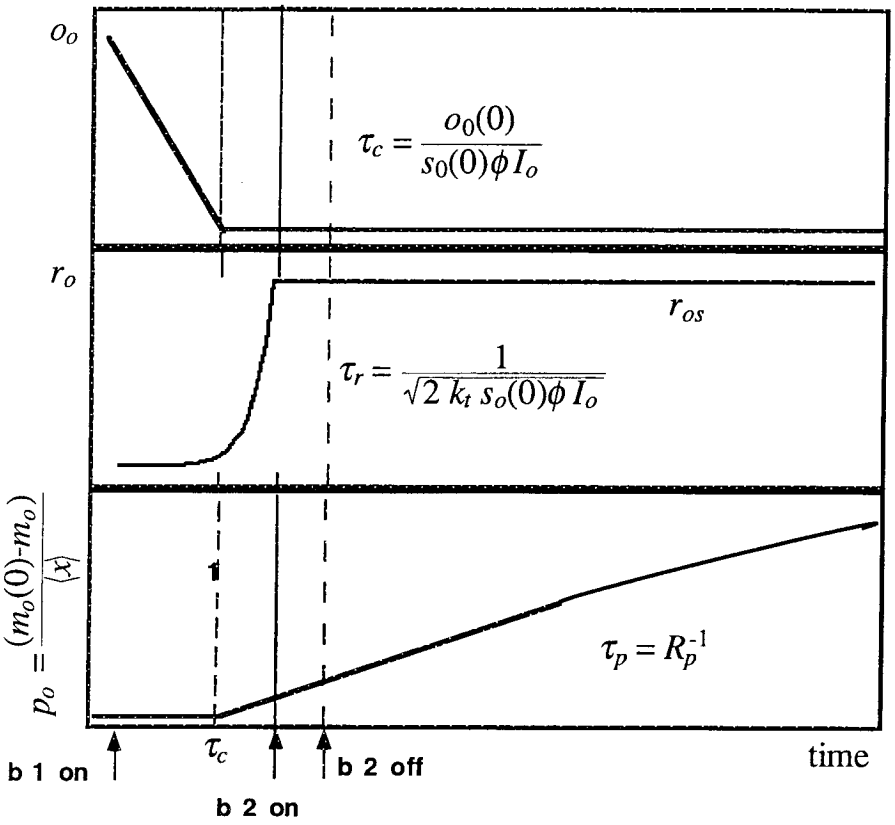

Figure 8.1 dynamics of the spatial dc components of the kinetic concentrations. The second weak beam is turned on and off for a short time. The initiator concentration is constant in the time frame shown.

When the second weak beam is turned off the spatially varying component of the radicals quickly decays, r_1, (figure 8.3) leaving behind the out-of-phase component $k_p r_{0s} m_{10}$ in equation 8.3d. This results in the gradual erasure of the existing in-phase grating.

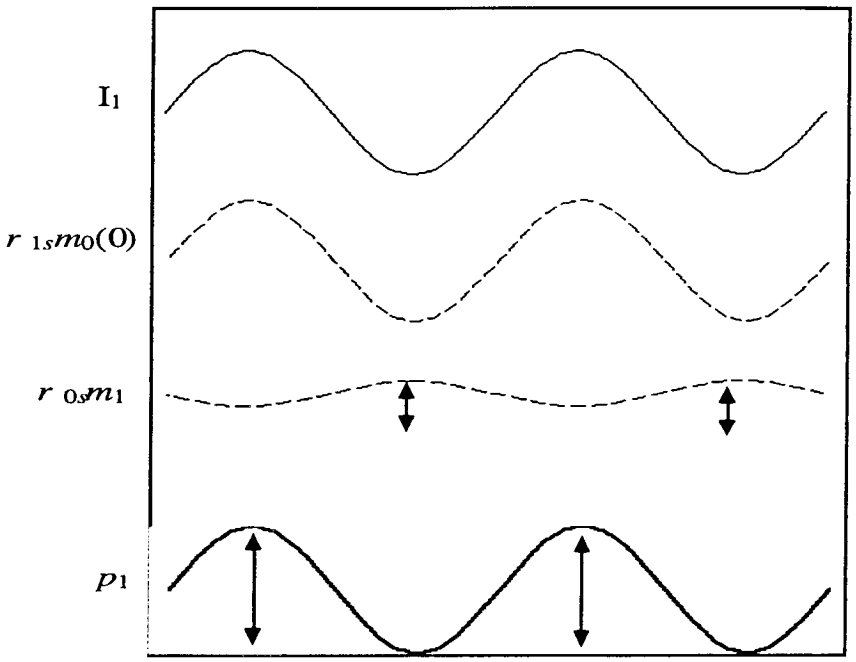

Figure 8.2, illustrates the in-phase and out-of-phase components of the polymerization rate during Δt. In-phase component dominates and an in-phase grating develops.

The spatially varying component of the monomer concentration m_1, decays with time constant, $\tau_2 = 1/(k_p r_{0s} + D_m \kappa^2)$. In the case where the monomer diffusion is large m_1 decays quickly and in-phase grating is not erased significantly. However in the absence of monomer diffusion the grating is erased completely. The final fixed grating amplitude can be easily calculated from equations 8.3:

$$p_1 = \frac{m_{10}}{\langle x \rangle}\left(1 - \frac{k_p r_{0s}}{k_p r_{0s} + D_m \kappa^2}\right). \qquad 8.5$$

In the experiment it is convenient to measure the radical dynamics by measuring the amount of time it takes for the condition $\frac{dp_1}{dt} = 0$ to be true. On figure 8.3 this point refers to the peak of the p_1 curve. This condition is satisfied when $r_{0s}m_{10} = r_1 m_0(0)$, which can be calculated to be:

$$\tau_3 = \tau_1 Ln[1/(r_{0s}k_p\Delta t)] \qquad 8.6$$

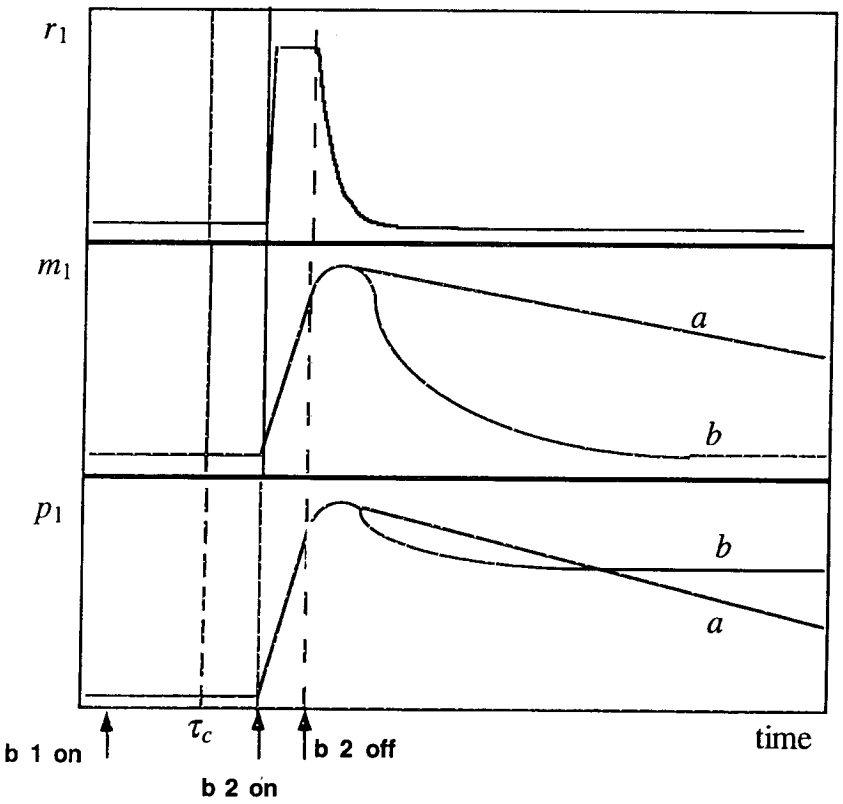

Figure 8.3 the dynamics exhibited by the spatially varying components of the chemical concentrations. a-refers to a case when the monomer diffusion is large, b-monomer diffusion is small.

The decay rate of the grating determines τ_2 which is equal to $1/(r_{0s}\, k_p)$ (at high intensities or small grating spacing), and it allows one to measure the ratio $k_p/\sqrt{k_t}$. Together with the measurement of the τ_3 one can determine both kinetic constants, k_p, k_t. Once these kinetic constants are known, the monomer diffusion constant can easily be acquired from τ_2. More importantly from the qualitative behavior of the dynamics it is easy to see if the monomer diffusion is present.

One important effect which is not directly accounted for within the model is the effects of increasing viscosity and crosslinking on the dynamical constants, k_p, k_t or Trommsdorff effect [7 ch 3-lOa]. Typically in the very beginning of the polymerization dynamics the rate constants are expected to remain constant (up to 5% conversion), then depending on the particular monomer, the ratio $k_p/\sqrt{k_t}$ or the polymerization rate is first expected to go up (autoacceleration). At this stage the termination rate, k_t is expected to decrease considerably due to increased difficulty for the large radicals to find and react with each other. However as the viscosity (at higher percent conversions) increases further, k_p decreases as well and the polymerization rate is expected decrease, possibly stopping the polymerization reaction completely before all the monomers are depleted [1]. Similarly one may expect large decreases in the monomer diffusion constant as well. As a result the exponential decay depicted in figure 8.3c is expected to be distorted. One can model these effects by assuming an arbitrary time dependence for

$k_p r_{0s}$ and $D_m \kappa^2$. It is interesting to note that if $k_p r_{0s} >> D_m \kappa^2$ at all times during the polymerization then the grating in figure 8.3c is expected to be erased completely independently of the gelation effect.

Another interesting point is that a scaling of the dynamics with $\sqrt{I_0}$ can be expected if $k_p r_{0s}$ and $D_m \kappa^2$ change in time only as a function of m_0 due to gelation (or the percent conversion). This is a physical assumption because the viscosity effects are expected to be only functions of the relative composition of the polymer, monomer mixture. With the above assumption equation 8. lb can be written as:

$$\frac{dm_0}{dt} = -\sqrt{\Phi I_0 s(0)} f(m_0) m_0, \qquad 8.7$$

where the scaling of the m_0 dynamics with $\sqrt{I_0}$ is clear. The rate equation for r_1, equation 8.3 b, can be expressed as:

$$\frac{dr_1}{dt} = -4\sqrt{\Phi I_0 s_0} f(m_0) r_1 + source, \qquad 8.8$$

where in equations 8.7,8 the function $f(m_0)$ symbolizes some arbitrary function, they are not meant to be the same function in the two equations. Equation 8.8 shows that the scaling with $\sqrt{I_0}$ also works for r_1 dynamics. Lastly the rate equation for m_1 can be expressed as (during the erasure of the in-phase grating):

$$\frac{dm_1}{dt} = -\sqrt{\Phi I_0 s_0} f(m_0) m_1 - g(m_0)\kappa^2 m_1, \qquad 8.9$$

where on the right-hand side the second term represents the decay of m_1 due to monomer diffusion. From equation 8.9 we conclude that the scaling of m_1 or p_1 dynamics with $\sqrt{I_0}$ is expected only when the monomer diffusion is small (for $k_p r_{0s} >> D_m \kappa^2$). Note that this scaling of the dynamics by $\sqrt{I_0}$ is due to the bifunctional termination reaction of two radicals, section 7.3. In the case of termination due to chain transfer as discussed in ref[6] (experiments performed in DuPont photopolymer), a linear scaling with the average intensity is expected.

8.4 Experimental demonstration of the characterization technique

In this section we describe photopolymerization experiments carried out with a multifunctional monomer, TMPTA from UCB Radcure. Irgacure 369 from Ciba-Geigy is used as the photo-initiator. A monomer, photo-initiator solution is prepared with 0.1 weight percent photo-initiator concentration. From this an initial initiator molar concentration of $s_0(0) = 3 \cdot 10^{-3}\ M/L$ can be calculated. Irgacure 369 exhibits bleaching upon photo-cleavage [8] and thus a transmission experiment (at 325 nm from HeCd laser) is carried out in order to determine the decay rate of the photo-initiators delta $I_0\Phi$.

Monomer mixture is placed in between two glass plates, (no spacer is used). A monomer film thickness of typically 50-20 micron is acquired. Approximately 8 percent change in transmission is observed upon photo-polymerization, from which the absorption within the polymer film is concluded to be small.

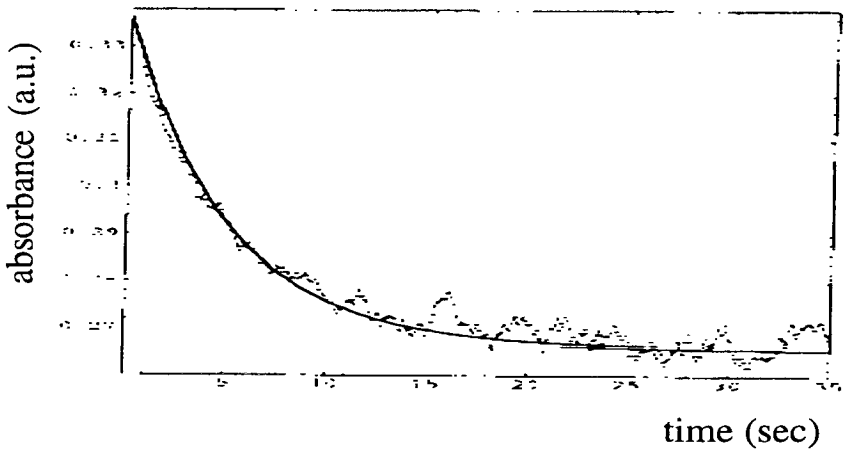

Figure 8.4 photo-bleaching dynamics upon illumination. The incident intensity is $I_0 = 0.5 \cdot W/cm^2$. The exponential fit is also shown (solid line).

The transmission experiment gives a value of $\Phi = 0.003 \cdot cm^2/mJ$, which implies much slower (an order of magnitude) decay rate for the photo-initiators than the typical polymerization rate.

Holography setup used in the experiments is shown in figure 8.5. Two coherent, expanded (collimated diameter 5 mm), extraordinarily polarized writing beams (at 325 nm) are incident to the polymer film. The intensity ratio of the two writing beams is

chosen to 25:1, which guarantees low intensity modulation. Also when the weak beam is blocked the average intensity changes very little.

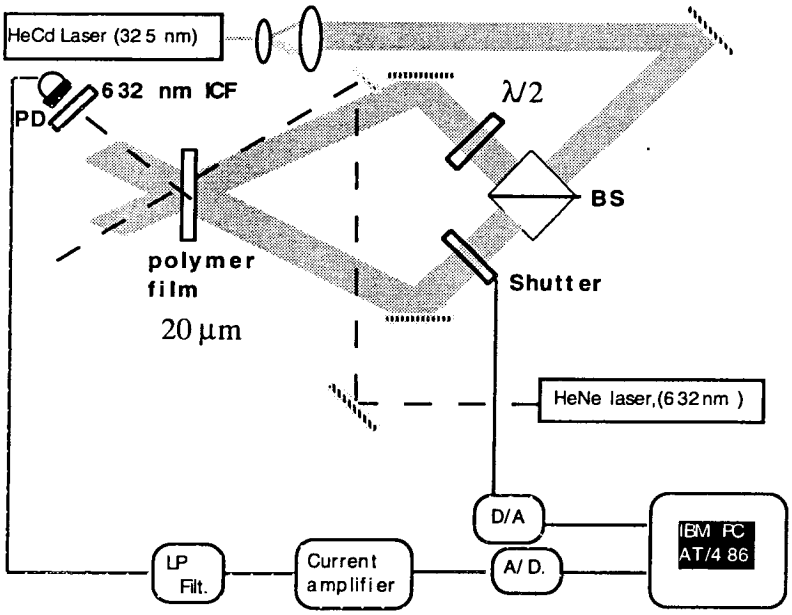

Figure 8.5 setup for the holography experiments

The angle between the two writing beams is 40 degrees, which implies a grating period of 0.32 microns. A computer controlled shutter (shutter 1) is placed on the optical path of the weaker writing beam. The grating is monitored by a phase matched beam at 632 nm, which does not initiate any photo-polymerization. The diffracted red beam is measured with a photo-diode and the dynamics is recorded with IBM PC AT/486.

In a typical experiment at first both writing beams are turned on. After a period of no polymerization, a sharp threshold is observed due to oxygen scavenging. This suggests as discussed in section 7.3 that $k_c >> k_p$. The fast increase in diffraction

efficiency is observed right after the threshold, signifying the dynamics of r_1. When a sufficient amount of diffraction efficiency is acquired, the weak beam is turned off (the writing time has to be much shorter than the polymerization dynamics). After the second weak beam is turned off spatial modulation of the radical concentration r_1 decreases very quickly. As a result the diffraction efficiency peaks shortly after the second beam is turned off. Then a slow decay of the diffraction efficiency, due to the out-of-phase component $m_1 r_0$, figure 8.2, is observed.

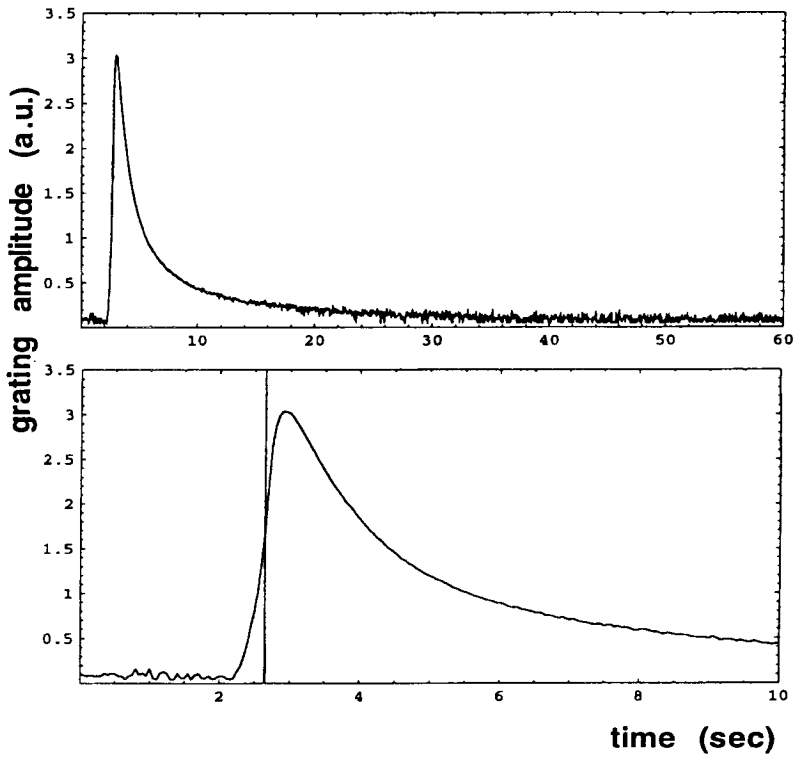

Figure 8.6 grating dynamics observed in a typical experiment, after the induction period due to oxygen, the grating begins to build up quickly. The second writing beam is turned off at *t=2.6 sec*. The grating continues to grow for a short time, peaks and goes through a

long decay. The fact that grating decays to zero implies that the monomer diffusion is not dominant at these intensities, $I_0 = 2.5 \cdot mW / cm^2$.

As shown in figure 8.7, the decay of the grating does not follow a simple exponential function. The increasing viscosity of the material as the polymerization proceeds results in the slowing down of the polymerization rate, or the reaction constants, $k_p / \sqrt{2k_t}$ decreases as the polymerization progresses.

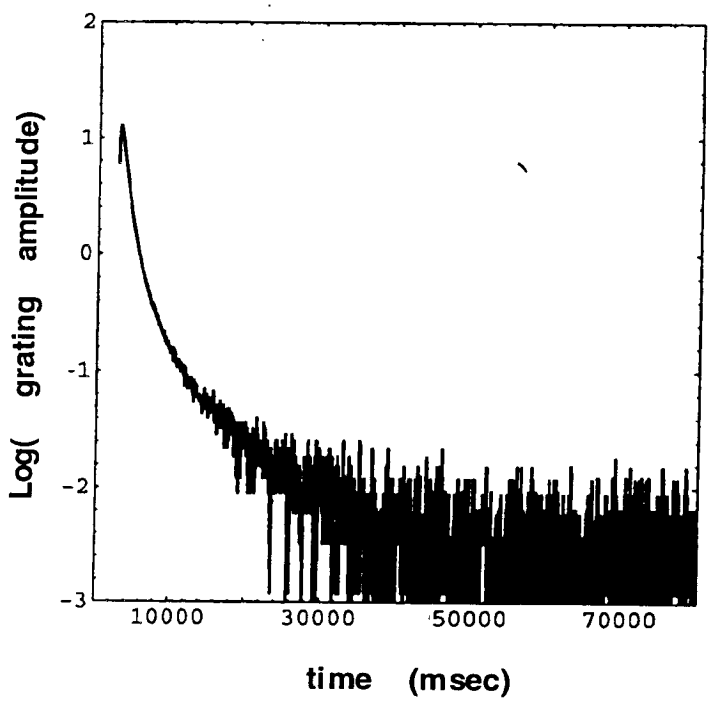

Figure 8.7 Log-linear plot of diffraction efficiency dynamics. Expected linear behavior is not present, dynamics only up to 50 seconds can be seen, $I_0 = 2.5 \cdot mW / cm^2$.

Since the diffraction efficiency is erased completely in figure 8.7, we conclude that the diffusion of monomers is not observable in this regime. We calculate the initial $k_p/\sqrt{2k_t}$ ratio from the initial slope of the decay curve (or $1/\tau_2$) in figure 8.7 to be $160\cdot\sqrt{L/(M\,\mathrm{sec})}$. The time it takes from turning off the second writing beam to the peaking of the diffraction efficiency is equal to τ_3 as defined in equation 8.6. From these two measurements we calculate the initial values of k_p, k_t to be $3\cdot10^4$, 10^6 *L(M sec),* respectively. Notice that the radical dynamics in figure 8.6 and 8.7 take place in the order of a second, while the polymerization dynamics takes place in tens of seconds and the initiator decay takes place in hundreds of second. We can say few things about the oxygen kinetic parameters. As mentioned before because of the sharp thresholding $k_c >> k_p$ must be true [7]. From the time at which the polymerization starts τ_c we can calculate the initial molar concentration in the monomer solution to be o(0) = 5 10^{-5} *M/L.*

In order to measure the monomer diffusion constant we lower the average intensity and in the regime where the erasure of the grating is due to the monomer diffusion we expect some grating amplitude to survive (fixed grating) at long time, figure 8.3 decay scenario b. For this purpose we studied the dynamics for intensities in the range 1 to 10^{-2} mW/cm^2. We find that within this range the monomer diffusion is not observed, for the investigated monomer. However from our observations we can set an upper limit for the monomer diffusion, $D_m << 10^{-2}\cdot cm^2/\sec$.

With dynamics recorded at different intensities we look for scaling with $\sqrt{I_0}$. Figure 8.8 shows the dynamics at seven different intensities, (roughly spaced evenly in the intensity range mentioned above). Clearly for the most part of the dynamics scaling works extremely well. This is a strong proof of the bimolecular termination reaction which is expected to take place in these chemicals. It also proves that the kinetic constants are only functions of the local monomer concentration (conversion efficiency). In figure 8.8a the dynamics is shown from the time the second writing beam is turned off. The time it takes for the diffraction efficiency to peak signifies the radical dynamics and as shown in the first figure, the scaling works for the radical dynamics as well. Note that in these figures, the quantity of interest is the slope of the logarithmic decay curves. Parameters that effect the final result as multiplicative constants (such as film thickness, proportionality constant between index change and the polymer molar concentration) are expected to result in vertical shifts of the curves. In figure 8.8 such shifts are accounted by aligning the long time dynamics of the dynamic curves.

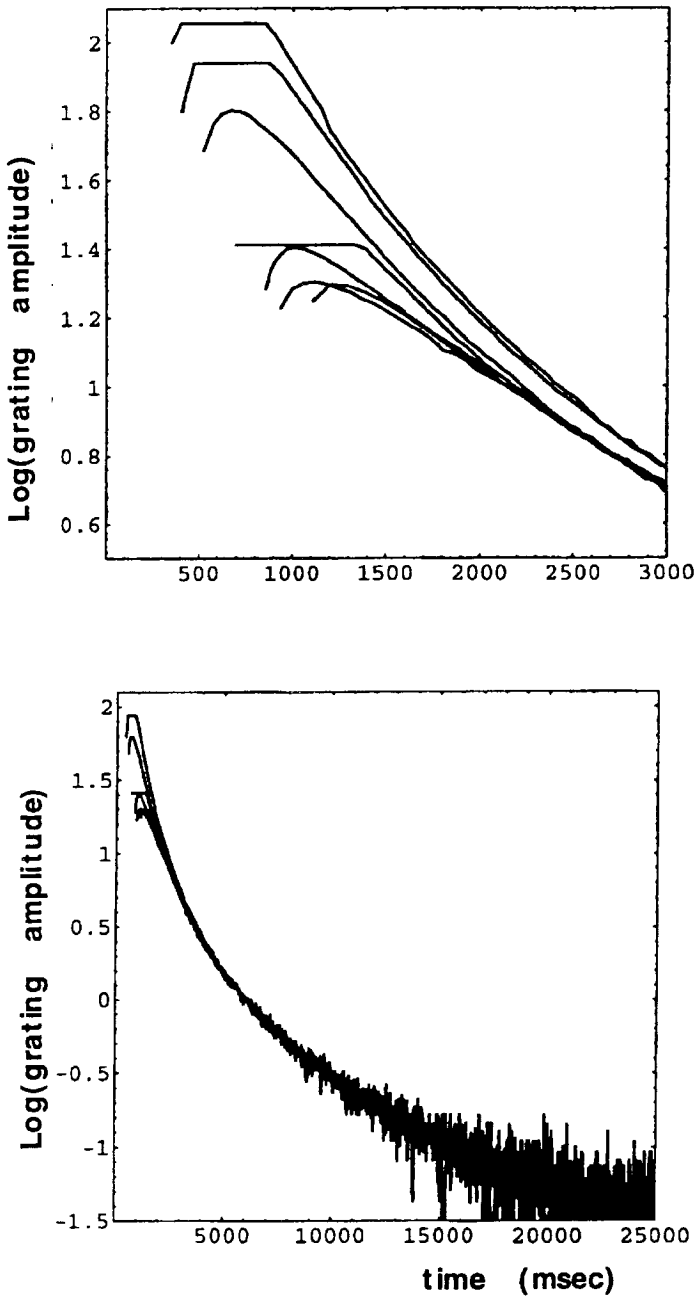

Figure 8.8 scaled dynamics exhibited by the grating amplitudes for various average intensities. Only the dynamics during the erasure with single writing beam is shown.

Oxygen seems to play a role during the very initial phases of the polymerization. Figure 8.9 shows the grating amplitude (scaled) dynamics for various intensities. The slope of the grating amplitude curve is $k_p r_1 m_0$. The radical dynamics is expected to be very quick (τ_1 section 8.3) and achieves a quasi-steady-state value which is expected to be scaleable with $\sqrt{I_0}$. The quasi-steady-state value for r_1 manifests itself as the final linear slopes in figure 8.9. However, at lower intensities possibly due to stronger oxygen effects it takes longer time for radicals to achieve their quasi-steady-state value.

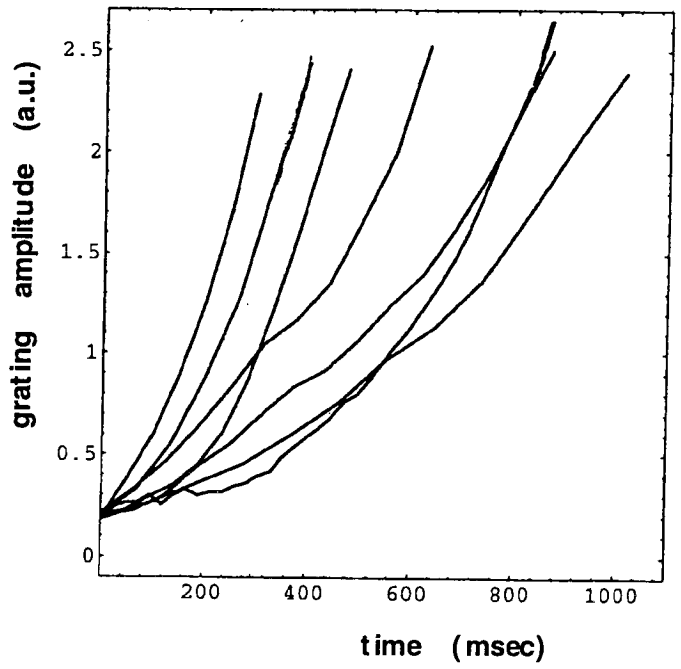

Figure 8.9, grating amplitude dynamics during the writing phase. The time is scaled by square root of the average intensity. For lower intensities it takes longer time to achieve the same grating amplitude.

Lastly an attempt to model the viscosity effects on the kinetic constants will be described. This attempt is initiated by the observation that the decay dynamics in figure 8.8,9 actually follow a simple power law. Figure 8.10 shows the log-log plot of the scaled dynamic curves for two extreme average intensities. Slope of the linear behavior is one, thus the monomer (or polymer) concentration can be expressed as:

$$m_1(t) = \frac{m_{10}}{t\sqrt{s(0)\Phi I_0}}. \qquad 8.10$$

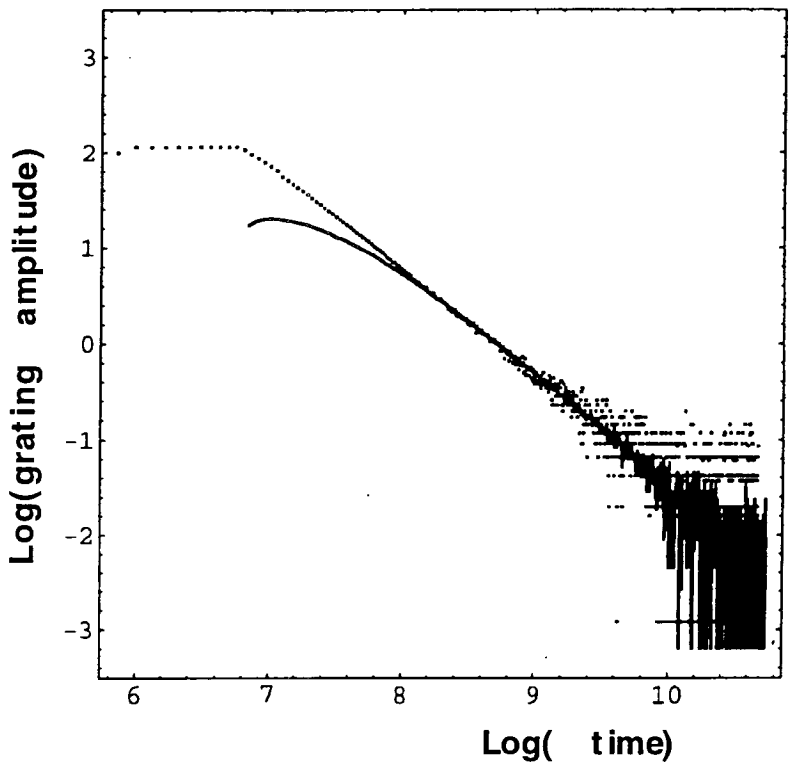

Figure 8.10 Log-log plot of grating decay dynamics (scaled), for two extreme intensities. The power low behavior is clear.

If one defines $f(m) = k_p / \sqrt{2k_t}$, (assuming that kinetic constants only depend on the degree of polymerization), then during the slow decay of the written grating, the kinetic equations for the monomer concentrations take the following form:

$$\frac{dm_0}{dt} = -f(m_0)m_0\sqrt{I_0 s_0(0)\Phi}$$
$$\frac{dm_1}{dt} = -m_1\left(f(m_0) + \frac{df}{dm_0}m_0\right)\sqrt{I_0 s_0(0)\Phi}. \qquad 8.11$$

It can be shown that a linear functionality of f with monomer concentration explains the functional dependence of equation 8.10.

$$f(m) = f(m(0))\frac{m}{m(0)}. \qquad 8.12$$

It may be that the linear dependence of $f(m)$ is only true for the particular monomer that was used. It remains to be seen if this is a general characteristic of gel effect (increased viscosity).

8.5 A simple way to look for monomer diffusion

In the last section, monomer diffusion is sought after by decreasing the average intensity gradually. However, this technique can require long recordings of grating decay

dynamics. In this section a simpler scheme for looking for monomer diffusion will be described, using the technique monomer diffusion in two other multifunctional monomers is sought after.

The technique again involves writing of a weak grating, (for a short time, much shorter than the polymerization dynamics). Then both of the writing beams are turned off. In the dark, the spatially varying monomer concentration, m_1, is expected to decay due to monomer diffusion. After waiting for some time in the dark, only one of the writing beams is turned on. If m_1 decays completely due to monomer diffusion during the dark-period then there is no grating component out-of-phase with the intensity, I_1 and no decay of the grating is expected. If on the other hand there is no diffusion of monomers than, m_1 does not decay and the grating is completely erased, signifying the expected uniform polymer concentration, in the absence of monomer diffusion.

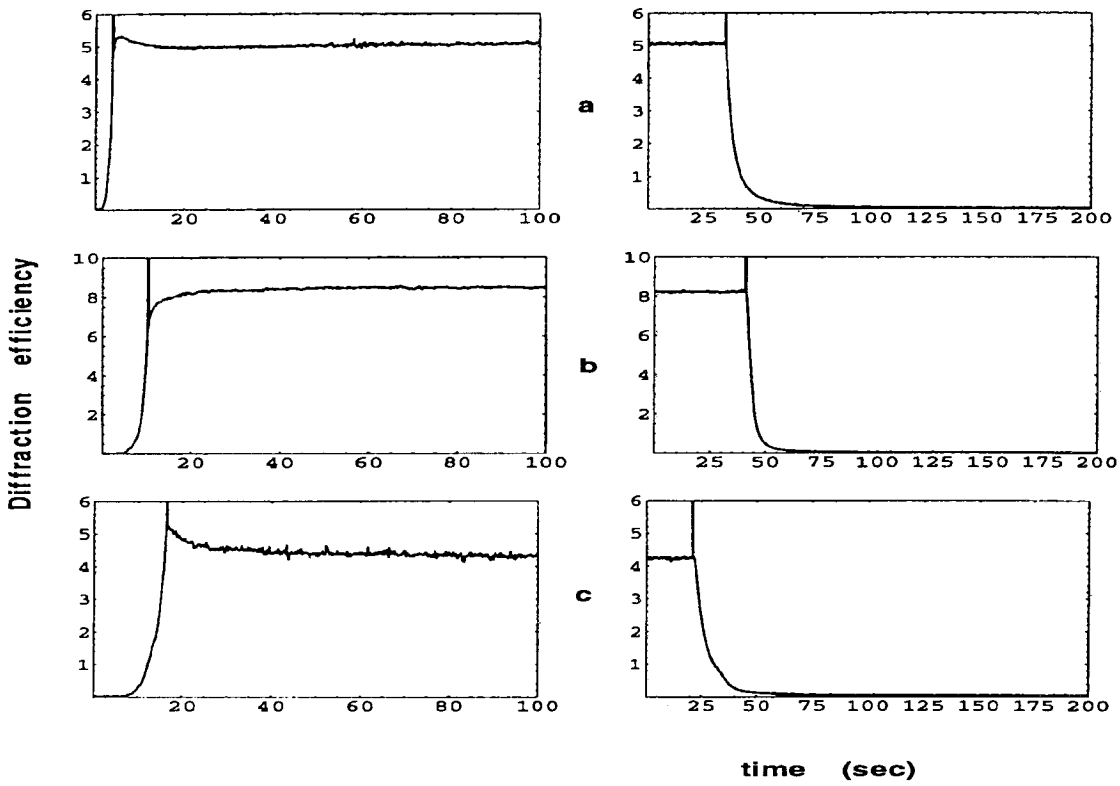

Figure 8.11 monomer diffusion is sought after in three different multifunctional acrylates, a)TMTA, b) Butyle ethylene c)HDODA with 0.1 wt % initiator concentration (Irgacure 369).

The technique is carried out in two other difunctional acrylate monomers, HDODA (UCB Radcure) and ethylene diacrylate with 0.1 wt % Irgacure 369. The dark time in each experiment was 30 minutes. For each of the multifunctional monomer the grating very quickly decays to zero when the erasure beam is turned on signifying the fact that the monomer diffusion is small. Considering the amount of time waiting in the dark, one can calculate an upper limit for diffusion constants in these materials, $D_m << 10^{-2}\, cm^2 / \sec$. This is a surprising result considering typical monomer diffusion constants are on the

order of $10^{-7} - 10^{-9} cm^2$ / sec [6]. This may be due to the multifunctional nature of the monomers that were used. Multi-functionality of the monomer results in strong crosslinking in the forming polymer network early on in the polymerization dynamics and is expected to result in considerable decrease in diffusion constants. Also since each molecule has in principle two-three functional groups, once one of the monomers (functional group) reacts with a propagating radical, the remaining unreacted monomers on the molecule become part of a large molecule, (although they have not yet reacted). From this argument by the time 10% conversion is completed, 30-40% of the remaining monomers may already be part of a larger molecule and not be able to diffuse. Our attempts to write gratings in butyl acrylate, a monofunctional acrylate with the same optical set up failed, although the polymerization is observed (hardening of the material). It is interesting to note that such a result with in the context of our model is only possible if a strong radical diffusion is assumed.

8.6 Is monomer diffusion essential for hologram fixing?

In the previous section, detailed experiments with three different multifunctional monomers are described. We conclude that very little monomer diffusion exists in these materials.

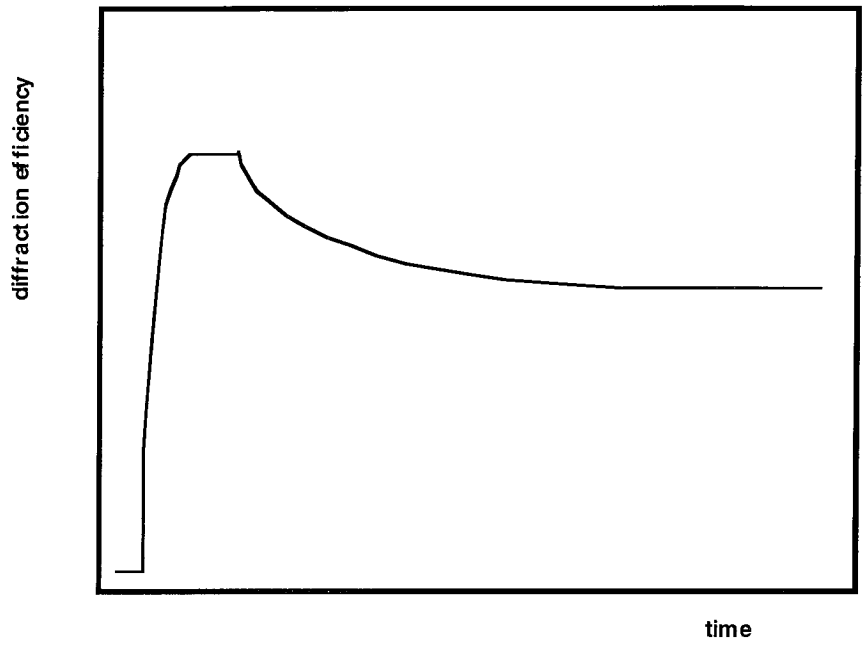

Figure 8.12, typical grating dynamic upon long writing, at long time a stable, fixed grating is attained.

When a grating is written in any of these chemicals for a long time, one typically sees the dynamics as shown in figure 8.12. In the beginning of the dynamics the expected in-phase grating develops very quickly followed by the gradual decay expected in the absence of monomer diffusion. However, unlike the expectations, the grating at long times do not decay to zero, instead a fixed, stable grating is obtained. This observation is contrary to the generally accepted view that the monomer diffusion is essential for fixing holograms [9]. One possible explanation is the incomplete polymerization that may come about due to strong crosslinking. For example this may happen also if the initiator concention completely decays before the 100% conversion is achieved. In this case, in

the frame work of the above model, ignoring all the diffusion effects, the problem can be solved exactly for the polymer concentration (at long times):

$$p = \frac{m(0)}{\langle x \rangle}[1 - \exp(-2\frac{(k_p r(0))}{\Phi I})] \qquad 8.13$$

where $r(0) = \sqrt{s(0)\Phi I/(2k_t)}$ is the radical concentration early on in the polymerization dynamics where the initiators are undepleted. As can be seen from equation 8.13 because of the square root of intensity dependence of the polymerization rate ($k_p r(0)$) the exponent is proportional to inverse square root of the intensity. The intensity dependence of the final polymer concentration signifies a fixed grating, that is out-of-phase with the intensity pattern. But since the dynamics shown in figure 8.12 does not show a change in the phase of the grating, the depletion of the photo-initiators is more likely to be not the cause of the fixed grating.

Lastly we would like to note that in the presence of monomer diffusion expected long time dynamics is exactly the same as what is shown in figure 8.12. What we have shown here is that such aggregate dynamics can also come about in the absence of monomer diffusion and one needs to be careful in identifying the hologram fixing mechanism which is probably essential from the point of view of stability and the life times of the fixed holograms.

8.7 Summary

Photopolymerization dynamics within the frame work of a standard polymerization model is studied. An experimental technique in which the dynamics of the initiators. monomers, and radicals are isolated and kinetic parameters are measured, is described. The technique is demonstrated with a multifunctional monomer, TMPTA. A simple way to determine the strength of monomer diffusion is described. The technique determines the presence of the monomer diffusion only with qualitative observations. Lastly we argue that observation of a fixed grating does not necessarily imply the existence of monomer diffusion. We demonstrate that in the chemicals in which no monomer diffusion was observed, fixed, stable gratings can be obtained.

References for Chapter Eight

[1] C. Decker, K. Moussa, Maromolecules 22, 4455 (1989).

[2] G. R. Tryson, A. R. Shultz, J. Polym. Sci., 17, 2059 (1979).

[3] C Decker, K Moussa, Makroml. Chem. 192, 507 (1991)

[4] C Decker, K Moussa, in Radiation Curing of Polymeric Materials, C E Hoyle and J F Kinstle, eds, (Amer Chem Soc Washinton 1990).

[5] C Decker, K Moussa, Markromol. Chem. Rapid Commun 11, 159 (1990).

[6] Vadim V. Krongauz, section 2.5 in Processes in Photoreactive Polymers, edited by V. V. Krongauz, A. D. Trifunac (Capman and Hall, 1995).

[7] Odion, Georg G., in Principles of Polymerization (Wiley-Interscience Publications, (1981)

[8] C Decker, section 1.2 in Processes in Photoreactive Polymers, edited by V. V. Krongauz, A. D. Trifunac (Capman and Hall, 1995).

[9] R. A. Lessard, R. Changkakoti, G. Manivannan, section 3.1 in Processes in Photoreactive Polymers, edited by V. V. Krongauz, A. D. Trifunac (Capman and Hall, 1995).